Title	Magnetically levitated linear slider with non-co ntact power supply
Author(s)	WATHTHEGE BUDDHIKA IMANTHA, Annasiwaththa Annasi
Citation	, .
Date of issue	2016-09
URL	http://hdl.handle.net/10173/1416
Rights	
Text version	ETD

Magnetically levitated linear slider with non-contact power supply.

A dissertation submitted to
Kochi University of Technology
in partial fulfillment of the requirements for the
degree of Doctor of Philosophy

by

A.W.B.I. Annasiwaththa

Graduate School of Engineering
Kochi University of Technology
Japan

Sep. 2016

Abstract

Magnetically levitated material handling systems offer many advantages to clean room manufacturing processes due to the absence of contact surfaces with relative motion. Therefore, a magnetically levitated linear slider (MagLevLS) with a non-contact power transfer method was investigated and presented. The proposed MagLevLS platform uses four hybrid electromagnets (HEMs) as actuators for levitation and an open-end generator for non-contact power transfer. The levitation platform was fabricated by installing four HEMs at four corners of a rigid rectangular steel plate. Ability to levitate and achieve zero power control of the suggested four points suspended platform under cogging torque and forces introduced by the non-contact power transfer method was investigated. The HEM was analyzed using FEM and results was used to obtain the relationship between the attractive force, the air gap, and the coil current. Furthermore, a prototype HEM was tested to validate FEM analysis data and results presented. The mathematical model of the HEM describing the attractive force in terms of coil current and air gap was obtained by surface fitting FEM data and experimental data. An open-end generator was designed to meet electrical power, force, torque and air gap requirements of the levitated platform and analyzed using FEM. ABS were purposed as the stator core construction material of the open-end generator to achieve required performance of the open-end generator for MagLevLS system. The open-end generator with ABS stator core can achieve near zero forces between the rotor and the stator under eccentricities according to the presented FEM analysis results. Furthermore, the torque of the open-end generator with ABS stator core shows almost constant torque behavior under constant electrical load. Subsequent experiments using a prototype open-end generator confirmed the FEM analysis results, and the obtained results are presented. A mathematical model to describe three degrees of freedom motion of the levitated platform was developed and a zero power levitation controller was designed and presented. Stable levitation was

achieved using three PD controllers to control three modes of operation of the platform specified as the vertical air gap, roll, and pitch. Zero power control loop was implemented using three integral controllers attached to each mode of the operation of the levitated platform. A nonlinear system dynamics was simulated, the levitation controller was tuned, and performance was observed using the designed nonlinear system simulator. A prototype levitation platform with the non-contact power supply was fabricated, and a 0.25 W steady state power consumption per each HEM was achieved using designed zero power controller. Experimental and simulation observations of the levitated platform under different step inputs were presented. According to the results, MagLevLS can achieve stable lavation under cogging forces and generate sufficient power for continuous operation.

Acknowledgments

Contents

List of Figures

List of Tables

Chapter 1

Introduction

1.1 Background

Modern advances in technology increasingly demand miniaturized products and high-density products packaging. Furthermore, demand for higher quality and low rejection ratios are increasing in the competitive market. During last decade, there is increased research interest leading to micro and nanotechnologies. The use of mobile devices are rapidly increased and mass manufacturing of these devices create a market for better manufacturing technologies. Some of the rapidly increasing markets include microprocessors and display panel manufacturing. According to MarketsandMarkets[1] market research, display market will reach $155 billion by the year 2020. In order to manufacture high pixel density displays, clean rooms are required with increasingly tougher clean environments. As of Q1, 2016 commercial semiconductor manufacturing in 14nm node and 10nm node under development. These advances require improved clean room manufacturing technologies. The magnetically levitated machines offer major improvements to clean room manufacturing technologies. Figure 1.1 shows an example clean room operation.

Regular material handling machines such as conveyors and motors have a mover and a stator. The mover and the stator have mechanical connections between each other. These mechanical connections include common mechanical machine elements such as bearings, guides ways, rollers, and gears depending on the nature of the machine. Such machine elements provide support for forces experienced by machines. Furthermore, they provide limits and guidance to moving parts of

---

[1]`http://www.marketsandmarkets.com/PressReleases/display.asp` 2016 Sep. 05

Figure 1.1: Hard disk assembly in a Segate clean room.[2]

the machine. In order to avoid the mechanical connection between the mover and the stator, magnetic levitation can be used. However, magnetic levitation should be able to guide and support moving parts of the machine. Mechanical machine elements connecting stators and movers have contact surfaces with relative velocity between each other. Such movements are subjected to friction and therefore lubrication is essential when the mechanical machine elements are involved. When these machines are operated, friction between moving parts will break small particles from contact surfaces. The small particles broken from machines leads to wear of machine elements. Furthermore, lubrication chemicals and small particles broken from contact surfaces are released into the operating environment of the machine. If the machines are operated in a clean room environment, these released particles could contaminate clean operating environment. Furthermore, mechanical machine elements could subjected to vibrations due to unbalanced mass rotations and non-smooth sliding surfaces. Any power transfer between a mover and a stator achieved by utilizing commutators could introduce electrical noise. Furthermore, these commutators are subjected to friction leading to particle release.

---

[2]Image from `https://commons.wikimedia.org/wiki/File:Seagate's_clean_room.jpg` 2016 Sep. 05

The machines which utilize magnetic levitation to separate the mover and the stator offers many advantages over regular machines which utilize mechanical machine elements. When the mover and the stator of a machine is separated by a non-contact mechanism like magnetic levitation, the friction between the mover and the stator is zero.Therefore, lubrication is not necessary and particles will not be released to the operating environment during operation. The magnetically levitated machine will not be subjected to wear. Mechanical vibrations occurred from mechanical machine elements will be reduced. Even though a mover can be separated from a stator using magnetic levitation, it is necessary to supply power to the levitated mover to achieve continuous operation. If the continuous operation of the levitated machine is not required, batteries could be used to supply power to the mover. If batteries are used, the amount of time that the levitated machine can be operated continuously depend on the amount of energy stored in the batteries. Use of large batteries to increase continuous operation duration will also increase levitated weight and the physical size of the machine. By reducing the amount of power consumed by the levitated machine, the duration of continuous operation can be increased. Therefore, is important to study methods to reduce power consumption of the levitated mover. Therefore Zero power control mechanisms play important role in magnetically levitated machines.

If the continuous operation of a magnetically levitated machine is preferred, it is necessary to supply power to the levitated mover of the machine using a non-contact power transfer method, because batteries could not supply energy to continuous operation. Therefore, it is important to study magnetic levitation with non-contact power transfer methods.

1.2 Previous research about similar MagLev material transport systems

The previous research by M. Morishita [1, 2]. suggests a use of linear quadratic regulator with integral action (LQI control scheme) to achieve zero power control of a magnetically levitated linear slider (MagLevLS) platform. The platform suggested by M. Morishita utilize four hybrid electromagnets (HEMs) as actuators and a platform consisting of two rigid plates with a pivot joint to achieve zero power control. The pivot joint is essential to introduce an extra degree of freedom to the levitated platform so that the zero power control can be realized with four hybrid

electromagnets [1, 2]. The controller was designed based on linearized mathematical model and HEMs were controlled using voltage controller mode. The controller was designed to control four modes of the operation of levitated platform. The four controlled modes include vertical levitation position, pitch, and two rolling motions. The second rolling freedom was introduced by the pivot joint between two levitated metal plates. The platform is powered by batteries, and continuous operation is not possible. Furthermore, information is not presented about power consumption of electronic controllers, linear motors, and sensors.

The previous research by K. J. Kim and C. H. Kim et al. [3, 4, 5] uses a secondary suspension mechanism to achieve zero power control and reduce vertical vibrations. The HEMs are installed on the secondary suspension system. The secondary suspension is acting as an extra degree of freedom to the levitated platform, so that the zero power control can be achieved. The lateral motion of the levitated platform was limited using guide rollers, and improved platform was presented with four guidance magnets to control the lateral motion. The spring constants for the secondary suspension system to reduce vertical vibrations due to guide rail surface defects was investigated and presented.

The previous research by Yuji Ishino et al. [6] uses solar cells and fluorescent lamps for non-contact power transfer. The levitated platform uses three hybrid electromagnets for levitation and three parallel guide rails for guidance. The presented system is capable of continuous levitation while consuming less than 250mW power. If the levitated platform require linear motor on the levitated platform for translation (i.e. horizontal transport of goods), the suggested system does not provide sufficient power.

The previous research about non-contact power transfer methods suggest the use of inductively and capacitively coupled systems. Furthermore, research was done on strongly coupled magnetic resonances and weakly coupled magnetostatic resonators. Different power transmitter and receiver arrangements are discussed, and low, medium and long range wireless power transmission using an inductive coupling and magnetic resonances are presented. [7, 8, 9, 10, 11, 12].

1.3   Motivation

Continuous operation of magnetically levitated linear slider platforms was not previously discussed and presented. The current levitated platforms use batteries or

wires to supply power. Even though very low power levitation was achieved for HEMs, power consumption by on-board electronics, sensors, and linear motors was not considered. However, the amount of power consumed by electronics, sensors, and the linear motor is much higher than that of zero power controlled HEMs. Therefore, it is essential to use non-contact power transfer method to achieve continuous levitated operation. The lateral alignment of the levitated platform was previously achieved using mechanical guide rollers and controlled by electromagnets [4, 5]. In such systems, the vertical position of the levitation is affected by lateral misalignment, and subsequent corrective action requires power. Therefore HEM can be improved to achieve better lateral and vertical force characteristics. Potential applications for the magnetically levitated linear slider platform with non-contact power transfer includes continuous material handling in clean room environments like semiconductor and LCD manufacturing. Furthermore, if sufficient amount of power can be transferred to a levitated platform, a machine-like a robot manipulator can be installed on the levitated platform when necessary.

1.4 Objectives of the research

It is expected to develop a prototype of a magnetically levitated linear slider platform with non-contact power transfer. It is expected to develop non-contact power transfer method so that the levitated platform can receive sufficient power to on-board controllers, sensors, linear motors and HEM actuators for continuous levitation and translation. The non-contact power transfer method will be customized to magnetically levitated linear slider platform. The HEMs used for levitation will be improved to achieve passive lateral alignment while reducing the effect on vertical levitation. It is expected to achieve near zero power levitation using a four point suspended single rigid platform.

Use of an open-end generator is suggested as non-contact power transfer method. The rotor eccentricities produce large attractive forces between the rotor and the stator of permanent magnet generators. Since passive lateral alignment is preferred in current research, the open-end generator should be designed to produce minimum attractive forces under rotor eccentricities. Furthermore, it is necessary to reduce torque fluctuation due to cogging to reduce vibrations introduced by cogging torque of the open-end generator.

Therefore major objectives of the research are,

- New system integration with non-contact power transfer method

- Design an open-end generator with minimum attractive forces between the rotor and the stator

- Design an open-end generator with minimum cogging torque

- Improve HEM to achieve passive lateral alignment while having minimum effect on vertical levitation

- Achieve near zero power operation with 3 DOF controller while having 4 HEMs and open-end generator is producing cogging forces and torques

Chapter 2

The prototype levitation system design

The proposed magnetically levitated linear slider system is shown in Fig. 2.1 and consists of three main assemblies,

1. Stationary support structure. (The stator)

2. Magnetically levitated, linear moving platform (The MagLevLS platform)

3. Long rotating permanent magnet array (The rotor)

2.1   Stationary support structure

Two guide rails used to guide magnetic flux paths of the HEMs are mounted on the stationary support structure as shown in Fig. 2.1. The supported linear moving distance of the prototype platform is 30cm. The support structure is made of A6061 Aluminum and SS400 steel. The rotor is mounted on the stationary support structure as shown and the rotor is driven by using an electric motor mounted on the stationary support structure. The motor and the rotor was coupled using a belt drive as shown in the prototype system. It is expected to use magnetic bearings and direct coupling between rotor and motor to avoid mechanical contacts between moving and stationary components. The stator of the linear motor is mounted on the stationary structure. However, it is removed from the Fig. 2.1 to highlight other elements of the design clearly.
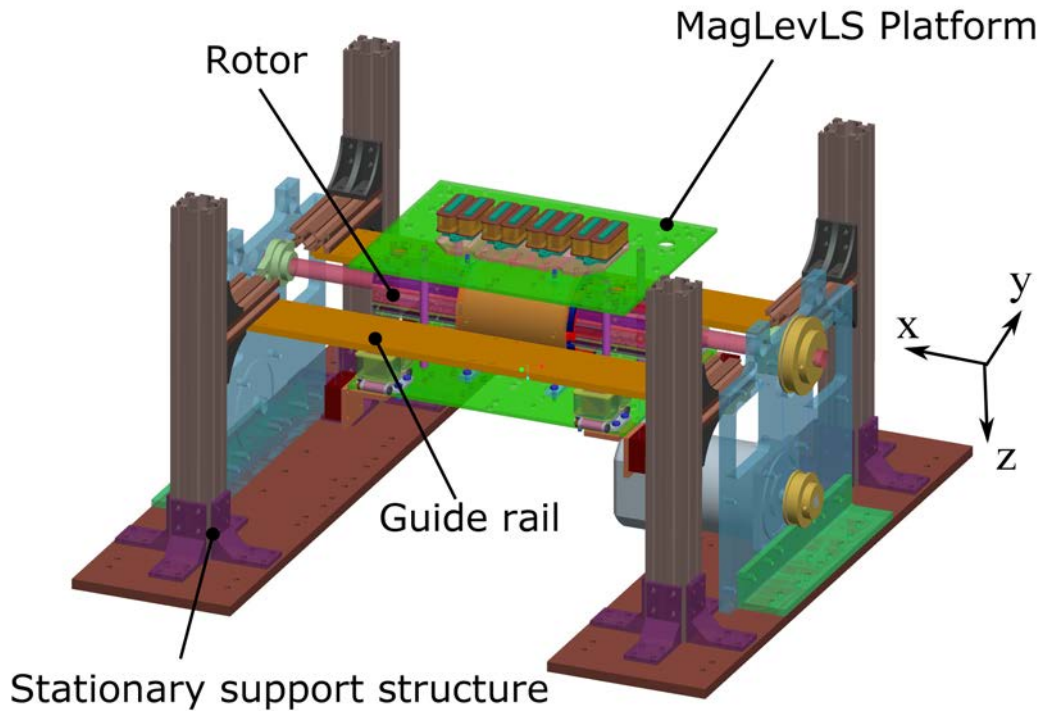
Figure 2.1: Magnetically levitated linear slider system. (The permanent magnet stator of the linear motor is not shown in this figure.

2.2 Magnetically levitated, linear moving platform

Figure 2.2 shows the basic design of the magnetically levitated, linear moving platform. The levitated platform contains four major elements of the system, which includes HEMs, air gap sensors, the stator of the open-end generator and the linear motor. The HEMs, the open-end generator, and the linear motor are custom designed to the MagLevLS platform.

The top plate of the levitated platform is made of A6061 Aluminum, and the bottom plate of the platform is made of SUS304 stainless steel. Stainless steel was used to increase the strength of the platform and Aluminum is used to reduce overall levitated weight. The top and the bottom plates are connected using rods as shown. The mover of the linear motor is mounted on the top plate.

The four HEMs used as actuators for the levitation are mounted at four corners of the platform as shown in fig. 2.2. A laser distance sensor is mounted close to each HEM to measure the air gap between HEM and the guide rail. The stator of

8
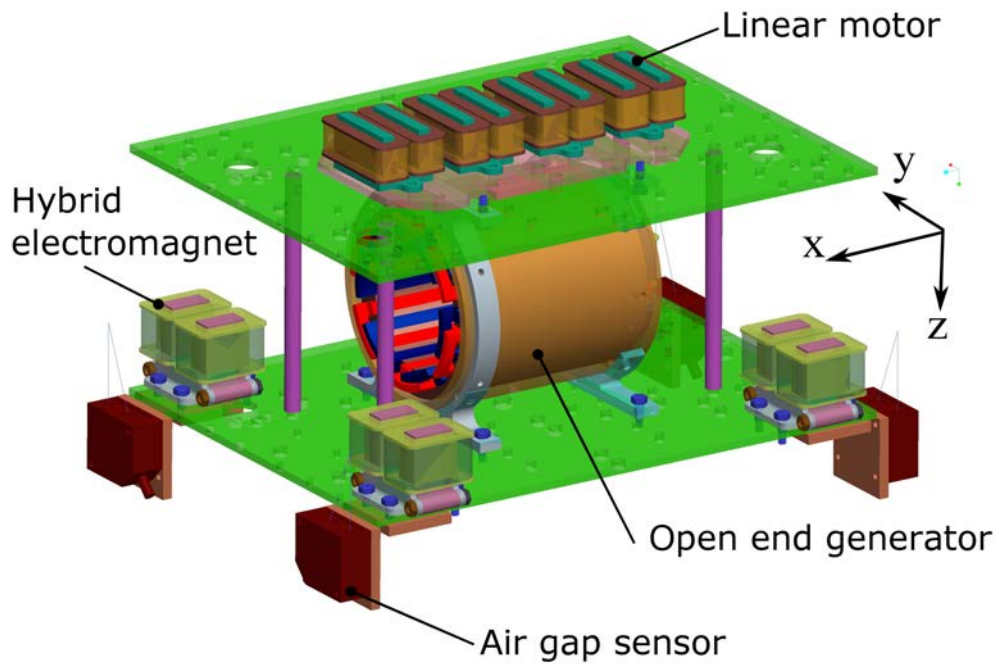
Figure 2.2: Magnetically levitated linear moving platform.

the open-end generator was mounted between the top and the bottom plates.

2.3 Long rotating permanent magnet array (The rotor)

The long rotating permanent magnet array is shown in the Fig. 2.3 The rotor as six magnetic pole pairs mounted on the surface of the rotor as shown. The base material of the rotor is SS400 soft magnetic steel. The rotor was rotated using an AC electric motor. The permanent magnets used for the rotor are the N35 type and has dimensions of 3mm×10mm×60mm. These permanent magnets are magnetized in 3mm direction. The red color and the blue color faces shown in Fig. 2.3 represents the north and the south pole of the permanent magnets. The design of the rotor was influenced by the availability of suitable permanent magnets for the design.
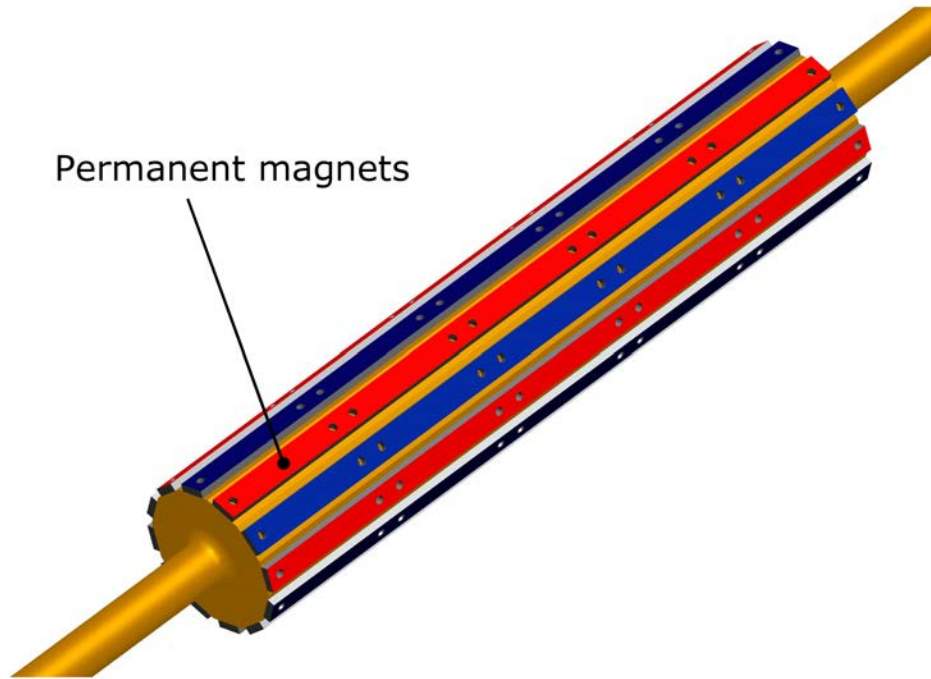
Figure 2.3: The permanent magnet rotor.

2.4 Hybrid Electromagnet and guide rail

Hybrid electromagnet design consists of a 25mm×21mm×12mm N50 permanent magnet and a laminated soft magnetic steel core. The soft magnetic steel used is grain oriented silicon steel type 23ZH100 manufactured by Nippon Steel & Sumitomo Metal Corporation. Each lamination has a thickness of 0.23mm, and the lamination factor is 0.94. Each hybrid electromagnet has two coils connected in series, and each coil has 360 turns wound using ϕ0.6mm copper wire. The hybrid electromagnet has a pole face area of 21mm×10mm. Figure 2.4 shows the basic design of the Hybrid electromagnet. The arrows in the Fig. 2.4 represents the magnetic flux path. The core of the hybrid electromagnet consists of 2 parts aligned with the north and the south pole of the permanent magnet as shown in Fig. 2.4. A major part of the magnetic flux generated by the electromagnets is directed through the permanent magnet due to this arrangement.

The guide rails were manufactured using SS400 soft magnetic steel. The guide rails were galvanized to overcome corrosion.
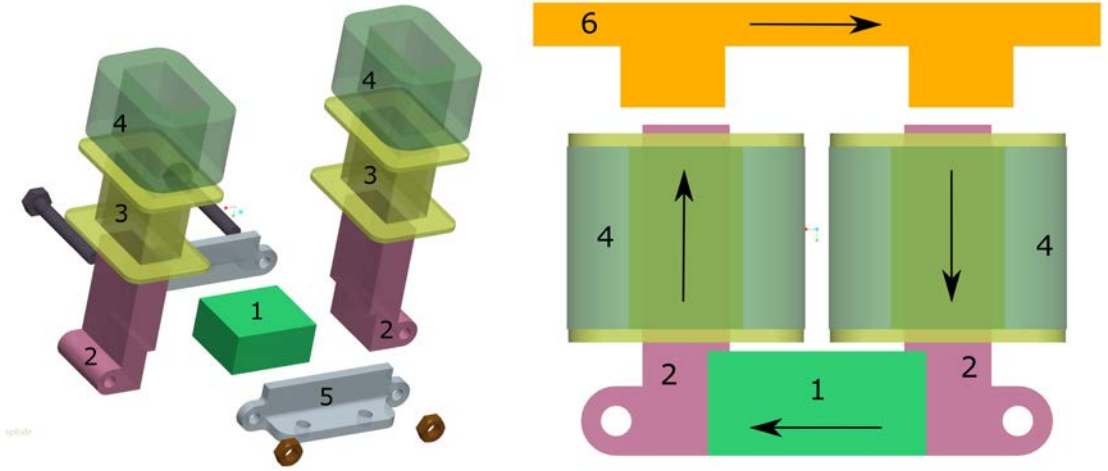
Figure 2.4: Hybrid electromagnet design. (1. N50 permanent magnet, 2. 23ZH100 soft magnetic steel core, 3. Plastic bobbin, 4. Copper coil, 5. Mounting plate, 6. Guide rail.)

2.5 Open-end generator

An open-end generator was used to achieve non-contact power transfer to the levitated platform. The non-contact power transfer system includes the stator core of the open-end generator mounted on the levitated platform as shown in Fig. 2.2. A permanent magnet rotor mounted on the stationary structure of the MagLevLS system as shown in Fig. 2.1 was used to generate electrical power in the coils of the open-end generator. The length in the x-direction of the generator core is 100mm. The open-end generator winding consists of 2 phases arranged in 180-degree phase angle. Each phase has 120 turns wound using ϕ0.5mm copper wire. The core of the open-end generator was manufactured using ABS for the final prototype. Figure. 2.5 shows a basic 3D design of the open-end generator and stator mountings.

For a three phase modular permanent magnet machine, feasible slot and pole combinations are described by Eq. 2.1 and Eq. 2.2. Furthermore, it is possible to obtain feasible slot and pole combinations by multiplying feasible N_s and p combinations by a positive integer. Table 2.1 shows feasible slot and pole counts for up to p=10 [13]. The geometry and the permanent magnet used for the prototype open-end generator do not allow the use of a feasible slot and pole combination. Therefore the efficiency of the prototype is less compared to a regular generator.
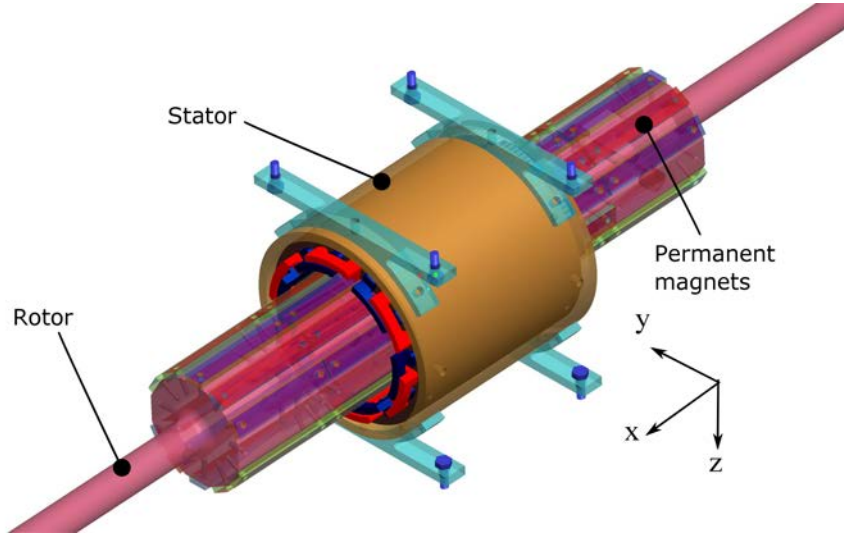
Figure 2.5: Open-end generator

However, higher efficiency is possible by using custom made permanent magnets.

$$N_s = 2p \pm 1 \tag{2.1}$$
$$N_s = 2p \pm 2 \tag{2.2}$$

where,

N_s = Slot count when $N_s/3$ = a positive integer

p = Number of pole pairs

2.6   Linear motor

A switched reluctance linear motor is used move the levitated platform in the x-direction. The linear motor design consists of 4 individually controlled electromagnets as the mover and an array of permanent magnets as a stator. The mover is mounted on top of the levitated platform as shown in Fig. 2.2. Each electromagnet consists of two coils connected in series. Figure 2.6 shows the design of the linear motor. The stator consists of permanent magnets, and SS400 strips mounted as shown in Fig. 2.6. The red and the blue colors represent the north and the south poles of permanent magnets. The permanent magnets used were type N35, has dimensions 3mm×10mm×60mm and magnetized in 3mm direction.

Table 2.1: Feasible slot and pole combinations for a three phase modular PM machine

Number of pole pairs p	Number of slots N_s
1	3
2	3,6
3	9
4	6,9,12
5	9,12,15
6	9,18
7	15,21
8	12,15,18,24
9	27
10	18,21,24,30
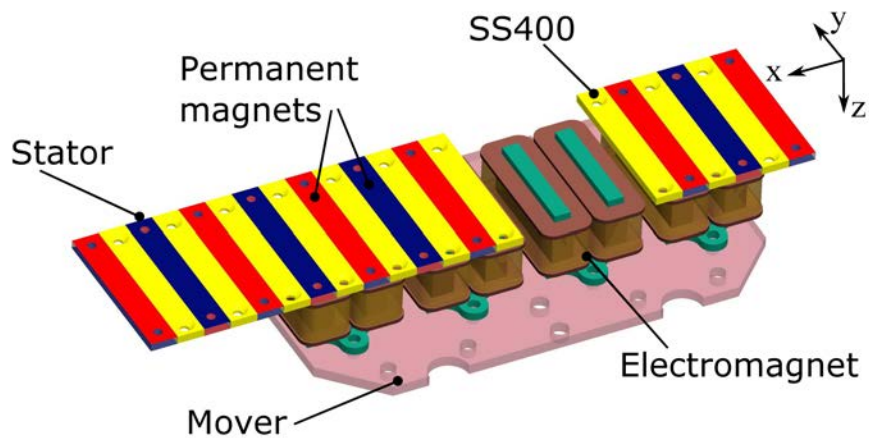
Figure 2.6: Linear motor

Chapter 3

Modeling and FEM analysis of hybrid electromagnet and Linear motor

The actuator used for the levitation was a hybrid electromagnet. The levitation system uses four identical HEMs and a HEM were modeled using 3D CAD software for FEM analysis. The system was propelled in x-direction using a switched reluctance linear motor. The FEM analysis was performed on 3D models, and the results were presented. The FEM analysis was performed using J-Mag designer software.

3.1 Attractive forces of Hybrid electromagnet

The hybrid electromagnet was analyzed using FEM to identify mathematical function describing force, current and air gap relationship. Table 3.1 shows the major parameters of the analyzed HEM. The bobbin thickness was selected by measuring a prototype HEM because the forces generated by HEM was affected by material between the soft magnetic steel core and copper winding.

The black dots shown in fig. 3.1 represents the data obtained by FEM analysis. According to the results, the attractive force between analyzed HEM and guide rail is approximately 36N at 2mm air gap and zero coil current. Therefore, designed HEM can levitate platform having an approximate weight of 15kg at an air gap of 2mm while having 0A coil current.

The attractive force between an electromagnet and a soft magnetic steel target

Table 3.1: Major parameters of the hybrid electromagnet and FEM analysis

Parameter	Value
Magnet pole area	10mm×21mm
Permanent magnet (PM)	12mm×21mm×25mm N50
PM magnetization direction	25mm
Number of coil windings	2, series-connected
Number of turns per coil	360 turns
Total coil resistance	4.3Ω
Bobbin thickness	1.6mm
Lamination factor	0.94
Analyzed air gap range	1mm to 6mm, 0.1mm increments
Analyzed current range	±3A, 0.2A and 0.1A increments
Guide rail material	SS400
HEM core material	23ZH100 (Nippon Steel and Sumitomo Metal Corporation)
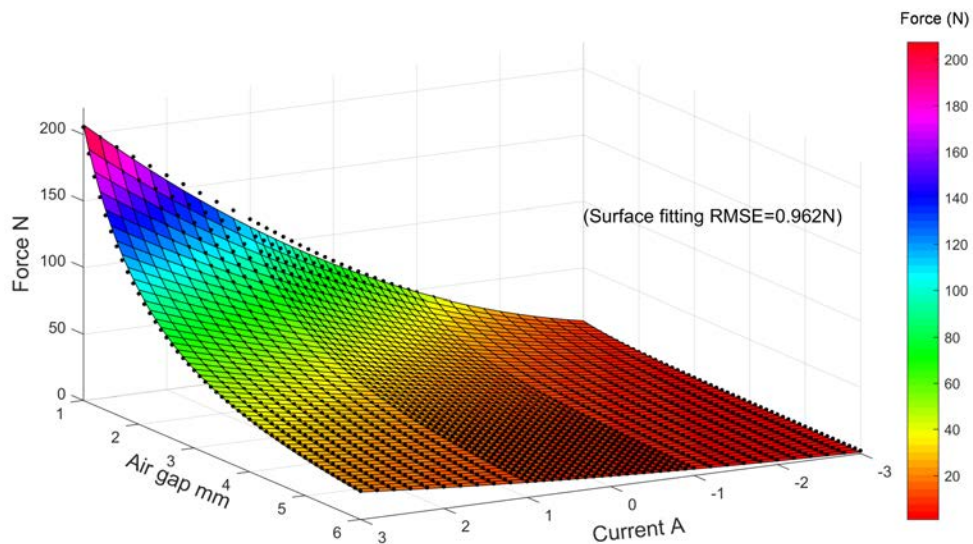
Figure 3.1: FEM analysis data and fitted surface.

can be described by Eq. 3.1. The constant k_m of Eq. 3.1 depends on the permeability of the magnetic flux path, the number of coil winding turns used for the electromagnet and the geometrical shape of the electromagnet and the target.

$$F = k_m \frac{i^2}{g^2} \tag{3.1}$$

Where,

F $\quad=$ Attractive force between electromagnet and soft magnetic steel target

k_m $=$ Constant

i $\quad=$ Current in the coil

g $\quad=$ Air gap between the electromagnet and target

The attractive force of the Eq. 3.1 becomes zero when the coil current is zero. However, HEM exerts an attractive force even when the coil current is zero, due to the presence of the permanent magnet. Therefore, the relationship between air gap, coil current and the attractive force of the HEM can be described by Eq. 3.2 [4]. The constants of Eq. 3.2 were obtained by surface fitting Eq. 3.2 on the data obtained by FEM analysis. The curve fitting toolbox of MATLAB software was used for surface fitting. The color shaded surface shown in fig. 3.1 shows the surface drawn using Eq. 3.2. The root mean squared error (RMSE) of the surface fitting is 0.962N. According to the fig. 3.1, and the RMSE of the surface fitting, the Eq. 3.2 can represent the relationship between air gap, coil current and the attractive force of the HEM to a good accuracy.

Figure 3.2 shows the error of surface fitting in range of $\pm$3A coil current and 1mm to 6mm air gap range. The error of attractive force obtained by FEM data to the attractive force predicted by Eq. 3.2 is less than 6N at any given point.

$$F = a \frac{(i+b)^2}{(z_{ag}+c)^2} \tag{3.2}$$

Where,

16
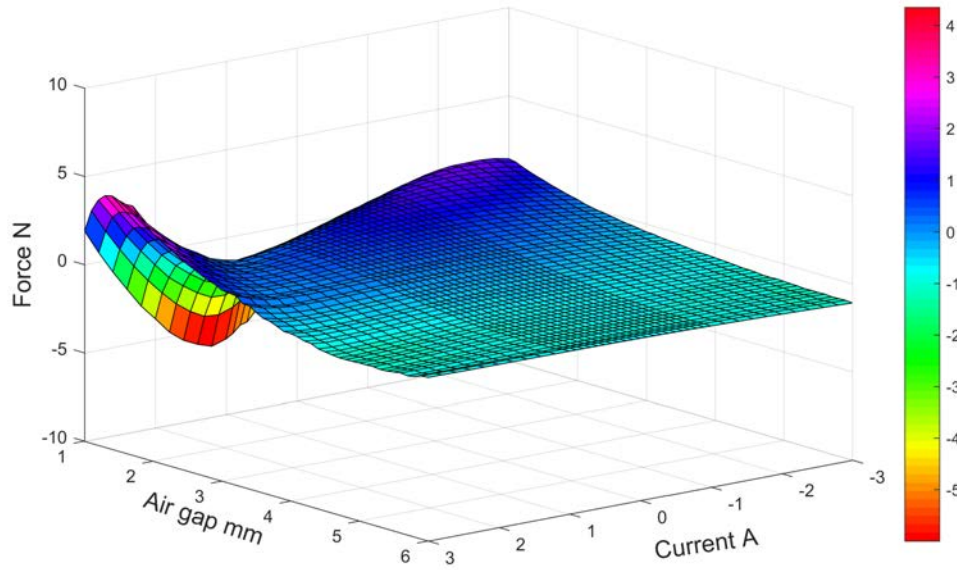
Figure 3.2: Force difference between attractive force predicted by mathematical model and attractive force obtained by FEM analysis.

F = The attractive force between electromagnet and target in Newtons.
i = Current in the coil in Amperes.
z_{ag} = The air gap between the electromagnet and the target in meters.
a = 1.845×10^{-5} Nm^{2}A^{-2}
b = 4.713A
c = 1.3×10^{-3}m

3.2   Lateral forces of Hybrid electromagnet

The previous work done by authors of [1] used rectangular cross section as the guide rail as shown in design D1 in fig. 3.3. The lateral direction (y-direction) motion of the levitated platform was not considered and presented. This is the simplest form of the guide rail. The attractive force described by the Eq. (2) does not depend on the y-direction position of the HEM due to the simple rectangular shape of the guide rail. The linear motion of the levitated platform in the y-direction and the angular motion of the platform around z-axis must be controlled and limited using extra electromagnets as actuators and mechanical limits. The authors of [3, 4, 5] used improved guide rail as shown in the design D2 in fig. 3.3. In design D2, the

17

size of the shown pole length h1 of the HEM and the mating pole length h4 of the guide rail are identical. Furthermore, the length h3 of guide rail and h2 of the HEM shown in fig. 3.3 are identical. If the platform moved in the y-direction, the design D2 could generate lateral force in y-direction opposing lateral movement of the platform from in y-direction. Furthermore, the improved design D2 can generate torque opposing rotation around the z-axis. Therefore, design D2 shown in fig. 3.3 allows passive lateral alignment of the levitated platform.
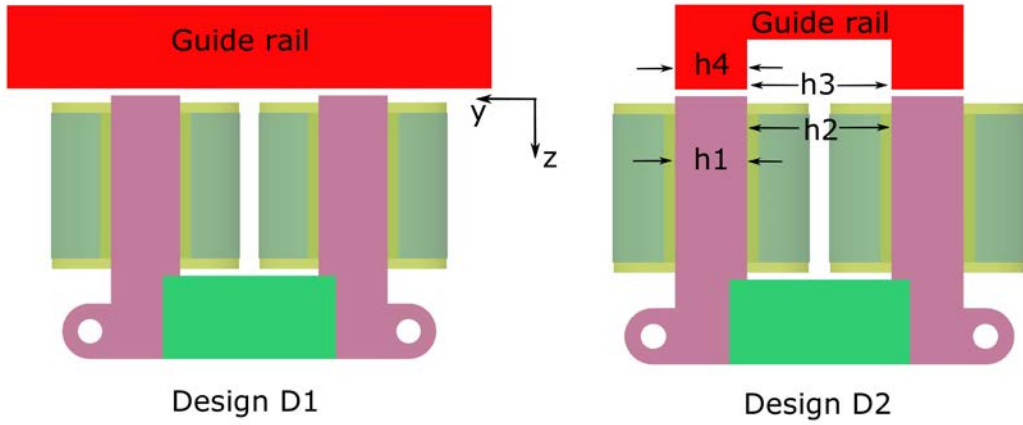
Figure 3.3: Existing hybrid electromagnet and guide rail designs

Figure 3.4 shows a further improved design referred to as design D3. The design D3 has h5 length larger than that of h1. The selected h5 length is large enough to keep the HEMs pole completely within limits of the h5 pole at the maximum allowed lateral displacement of 2 mm. Furthermore, length h6 is slightly larger than length h2. Figure 3.5 shows the y-direction displacement vs. y-direction force of the HEM designs D2 and D3 obtained by FEM analysis. The green line (h6=20mm, h5=10mm) in the fig. 3.5 represents the design D2. According to the results, the force opposing lateral displacement of design D2 is larger than that of design D3. However, the design D3 exhibits a relatively linear relationship between F_y force and displacement in the y-direction. The relatively linear relationship is due to the reduction of edge effects between the guide rail and the HEM in design D3.

Figure 3.6 shows the y-direction displacement vs. attractive force between the HEM and the guide rail. The green line (h6=20mm, h5=10mm) in the fig. 3.6 represents the HEM design D2. According to the results, change in attractive force due to y-direction displacement is much higher in the HEM design D2 compared

18
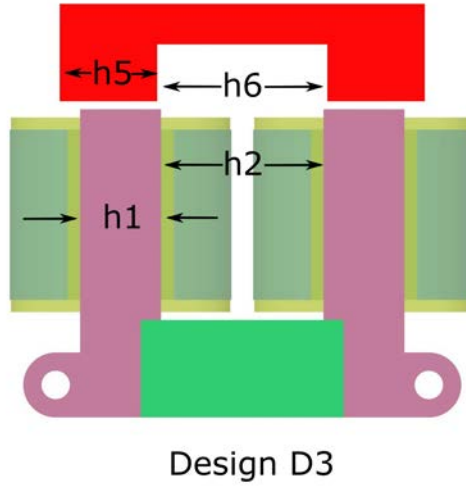
Figure 3.4: Hybrid electromagnet improved design

to the HEM design D3. When the MagLevLS platform is loaded and unloaded, it is not possible to guarantee that the forces experienced by the MagLevLS platform will only be in the z-direction. Therefore, when the platform is loaded and unloaded, the platform will experience vibrations in y-direction due to external forces. These vibrations will cause changes in attractive force as shown in fig. 3.6. These change in forces will cause zero power controller to correct levitated position to reach zero power operation point and will cause vibrations in the z-direction. These vibrations will consume electric power due to the action of zero power controller. The suggested improved HEM design D3 has less effect on attractive force under y-direction displacement of the levitated platform as shown in fig. 3.6. The prototype HEM was fabricated using values 10mm, 20mm, 14mm and 21mm for the parameters h1, h2, h5, and h6 respectively.
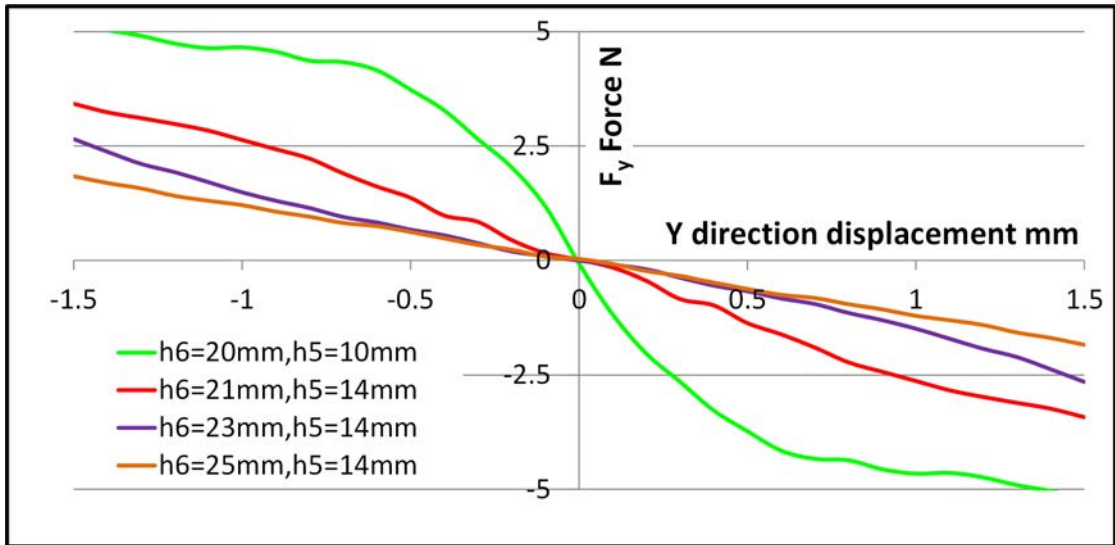
Figure 3.5: y-direction displacement vs. y-direction force of HEM designs D2 and D3. (h1=10mm, h2=20mm)
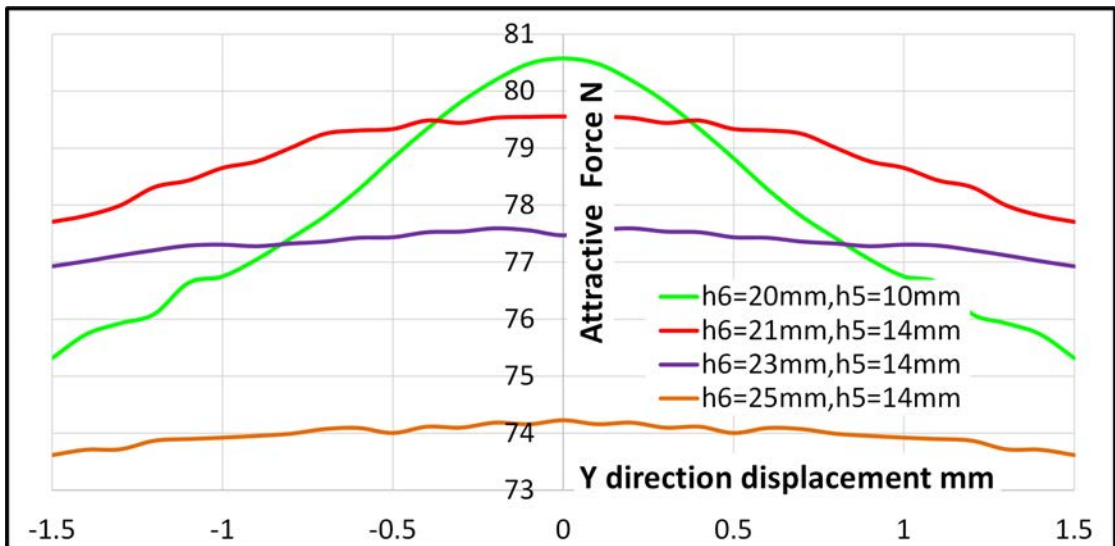
Figure 3.6: y-direction displacement vs. attractive force of HEM designs D2 and D3. (h1=10mm, h2=20mm)

3.3   Linear motor FEM analysis

The designed switched reluctance linear motor uses four electromagnets on the mover and a permanent magnet array in the stator as shown in fig. 2.6. Each electromagnet has two coils connected in series. Each coil has 160 turns and wound using Φ0.5mm copper wire. The internal resistance per coil is 1.2Ω. The magnetic pole surface area of the electromagnet is 6mm×40mm, and the surface area of the mating permanent magnet is 10mm×60mm. The permanent magnet used is Neodymium N35. The starter of the linear motor was manufactured by placing permanent magnets and similar sized SS400 strips as shown in fig. 2.6. The thickness of the permanent magnet and SS400 strips is 3mm, and permanent magnets are magnetized in 3mm direction. The linear motor was powered using the current waveform shown in fig. 3.7. The linear motor completes one driving cycle per 40mm travelling in the x-direction. The driving current of the each electromagnet depends on the relative position of the mover of the linear motor.
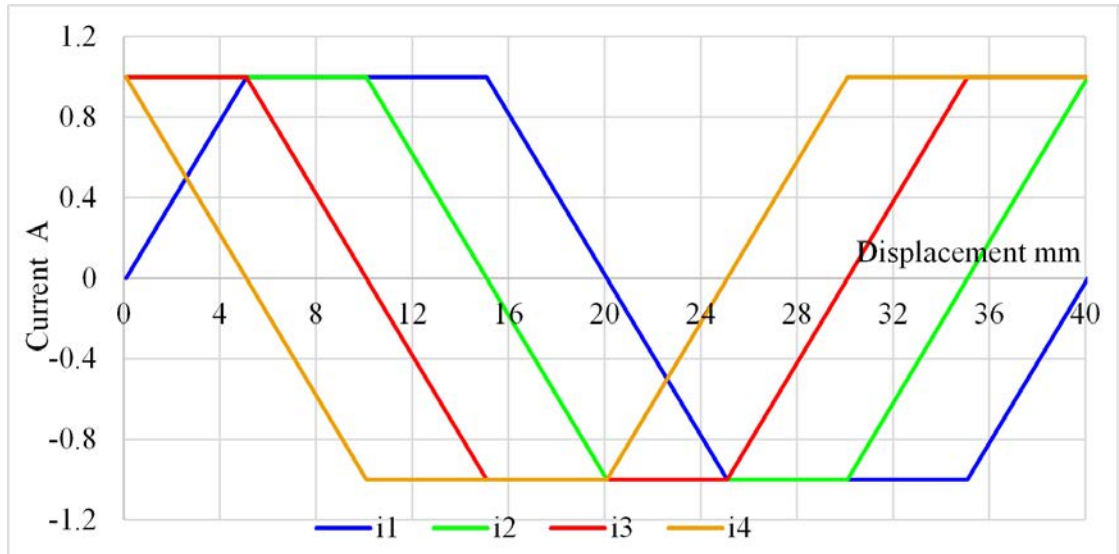
Figure 3.7: Linear motor driving current waveform. i1, i2, i3, and i4 represent current in each electromagnet

Figure 3.8 shows the thrust force generated by the linear motor at several different air gaps. Since the levitated platform has to adjust air gap of levitation based on applied load to achieve zero power levitation, the thrust force at different air gaps are investigated. According to the results, the thrust force is fluctuating, and the thrust force depends on the air gap between the mover and the stator of

the linear motor. Therefore, a position controller will be complicated and needs feedback information about mover position.
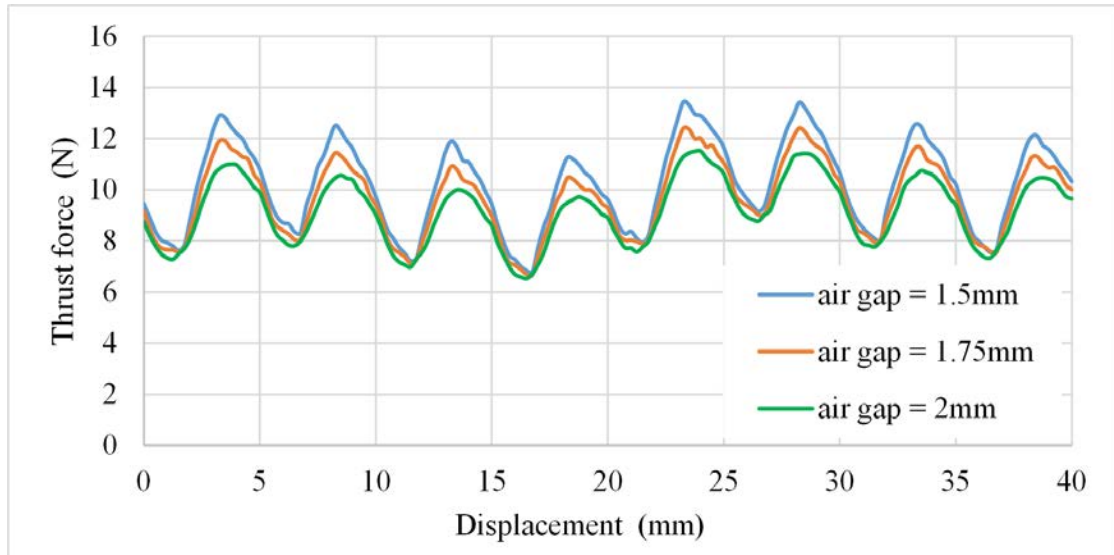
Figure 3.8: Linear motor thrust force at different air gaps.

Chapter 4

Modeling and FEM analysis of the open-end generator.

The first part of this chapter investigates the possibility of using soft magnetic steel cored open-end generator and establishes that the soft magnetic steel cored open-end generator cannot achieve all design requirements based on FEM analysis results. Then the use of ABS (Acrylonitrile-Butadiene-Styrene) as stator core material was suggested and achieved results presented. The ABS core can achieve all design requirements of the open-end generator. Furthermore, ABS achieved better efficiency than soft magnetic steel core because of the absence of eddy currents.

The open-end generator design requires,

- Near zero attractive forces between the rotor and the stator under eccentricities.

- Minimum cogging torque fluctuation.

- Torque that can be supported by HEMs.

- Generate approximately 35W of electric power.

- Minimum of 3mm air gap.

Each of the above plays a vital role in MagLevLS platform. Each HEM can produce up to 2.5N restitutive force per 1mm lateral displacement as shown in fig. 3.5. The attractive forces generated between the rotor and the stator must be smaller than the lateral forces produced by HEMs under y-direction misalignment

to achieve passive lateral alignment of the levitated platform. Therefore, near zero attractive forces between the rotor and the stator under eccentricities are essential. The torque experienced by the stator of the open-end generator is transferred to the levitated platform. If the torque exhibits fluctuations, the platform will experience vibrations around roll axis (x-axis), and will require a complex controller to suppress vibrations and achieve levitation. The cogging effect is one of the major factors that affect torque fluctuations. Therefore, it is preferred to minimize cogging torque fluctuations of the open-end generator. The total amount of torque experienced by the levitated platform must be supported by force difference of the HEMs. In order to reach zero power levitation position, the HEMs must change air gap to achieve required attractive force difference between HEMs and guide rail. If the torque is large, a large air gap difference will be required and that will introduce large roll angle at steady state of the levitated platform. Therefore is important to reduce torque generated by the open-end generator. The levitated platform requires approximately 35W of electrical power to achieve continuous levitation in the prototype system. The levitated platform must reach zero power levitation position based on the load on the platform. Furthermore, loading and unloading platform will change levitated air gap during transient states. Therefore, a larger air gap is required between the rotor and the stator of the open-end generator so that the rotor will not touch the stator during transient states or steady states of operation.

The open-end generator design was improved in several stages based on FEM analysis data and design requirements of the MagLevLS platform. The maximum diameter of the open-end generator core and the length of the core in the x-direction (refer to fig. 2.5) was limited to 95mm and 100mm respectively, based on the geometrical constraints of the designed prototype MagLevLS platform. Figure 4.1 shows the major dimensions of the selected open-end generator for prototype fabrication. The open-end generator designs analyzed in this chapter uses N35 permanent magnets which has dimensions 3mm×10mm×60mm and magnetized in 3mm direction.

A generator or an alternator has its rotor and stator core axis aligned in the same line, and the axes are identical. This arrangement is always maintained using bearings to fix the relative position of the core and the rotor of the generator. However, due to the levitated nature of the MagLevLS platform, it is impossible to align and maintain the open-end generator core axis and rotor axis to the
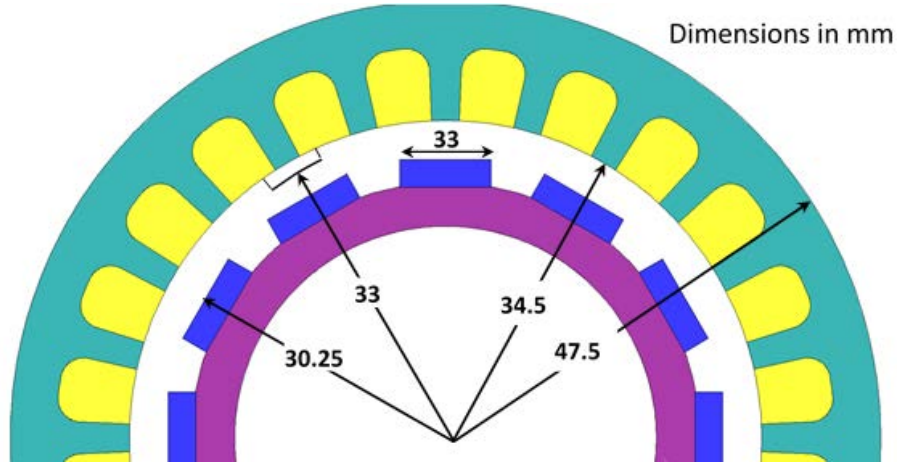
Figure 4.1: Major dimensions of the selected open-end generator for prototype fabrication.

same line during operation of the MagLevLS system. When there is misalignment between the rotor axis and the core axis, large cogging torques and cogging forces are induced between the open-end generator core and the rotor. In order to achieve zero power levitation, these cogging torques and forces must be reduced to a limit that can be handled by HEMs. It is advantageous for a regular generator to reduce the air gap to increase the amount of power generated. However, the proposed open-end generator requires a larger air gap compared to a similar-sized regular generator to achieve levitation under different levitated loads while satisfying zero power operation condition.

4.1 FEM analysis of open-end generators with soft magnetic steel stator core

Figure 4.2 shows two of the analyzed open-end generator designs. The design D1 has permanent magnets completely buried (3mm) in the rotor. The permanent magnets of the design D2 are buried 1mm into the rotor. The air gap between the rotor and the core is 2.5mm for both designs. In order to achieve the same 3.6mm air gap, the rotor diameters of the designs were adjusted. (i.e. The positions of the permanent magnets relative to the stator core is identical in both designs.). For the FEM analysis, three phase coil windings were used. Electric power produced by the open-end generator was rectified using three phase rectifier bridge and external load resistors were used to measure the power dissipation under external

loads. Each phase of the coil winding has 30 turns, and internal resistance per phase is 0.6Ω. The rotor and the core used SS400 as the construction material. The permanent magnets were the N35 type with 3mm×10mm×60mm dimensions and were magnetized in 3mm direction. The open-end generator cross section shown in fig. 4.2 shows 3mm×10mm cross section of the permanent magnets. Both designs have 24 core slots for coil windings and the approximate area of a slot in shown cross section is $45.4mm^2$. The rotor was rotated at a rotational speed of 1600 rpm for the analysis. The core of the open-end generators used for the FEM analysis was laminated and the used lamination factor was 0.94.
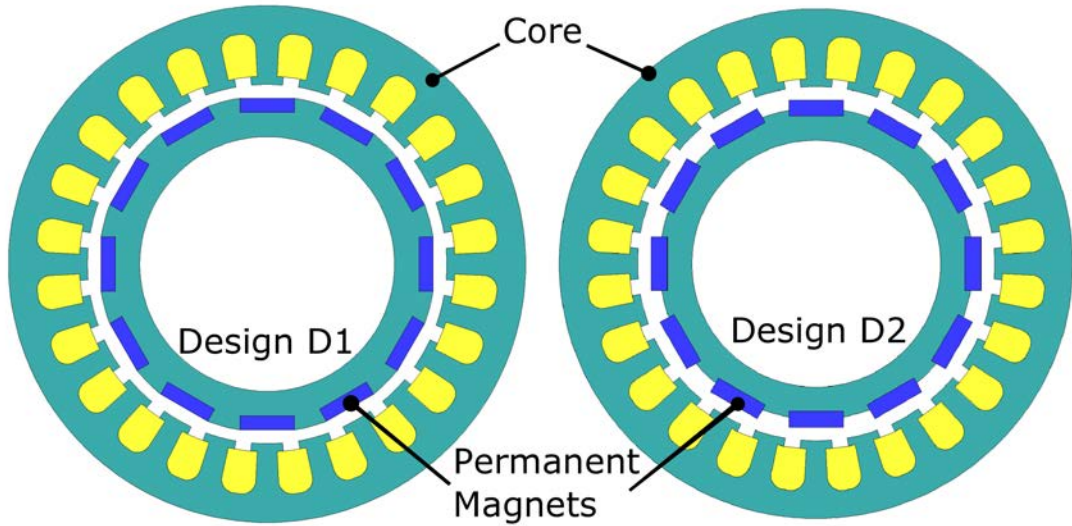
Figure 4.2: open-end generator design D1 and design D2. The design D1 has permanent magnets completely buried (3mm) in the rotor. The permanent magnets of the design D2 are buried 1mm in to the rotor.

During the FEM analysis, the diameter of the copper wire used for coil winding was selected to withstand the currents produced in the copper windings. The number of turns per phase used for the FEM analysis was selected to reflect the number of physically possible turn count based on the diameter of the copper coil and the cross-sectional area of a slot. The presented data represents most promising designs for the open-end generator.

Figure 4.3 shows the cogging forces generated by the open-end generator design D1 and design D2. According to the results, the open-end generator design D1 with buried permanent magnets generate less cogging forces compared to the design D2 at similar rotor eccentricities. When the rotor eccentricity is 0.5mm, root mean

square (RMS) cogging force of design D1 is 132N while that of design D2 is 181N. However, the cogging forces generated by both designs are large compared to the forces generated by HEMs. The peak to peak fluctuation of cogging forces is approximately similar in both designs. The large cogging forces are primarily due to the use of permanent magnet rotor with a soft magnetic steel core.
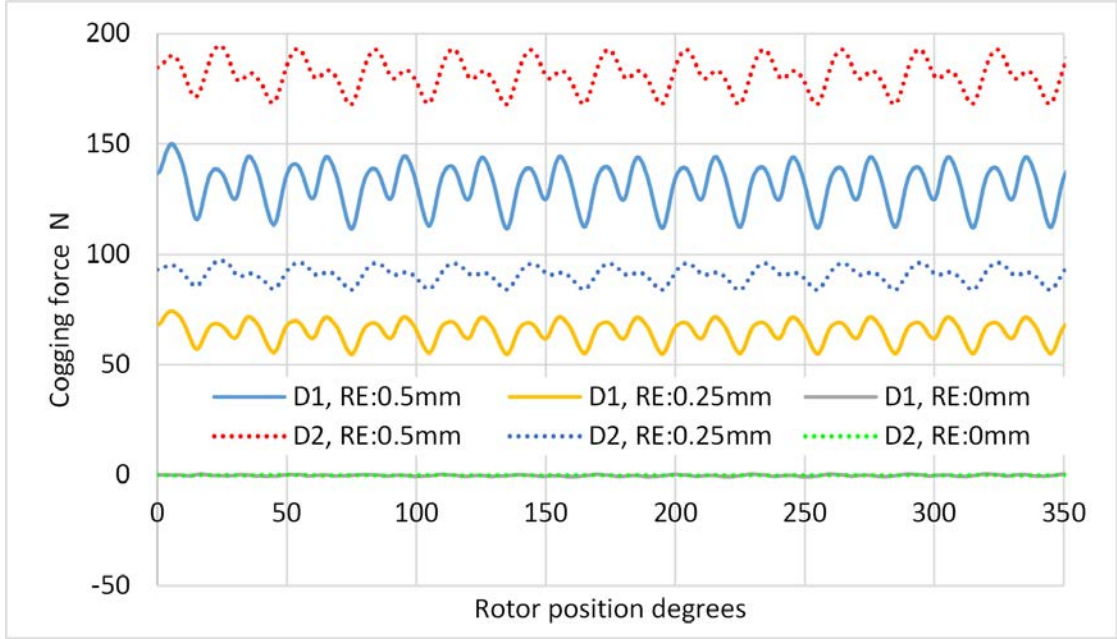
Figure 4.3: Cogging forces generated due to rotor eccentricity (RE) of the open-end generator designs D1 and D2.

Figure 4.4 shows the electric power dissipated through a 1Ω load resistor when the open-end generator rotor was operated at 1600rpm. The results suggest that the change in electric power dissipation due to the rotor eccentricity is negligible. The open-end generator design D1 can dissipate approximately 119W RMS electric power across 1Ω load while the design D2 can dissipate approximately 234W RMS electric power. These results show that the use of permanent magnets mounted on the surface of the rotor as in design D2 can generate approximately twice the amount of power compared to design D1. The increase in cogging force due to the surface mounted permanent magnets is approximately 37.5%. Therefore, the design D2 is more suitable for the MagLevLS platform design. The changes in electric power dissipation and cogging forces in design D1 and design D2 is explained by magnetic flux paths. Figure 4.5 shows several magnetic flux lines and magnetic flux density plot of the open-end generator design D1 obtained using

27

FEM analysis. The magnetic flux lines inside the highlighted region in red shows that there are some closed flux paths exists completely inside the rotor. When the permanent magnets are mounted on the surface of the rotor the highlighted region of the rotor is eliminated. Since the highlighted high relative permeability region does not exist in design D2, most of the magnetic flux paths are closed through the air gap and the stator core of the open-end generator. Therefore, the amount of magnetic flux experienced by the windings is increased. This increase in magnetic flux experienced by the windings increases electric power generation. Furthermore, increase in magnetic flux experienced by the soft magnetic steel core increases cogging forces as seen in fig. 4.3.
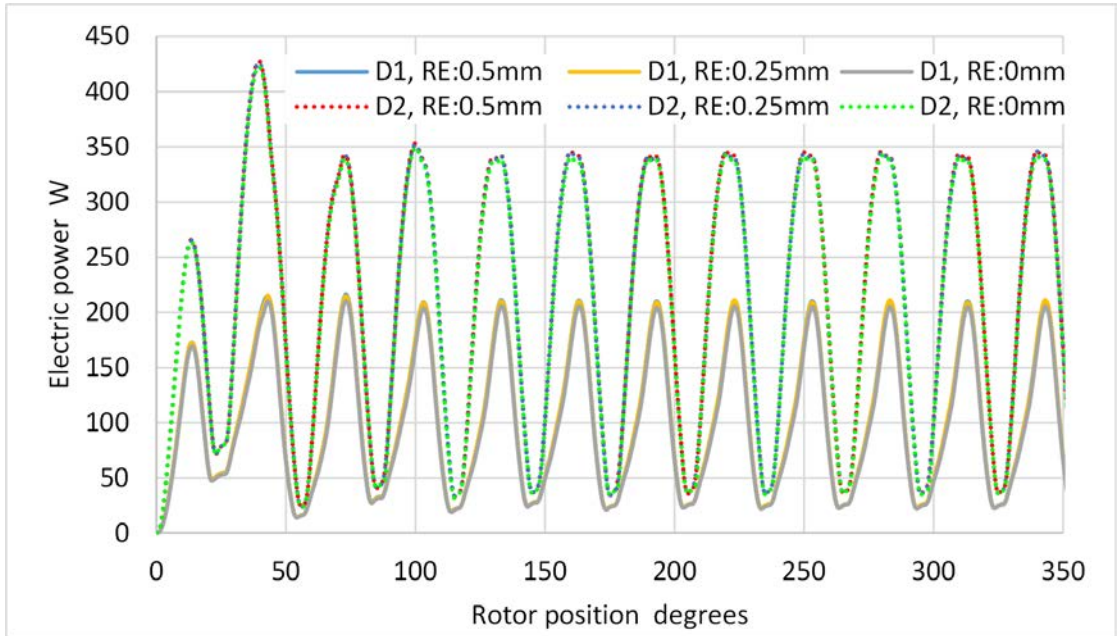
Figure 4.4: Electric power dissipation across 1Ω load resistor at different rotor eccentricities (RE) of the open-end generator designs D1 and D2.

The magnetic flux density plot and magnetic flux path analysis of the open-end generator design D2 are shown in fig. 4.6. The magnetic flux paths exist in some rotor positions does not go through the copper windings in the generator core. The highlighted region in fig. 4.6 shows some of the magnetic flux paths which do not go through the windings. Furthermore, the change in the air gap between the permanent magnets and the core due to the physical shape of the core contribute to the fluctuations of cogging force depending on the rotor position.

Further analysis was performed by increasing the cross-sectional area of the
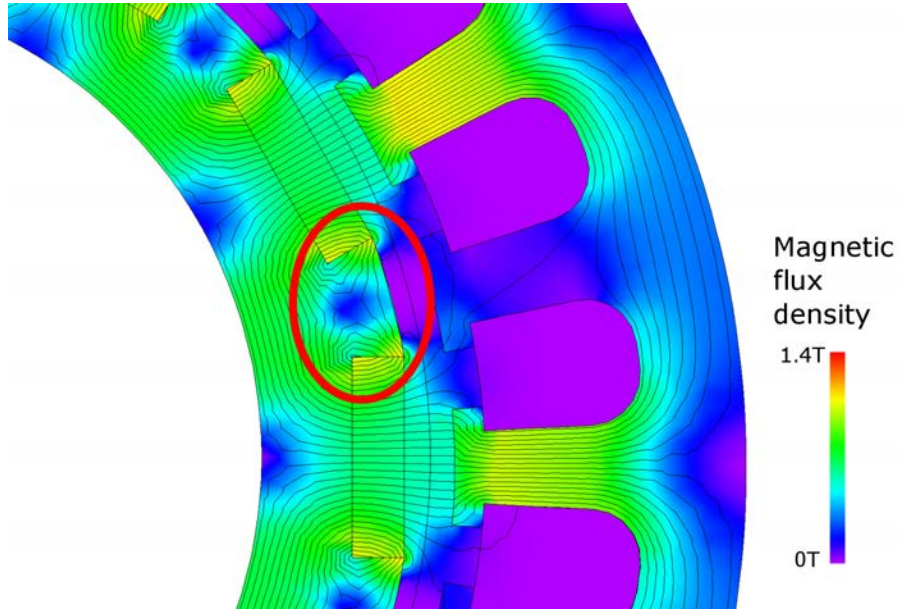
Figure 4.5: Magnetic flux lines and magnetic flux density plot of the open-end generator design D1 obtained using FEM analysis.

core slots, increasing and decreasing the core slot count and the rotor pole pair count. The design D2 was improved by increasing the cross-sectional area of a slot to $50.8mm^2$ and by slightly reducing the copper wire diameter used for the winding. The number of turns per phase is increased to 40 turns in improved design D2. The consequent FEM analysis revealed that the improved open-end generator can dissipate 184W RMS electric power through a 1Ω load resistor. The RMS cogging force was 146N at 0.5mm rotor eccentricity for the improved open-end generator. The non-sinusoidal waveforms of the power dissipation and cogging forces suggest that the phases of the open-end generator is overlapped and not at 120-degree phase angles. However, due to the use of readily available, simple rectangular cuboid permanent magnets for the rotor, and the physical constraints of the MagLevLS platform it is not possible to arrange phases at 120-degree phase angles. However, it is possible to overcome the difficulties due to the uneven phase angles by using an external electronic circuit to match phase angles. The open-end generator design D3 was obtained by slightly modifying the physical shape of the cross section of the core. The resulted design D3 is shown in the fig. 4.7. The red circle highlights the change made to the design D2 to obtain design D3. The design D3 uses three phase winding, and external 1Ω load was connected through a three phase bridge rectifier. Each phase of the winding has 40 turns. Figure 4.8

29

shows the cogging forces observed in open-end generator design D3. The results suggest that the removal of highlighted SS400 part compared to the open-end generator design D2 reduces cogging force to less than 60N. Furthermore, the air gap is increased to 3.6mm. The reduction of cogging force can be attributed to increasing of air gap.
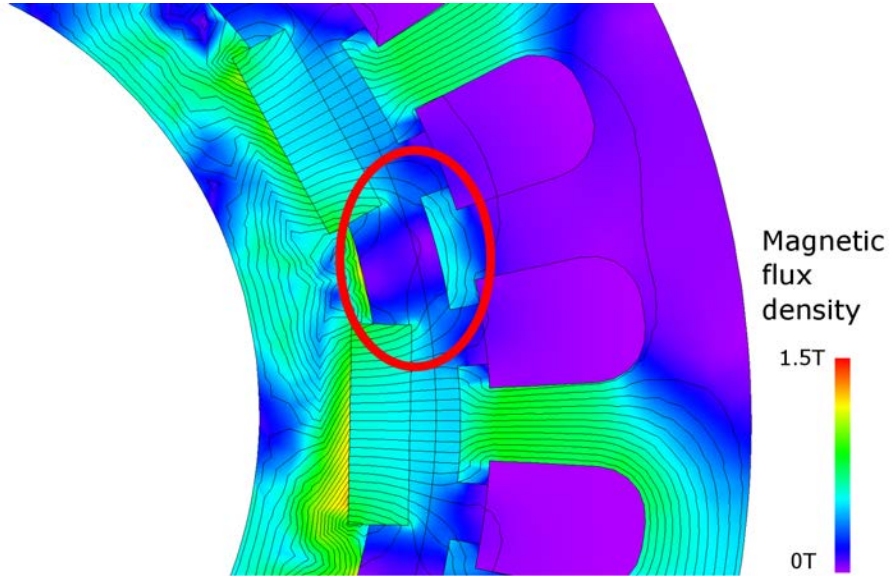
Figure 4.6: Magnetic flux lines and magnetic flux density plot of the open-end generator design D2 obtained using FEM analysis.

Figure 4.11 shows the power dissipation through a 1Ω load resistor of the open-end generator design D3. According to the results, RMS power generated was approximately 147W. Compared to the open-end generator design D2, the open-end generator design D3s reduction of power generation is approximately 37W. However, the open-end generator design D2 has approximately 240% more cogging force compared to the open-end generator design D3 at 0.5mm rotor eccentricity. Furthermore, the change of power generation due to rotor eccentricity was negligible as seen in fig. 4.11.

The x-direction length of the stator core of open-end generator designs D1, D2, and D3 can be changed to achieve the same amount of electrical power from all three designs. This allows convenient comparison of the attractive force between the rotor and the stator of the open-end generator under eccentricities. Figure 4.9 shows the attractive forces obtained from FEM analysis of open-end generator designs D1, D2, and D3 when each generator is producing approximately 119W rms electrical power. All three designs used three phase windings and 1600 rpm rotor
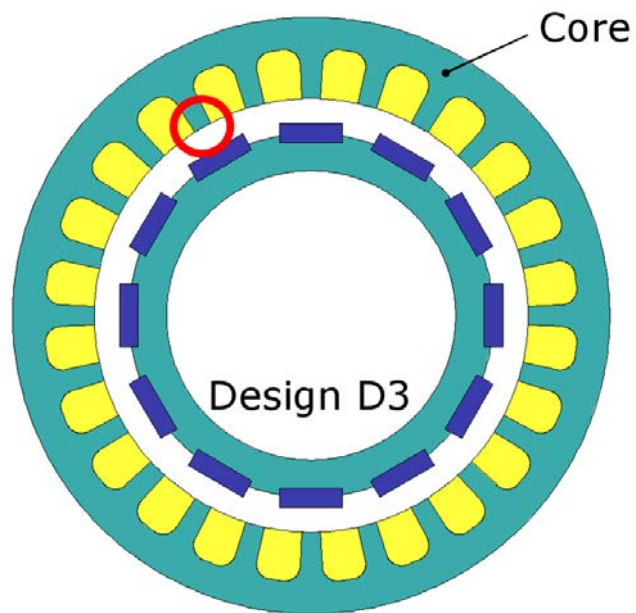
Figure 4.7: open-end generator design D3.
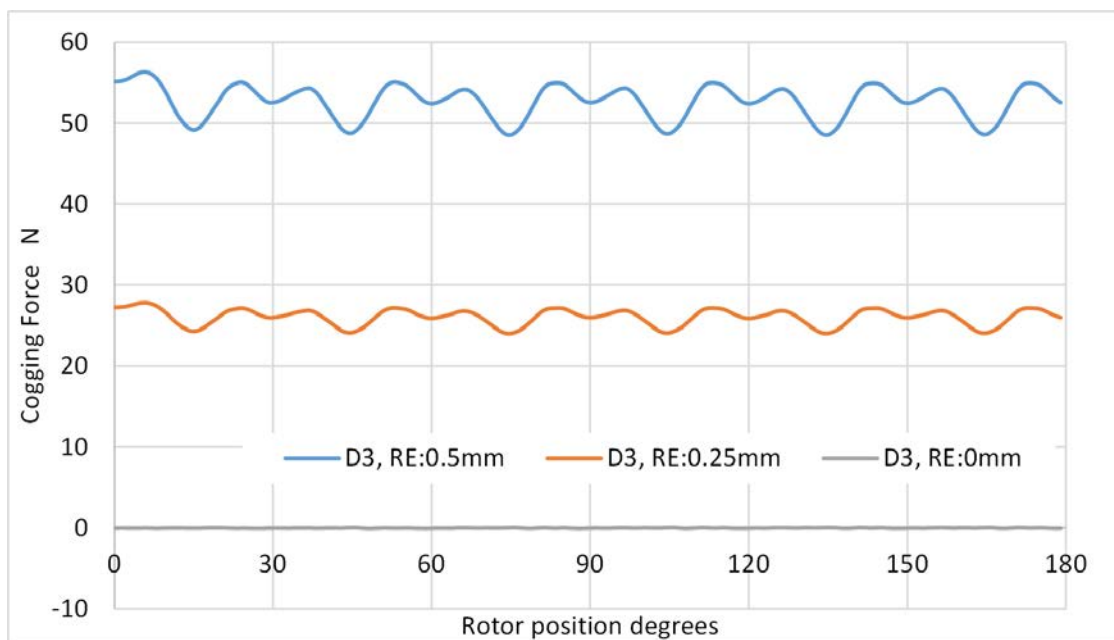
Figure 4.8: Cogging forces generated due to rotor eccentricity (RE) of the open-end generator design D3.

speed. Furthermore, it is possible to change the amount of power produced by the open-end generator by changing rotor speed. However, change to the attractive force between the rotor and the stator due to rotor eccentricity is minimum when the rotor speed is changed. (i.e ex. 100rpm and 2000rpm rotor speed produce vastly different electrical power. However, the attractive force is not changed significantly for a given rotor eccentricity value due to the change of rotor speed.) Figure 4.10 shows the rotor torque while open-end generator designs D1, D2, and D3 produce approximately 119W rms electrical power. According to the fig. 4.10, the open-end generator design D3 produce less torque fluctuation than design D1 and D2. Since the open-end generator, D3 produce a less attractive force between the rotor and the stator at a given rotor eccentricity and torque fluctuation is less, the design D3 is more suitable for the MagLevLS platform.
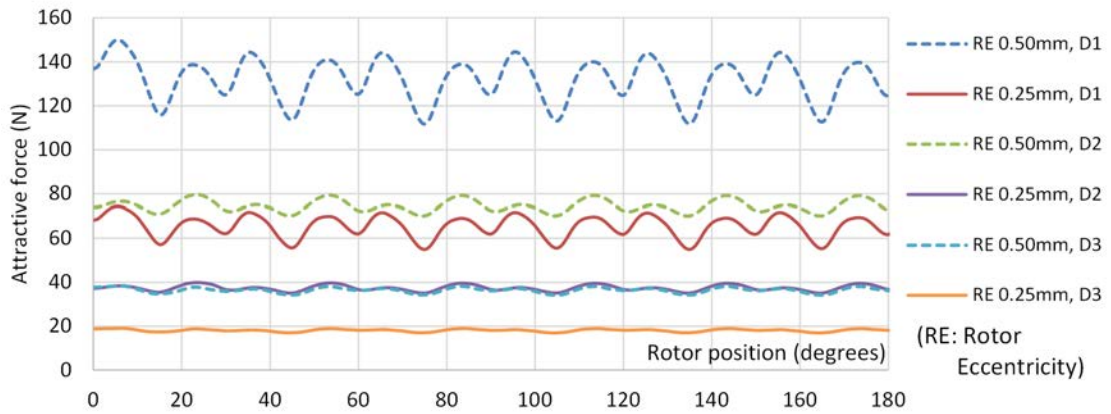
Figure 4.9: Attractive force between the rotor and the stator vs rotor position while all generators produce approximately same (119W) rms power. (1600rpm, 3 phase winding)

The open-end generator design D3 was improved by changing the coil winding to two phase based on FEM analysis results of the open-end generator designs D1, D2, and D3 to obtain the open-end generator design D4. The physical shape of the rotor and the core was identical to the open-end generator design D3 shown in fig. 4.7. After performing several FEM analysis passes, the winding was set to two phase winding with 24 turns per phase. The rotor speed was reduced to 600rpm. The internal resistance per winding was 0.3Ω. The power dissipation was measured through a 1Ω load resistor and a rectifier bridge.

Figure 4.12 shows the cogging forces observed from open-end generator design
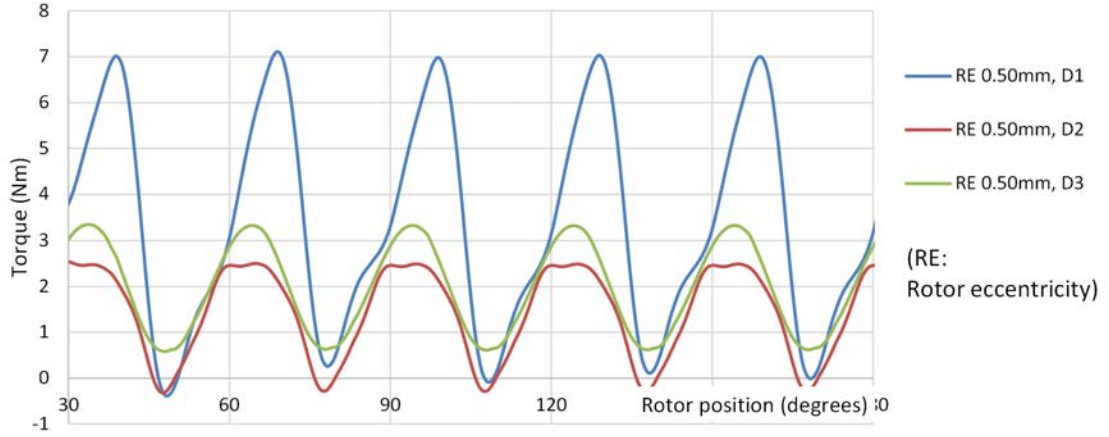
Figure 4.10: Torque vs rotor position of the open-end generator. (1600rpm, 3 phase winding)

D4. The results show that the cogging forces are not significantly changed from design D3 to design D4 when the core length in x-direction is same (100mm). However, as shown in fig. 4.13, electrical power dissipated through 1Ω load resistor was increased to 162W RMS. Furthermore, the electrical power dissipation and cogging forces exhibit approximately sinusoidal waveforms suggesting better phase angle arrangement than open-end generator design D1, D2, and D3. Therefore, the open-end generator design D4 having two phase coil windings is more suitable for MagLevLS platform based on reduced rotor speed, preferable cogging force, and power dissipation characteristics.

The open-end generator design D4 was analyzed to obtain the relationship between rotor angular position, rotor eccentricity, and cogging force. Equation 4.1 shows the obtained relationship by surface fitting FEM analysis data. The blue dots in the fig. 4.14 represent the obtained data points using FEM, and the shaded surface represents the cogging forces obtained using Eq. 4.1. It is possible to eliminate the constant u in Eq. 4.1 by selecting the stator core and the rotor relative start positions.

$$F_p(\gamma, y) = y(s + w \times \sin(12(\gamma+u))) \tag{4.1}$$

Where,
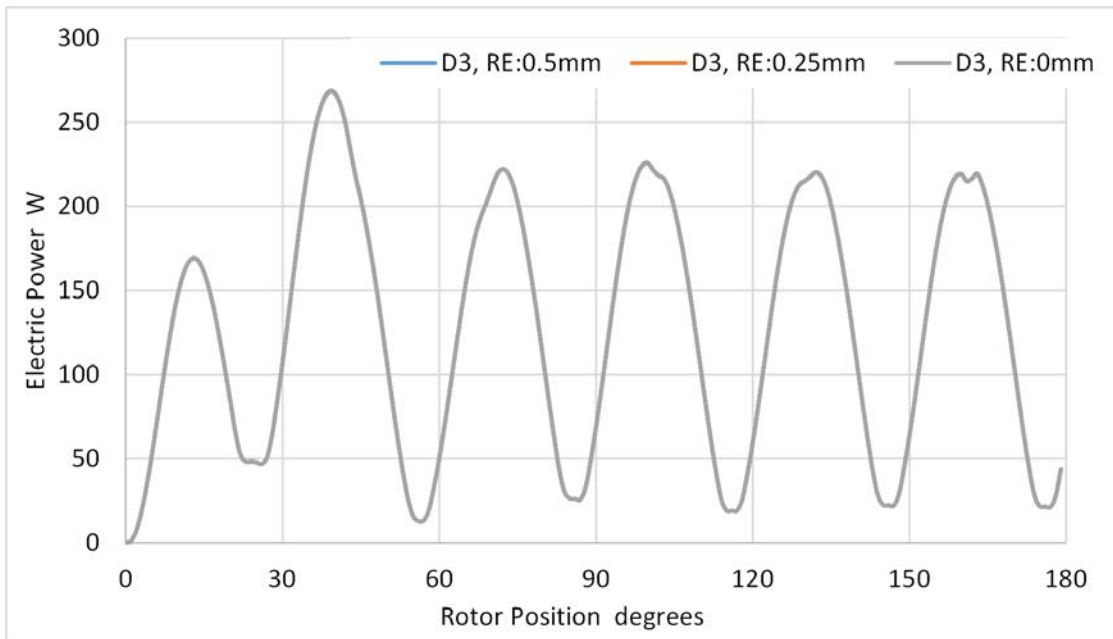
Figure 4.11: Electric power dissipation across 1Ω load resistor at different rotor eccentricities (RE) of the open-end generator design D3.
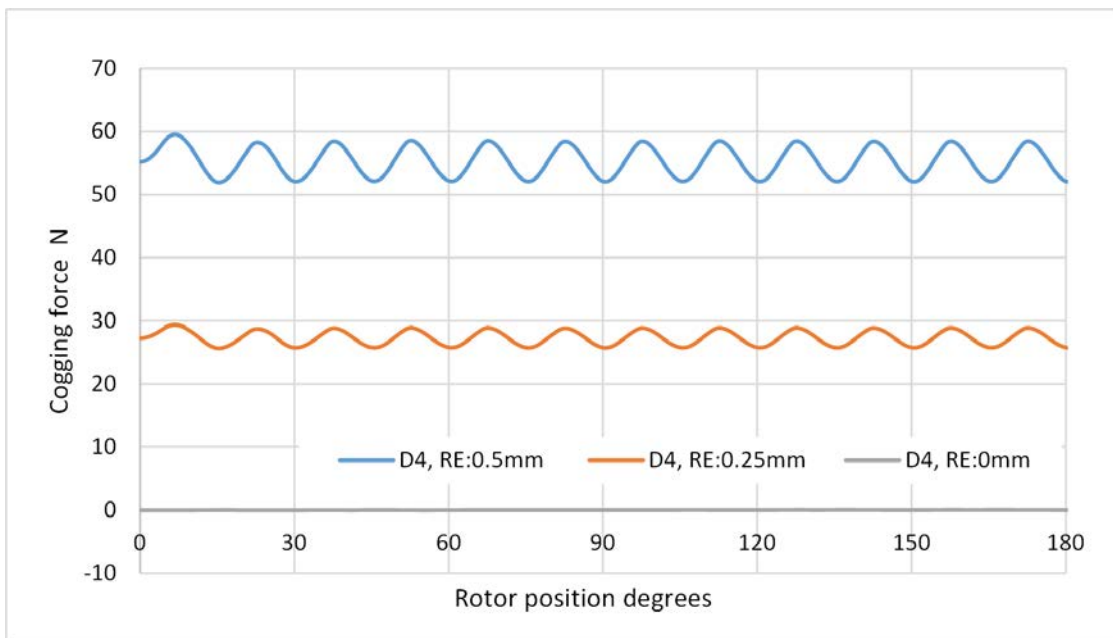
Figure 4.12: Cogging forces generated due to the rotor eccentricity (RE) of the open-end generator design D4.
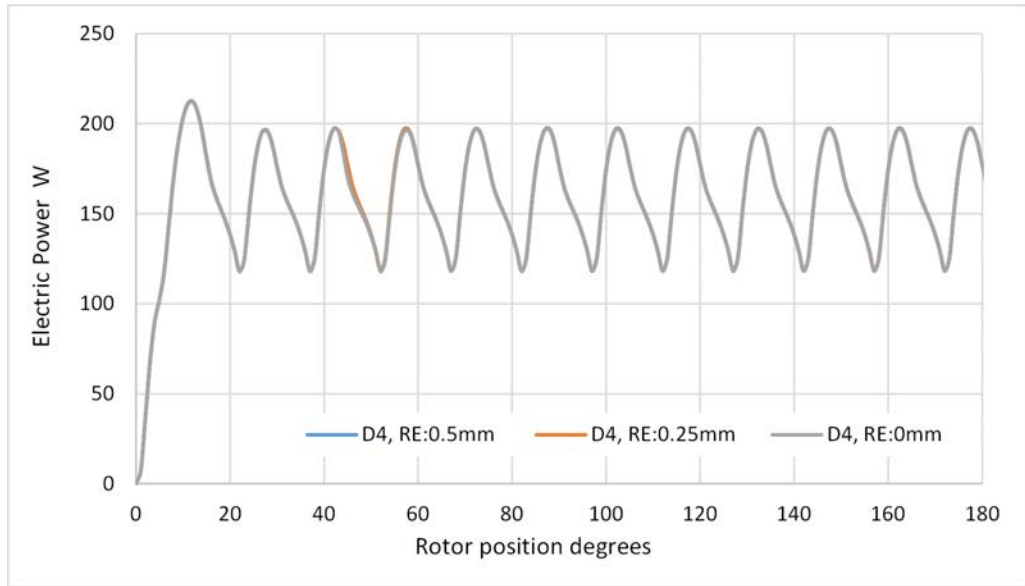
Figure 4.13: Electric power dissipation across 1Ω load resistor at different rotor eccentricities (RE) of the open-end generator design D4.
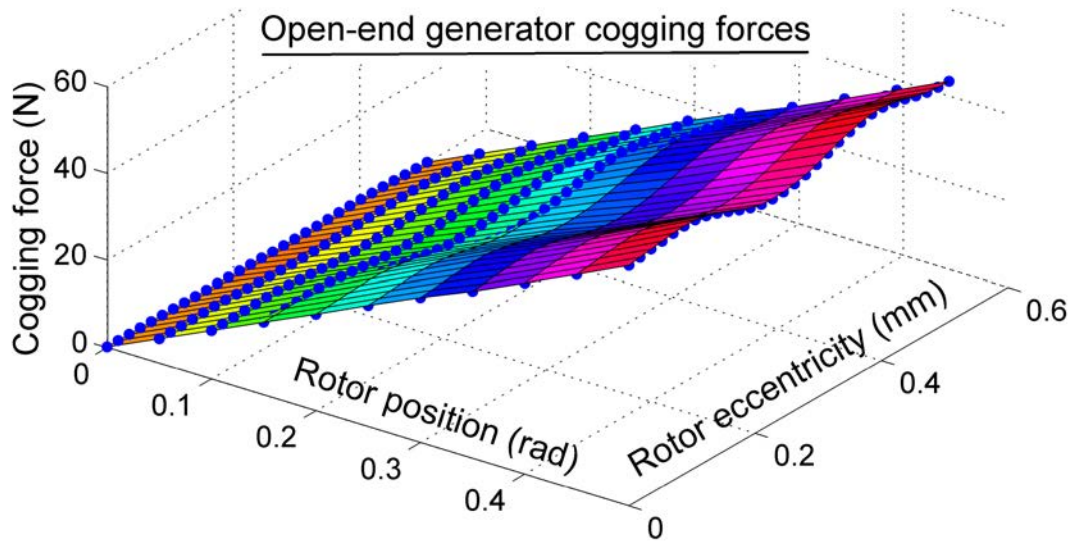
Figure 4.14: Relationship between rotor position, rotor eccentricity and cogging force of the open-end generator design D4.

$\mathrm{F}_p(\gamma, y)$ = Cogging force in N

γ = Rotor angular position in radians

y   = Rotor eccentricity in mm

s   = 116.5 Nmm^{-1}

w   = -6.84 Nmm^{-1}

u   = -1.37 rad

All of the open-end generator designs analyzed using SS400 as core material generate large cogging forces and cannot be compensated by lateral forces generated by HEMs. The maximum amount of allowable cogging force in the lateral (along the y-axis) direction of the MagLevLS platform is approximately 7N at 0.5mm displacement as shown in fig. 3.5. The open-end generator design D4 can generate up to 60N cogging force as shown in fig. 4.12. The amount of expected power from the open-end generator was approximately 35W. However, the open-end generator design D4 can dissipate approximately 162W RMS electric power through a 1Ω external load.

4.2 FEM analysis of open-end generators with ABS stator core

The open-end generator design D5 was constructed based on the open-end generator design D4. The physical dimensions of the generator core and the rotor are identical to the open-end generator design D3. The core construction material of the open-end generator was changed to ABS in design D5. It is expected to eliminate cogging forces of the open-end generator since the relative permeability of ABS is close to 1 and ABS is non-ferromagnetic. The expected forces are Lorentz forces due to electromagnetic induction. The use of ABS as core material closely approximate core-less machine and the amount of electric power generated in windings are reduced. Since the current passing through windings is reduced due to the use of ABS as the core material, it is possible to decrease the diameter of the copper wire used for winding. The open-end generator design D5 has two phase winding with 120 turns per phase. Each winding was connected to a separate load resistor to avoid losses due to phase overlapping. It is expected to feed electric power generated from the open-end generator to the MagLevLS platform through a phase correction and regulation circuit. The use of ABS to manufacture

core facilitates convenient coil winding and generator construction compared to a stator coreless generator.

Figure 4.15 shows the cogging forces obtained by analyzing open-end generator design D5 at several rotor eccentricity values. The results suggest that the cogging force is a restitutive force. The non-uniform nature of the cogging force seen at 3mm rotor eccentricity in fig. 4.15 is due to the element sizes used in FEM analysis. This effect is not clearly visible when the rotor eccentricity is smaller. The open-end generator designs utilize SS400 as the core construction material had attractive force as the cogging force. Therefore, the lateral forces generated by HEMs must compensate for cogging forces in the y-direction to maintain lateral alignment. However, when ABS used as the core material, cogging force become a restitutive force and therefore, cogging force supports lateral force generated by HEMs to maintain lateral alignment. Therefore, use of ABS is advantageous for passive lateral alignment.
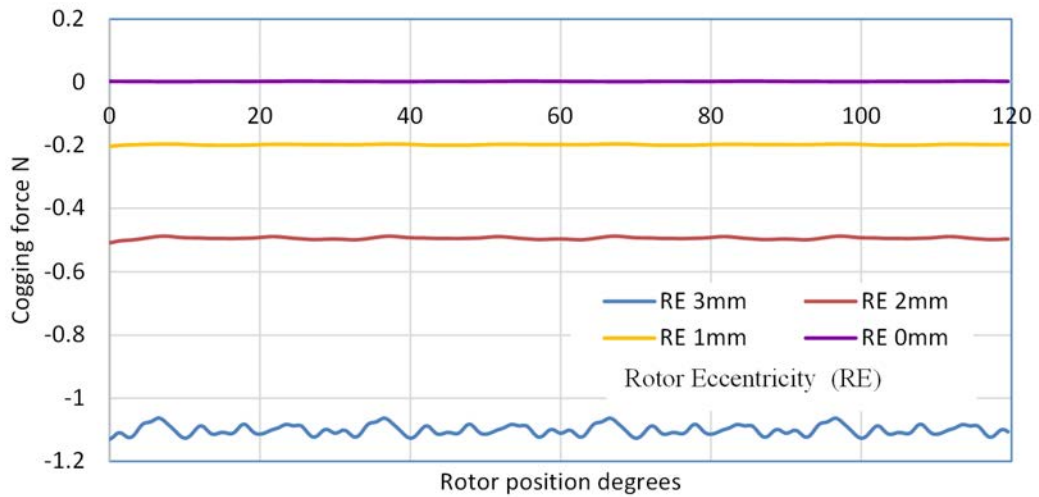
Figure 4.15: Cogging force between the open-end generator core and the rotor of the design D5 obtained by FEM analysis. The core material used is ABS. Positive force represents an attractive force between the core and the rotor.

Figure 4.16 shows the electrical power produced by one winding of the open-end generator at 800 rpm rotor speed. The internal resistance of each winding of the open-end generator is 19Ω, and therefore, 19Ω load resistor was used to measure power dissipation. According to the results, single winding can dissipate RMS power of 12.2 W using ABS core. Therefore, it is possible to obtain 24.4 W electric power using ABS core open-end generator using both windings. Although

the SS400 core can generate more power, it is not feasible to use SS400 stator core for the open-end generator due to large cogging forces. The results presented in fig. 4.16 suggest that the rotor eccentricity does not significantly affect the amount of power generated by the generator when ABS used as the core material. This is an advantage for the levitated platform because the open-end generator can supply the same amount of power to the platform regardless of its levitated air gap.
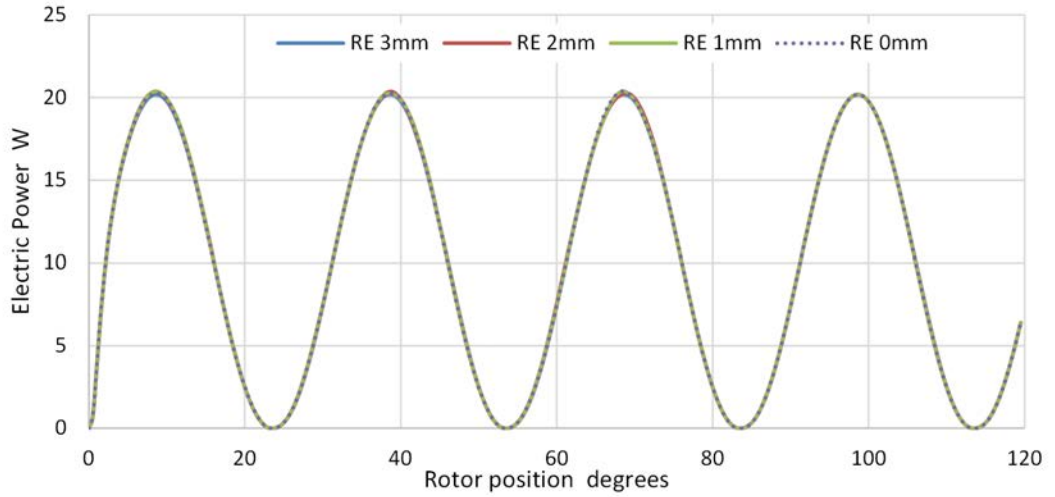
Figure 4.16: Electric power generation of the open-end generator design D5. Figure shows electric power dissipated through a 19 Ω load while the rotor of the open-end generator is rotated at 800 rpm. Each coil of the open-end generator is connected to separate a 19 Ω load. The graph shows power dissipation through one load resistor.

Figure 4.17 shows the electrical power dissipation through a 19Ω load resistor at several rotor speeds. The rotor eccentricity was kept at 2mm for the analysis. According to the results, 1000rpm rotor speed can dissipate approximately 19.3W RMS power through a 19Ω external load using one phase winding. Therefore, it is possible to use open-end generator to produce expected electric power of 35W by utilizing both windings. The frequency of the sine AC waveform depends on the rotor rpm and can be described by Eq. 4.2.

$$f = \frac{r \times p}{60} \tag{4.2}$$

Where,

f = Sine wave frequency of electric power in Hz

r = Rotor speed in rpm

p = Pole pair count of the rotor. (i.e. 6)
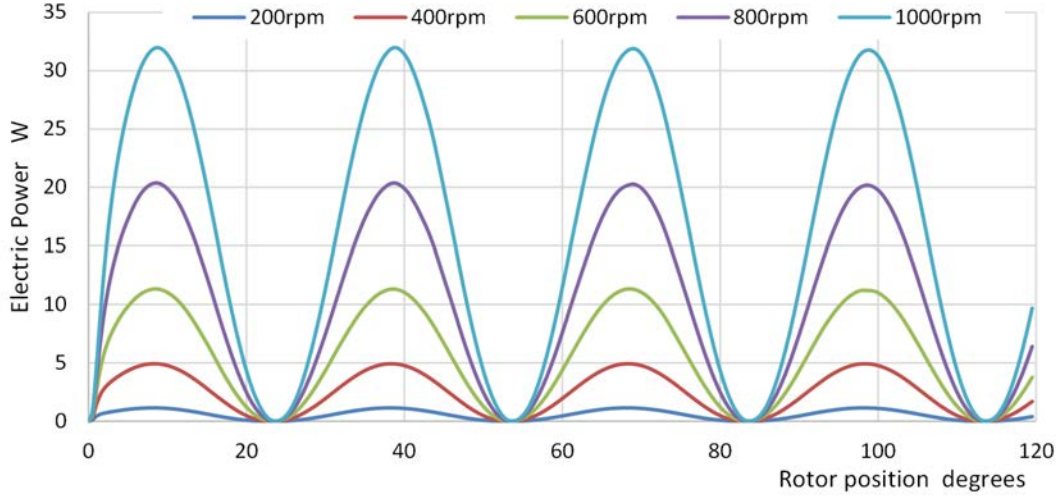
Figure 4.17: Electric power generation of the open-end generator design D5. Figure shows electric power dissipated through a 19 Ω load while the rotor of the open-end generator is rotated at several speeds. Each coil of the open-end generator is connected to separate a 19 Ω load. The graph shows power dissipation through one load resistor.

Figure 4.18 shows the torque observed from three different open-end generators. All three open-end generators produce approximately 24W rms electrical power and have two phase winding. Furthermore, all three generators shown in fig. 4.18 uses generator profile similar to design D3. In order to obtain same 24W power from all 3 designs, the x-direction length, the rotor speed and the stator core construction material was changed as shown in the fig. 4.18 legend. The provided torque values were observed when the rotor and the stator have 2 mm eccentricity. The results shown in fig. 4.18 suggest that the ABS stator core produces minimum torque fluctuation during the operation of the generator. Furthermore, the ABS stator core requires minimum torque to produce 24W rms electrical power.

Figure 4.19 shows the cogging torque generated by the open-end generator around the x-axis. The cogging torque increases with decreasing external load resistance according to the FEM analysis results. When the external load resistance decreases, the amount of current passing through the circuit increases and therefore the Lorentz forces generated in the generator increases. Hence, the cog-
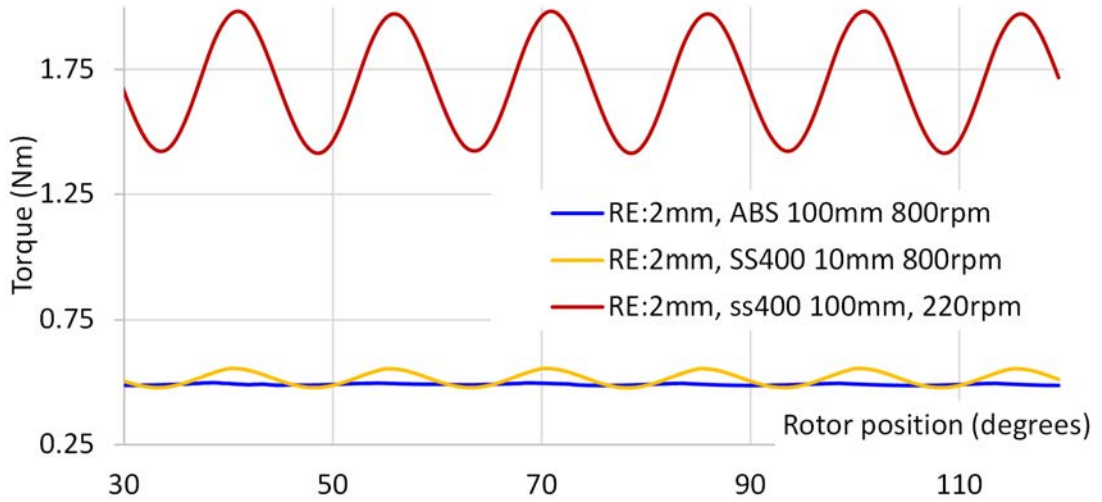
Figure 4.18: Torque comparison of open-end generators. All three generators produce approximately 24W rms electric power

ging torque generated due to the Lorentz forces increases as shown. The cogging torque exhibits a nearly sinusoidal waveform with a peak to peak difference of 0.015Nm for 19Ω external load as shown in fig. 4.19. Therefore, when ABS is used as the core material with 19Ω external load, the force difference required to overcome the fluctuation of peak to peak cogging torque is less than 0.1N between HEMs. Therefore, it is possible to assume that the cogging torque is constant for the analysis.

Table 4.1: open-end generator efficiencies.

Stator core (material, x-direction length)	rotor speed (rpm)	rms power per phase	efficiency
ABS, 100mm	800	12.3W	61.0%
SS400, 10mm	800	11.8W	54.0%
SS400, 100mm	220	11.3W	56.3%

Table 4.2 shows the efficiencies of several open-end generators calculated from FEM analysis data. According to the results, the ABS stator core can achieve better efficiency than soft magnetic steel stator core. The primary reason for efficiency improvement is the absence of eddy currents in ABS core. The relatively low efficiency of all generators is due to using an inefficient pole and slot count. Better pole and slot count are possible if the permanent magnet is custom man-
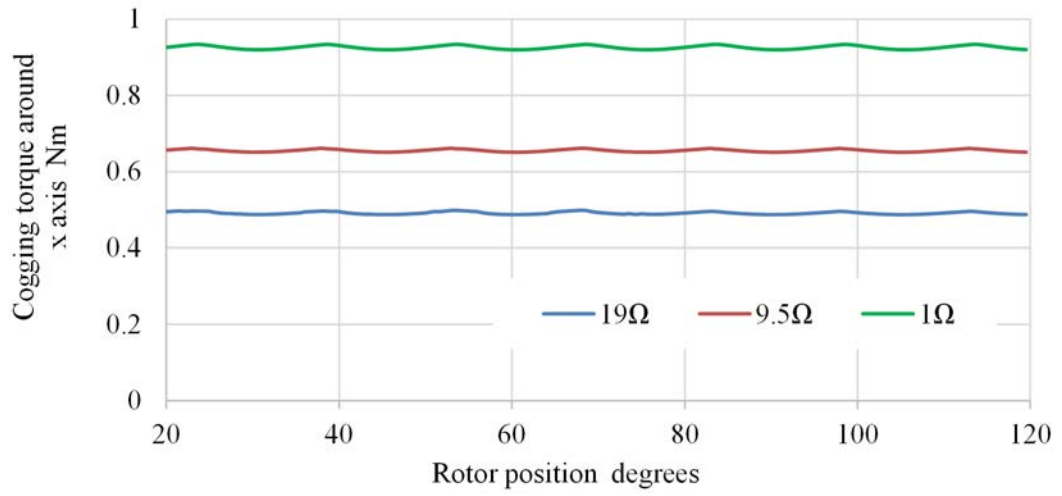
Figure 4.19: Cogging torque around x-axis of the open-end generator design D5 under 19 Ω, 9.5 Ω, and 1 Ω external loads at 800rpm. ABS is used as the core material.

ufactured for the open-end generator. However, the obtained efficiency of 61% is sufficient for an initial prototype.

Chapter 5

Mathematical model of the Levitated platform and the Levitation controller

When the MagLevLS platform is levitated, the levitated platform has six degrees of freedom. The linear sliding motion of the platform in the x-direction is achieved and controlled using a linear motor. The linear motion in the y-direction and the yawing motion around the z-axis are passively controlled by the geometrical design of the HEM and the guide rail. The mathematical model for the MagLevLS platform is obtained for the three degrees of freedom motion of the levitated platform in the linear z-direction, roll around the x-axis, and pitch around the y-axis. Fig. 5.1 shows the coordinate system used for the mathematical modeling and the forces acting on the MagLevLS platform.

5.1   Three degree of freedom Mathematical model of the MagLevLS

Equation 5.1 shows the linearized mathematical model of a HEM around operating point (z_0,i_0) obtained by linearizing Eq. 3.2, where F_n is the attractive force between the nth HEM and the guide rail. The operating point is selected in such a way that the weight of the MagLevLS platform is supported by four HEMs without
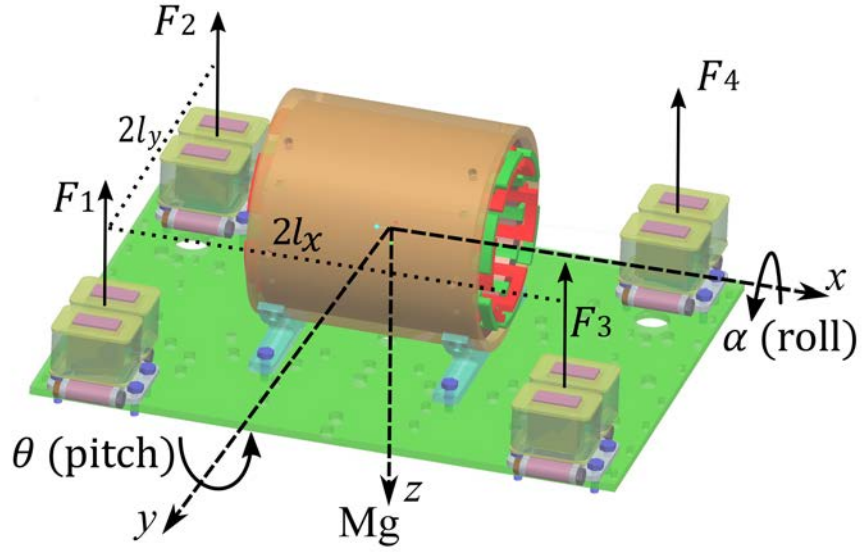
Figure 5.1: Magnetically levitated linear slider platform. Coordinate system, forces and torques acting on the MagLevLS platform

consuming any electric power (i.e. $i_0 = 0$ A).

$$[F_n]_{z_0,i_0} \cong F_n(z_0, i_0) + k_i \delta i_n - k_z \delta z_n \tag{5.1}$$

Where,

$$k_i = \left(\frac{\partial F}{\partial i}\right)_{z_0,i_0} = \frac{2ab}{(z_0 + c)^2}$$

$$k_z = -\left(\frac{\partial F}{\partial z}\right)_{z_0,i_0} = \frac{2ab^2}{(z_0 + c)^3}$$

a $= 1.845\ 1.845 \times 10^{-5}\ \mathrm{Nm^2A^{-2}}$
b $= 4.713$A
c $= 1.3 \times 10^{-3}$m
n $= 1, ..., 4$
$i_0 = 0$ A
$z_0 =$ Levitated air gap in m

The constants a, b, and c were obtained by 3D FEM analysis of the HEM. When the MagLevLS platform with mass M is levitated at air gap of z_0 and coil

current i_0 for all four HEMs, assuming that all four HEMs are identical,

$$\sum_{n=1}^{4} F_n (z_0, i_0) - Mg = 0 \tag{5.2}$$

Then, the linearized equations describing forces acting in the z-direction and torques acting around x and y-axes of the MagLevLS platform around the operating point (z_0, i_0) become,

$$\begin{bmatrix} F_z \\ \Gamma_x \\ \Gamma_y \end{bmatrix} = T \begin{bmatrix} F_1 \\ F_2 \\ F_3 \\ F_4 \end{bmatrix} \tag{5.3}$$

Where,

$$T = \begin{bmatrix} -1 & -1 & -1 & -1 \\ -l_y & l_y & -l_y & l_y \\ -l_x & -l_x & l_x & l_x \end{bmatrix}$$

F_z, Γ_x, and Γ_y are the forces acting on the levitated platform in the z-direction, torque around the x-axis, and torque around the y-axis, respectively.

Considering the geometrical constraints of the levitated platform, we can obtain Eq. 5.4 for small angles $\delta\alpha$ and $\delta\theta$.

$$\begin{bmatrix} \delta z_1 \\ \delta z_2 \\ \delta z_3 \\ \delta z_4 \end{bmatrix} = -T' \begin{bmatrix} \delta z \\ \delta\alpha \\ \delta\theta \end{bmatrix} \tag{5.4}$$

Where,

$\delta z_n = z_n - z_0$

z_n = Air gap between the nth HEM and the guide rail,

δz = A small change of position of the center of gravity of the platform in the z-direction.

From Eq. 5.1 to 5.4, linearized mathematical model as shown in Eq. 5.5 for

44

the MagLevLS platform was obtained.

$$
\begin{bmatrix} M\ddot{z} \\ I_x\ddot{\alpha} \\ I_y\ddot{\theta} \end{bmatrix} = k_z TT' \begin{bmatrix} \delta z \\ \delta\alpha \\ \delta\theta \end{bmatrix} + Tk_i \begin{bmatrix} \delta i_1 \\ \delta i_2 \\ \delta i_3 \\ \delta i_4 \end{bmatrix}
\tag{5.5}
$$

Where,

M $\quad$ = mass of the MagLevLS 5.1kg
I_x $\quad$ = moment of inertia of the MagLevLS around the x-axis $(3.973\times10^{-2}\text{kgm}^2)$
I_y $\quad$ = moment of inertia of the MagLevLS around the y-axis $(5.797\times10^{-2}\text{kgm}^2)$
δi_n = current in the nth HEM $(n=1,..., 4)$.

5.2 Levitation Controller

The state vector of the MagLevLS platform is selected as,

$$
X = \begin{bmatrix} \delta z & \delta\alpha & \delta\theta & \delta\dot{z} & \delta\dot{\alpha} & \delta\dot{\theta} \end{bmatrix}'
\tag{5.6}
$$

The state space realization of the MagLevLS platform is,

$$
\dot{X} = \begin{bmatrix} 0_{3\times3} & I_{3\times3} \\ k_z TT' & 0_{3\times3} \end{bmatrix} X + \begin{bmatrix} 0_{3\times4} \\ Tk_i \end{bmatrix} \begin{bmatrix} \delta i_1 \\ \delta i_2 \\ \delta i_3 \\ \delta i_4 \end{bmatrix}
\tag{5.7}
$$

where, $I_{3\times3}$ is a 3×3 identity matrix and $0_{3\times3}$ and $0_{3\times4}$ are 3×3 and 3×4 zero matrices respectively.

Assuming that the platform levitation is stabilized by applying δF_z force in the z-direction, $\delta\Gamma_x$ torque around the x-axis, and $\delta\Gamma_y$ torque around the y-axis,

platforms state space representation can be obtained as Eq. 5.8:

$$\dot{X} = \begin{bmatrix} 0_{3\times3} & I_{3\times3} \\ k_z TT' & 0_{3\times3} \end{bmatrix} X + \begin{bmatrix} 0_{3\times3} \\ I_{3\times3} \end{bmatrix} \begin{bmatrix} \delta F_z \\ \delta \Gamma_x \\ \delta \Gamma_y \end{bmatrix} \tag{5.8}$$

The state space retaliation of the MagLevLS platform shown in 5.8 is in the form,

$$\dot{X} = AX + BU$$

$$Y = CX + DU$$

where,

$$A = \begin{bmatrix} 0_{3\times3} & I_{3\times3} \\ k_z TT' & 0_{3\times3} \end{bmatrix}$$

$$B = \begin{bmatrix} 0_{3\times3} \\ I_{3\times3} \end{bmatrix}$$

$$C = \begin{bmatrix} I_{3\times3} & 0_{3\times3} \end{bmatrix}$$

$$D = [0_{3\times3}]$$

Then the controllability matrix R becomes (5.9), and observability matrix Q becomes (5.10). The rank of controllability matrix is 6, and the rank of observability matrix is also 6. Since the ranks are equal to the rank of matrix A, the system is state controllable and observable.

$$R = \begin{bmatrix} A & AB & A^2B & ... & A^5B \end{bmatrix} \tag{5.9}$$

$$Q = \begin{bmatrix} C & CA & CA^2 & ... & CA^5 \end{bmatrix} \tag{5.10}$$

The four control currents δi_n (n=1,..., 4) of the four HEMs are obtained by

transforming controlled force δF_z, controlled torque $\delta \Gamma_x$, and controlled torque $\delta \Gamma_y$ as (5.11). The transform matrix $T^{\#}$ is the pseudo inverse of matrix T defined as Eq. 5.12. Equation 5.13 shows expanded form of the Eq. 5.11

$$
\begin{bmatrix} \delta i_1 \\ \delta i_2 \\ \delta i_3 \\ \delta i_4 \end{bmatrix} = \frac{T^{\#}}{k_i} \begin{bmatrix} \delta F_z \\ \delta \Gamma_x \\ \delta \Gamma_y \end{bmatrix} + \frac{k_z}{k_i} (-T') \begin{bmatrix} \delta z \\ \delta \alpha \\ \delta \theta \end{bmatrix} \tag{5.11}
$$

$$
T^{\#}_{4\times3} = \left(\left(\left(T_{3\times4}(T')_{4\times3} \right)^{-1}_{3\times3} \right) T_{3\times4} \right)' \tag{5.12}
$$

$$
\begin{bmatrix} \delta i_1 \\ \delta i_2 \\ \delta i_3 \\ \delta i_4 \end{bmatrix} = \frac{1}{k_i} \begin{bmatrix} -0.25 & -\frac{1}{4l_y} & -\frac{1}{4l_x} \\ -0.25 & +\frac{1}{4l_y} & -\frac{1}{4l_x} \\ -0.25 & -\frac{1}{4l_y} & +\frac{1}{4l_x} \\ -0.25 & +\frac{1}{4l_y} & +\frac{1}{4l_x} \end{bmatrix} \begin{bmatrix} \delta F_z \\ \delta \Gamma_x \\ \delta \Gamma_y \end{bmatrix}
$$

$$
+ \frac{k_z}{k_i} \begin{bmatrix} 1 & +l_y & +l_x \\ 1 & -l_y & +l_x \\ 1 & +l_y & -l_x \\ 1 & -l_y & -l_x \end{bmatrix} \begin{bmatrix} \delta z \\ \delta \alpha \\ \delta \theta \end{bmatrix} \tag{5.13}
$$

Where,

l_x=0.11 m

l_y=0.09 m

By applying numerical values to the state space model, the numerical representation of the plant dynamics in the form of state space model (5.8) was obtained

as follows.

$$
A = \begin{bmatrix}
0 & 0 & 0 & 1 & 0 & 0 \\
0 & 0 & 0 & 0 & 1 & 0 \\
0 & 0 & 0 & 0 & 0 & 1 \\
21520.8 & 0 & 0 & 0 & 0 & 0 \\
0 & 174.3 & 0 & 0 & 0 & 0 \\
0 & 0 & 260.4 & 0 & 0 & 0
\end{bmatrix}
\tag{5.14}
$$

The multiple input multiple output (MIMO) system shown in (5.8) and (5.14) yields continuous linear time invariant input to output relationships as follows,

$$
M\ddot{z} = \frac{1}{s^2 - 21520}\delta Fz
\tag{5.15}
$$

$$
I_x\ddot{\alpha} = \frac{1}{s^2 - 174.3}\delta\Gamma_\alpha
\tag{5.16}
$$

$$
I_y\ddot{\theta} = \frac{1}{s^2 - 260.4}\delta\Gamma_\theta
\tag{5.17}
$$

All other inputs to output relationships are zero. Therefore, force δF_z and torques $\delta\Gamma_x$ and $\delta\Gamma_y$ required for achieving stable levitation around operating point (z_0, i_0) can be controlled using three separate proportional and derivative (PD) controllers controlling each mode of platform. The cogging forces and torques introduced by the open-end generator are considered as disturbances to the MagLevLS system.

5.3   Initial PD controller gains

Discrete time PD controllers having filtered derivative was used to control each mode of the MagLevLS platform. The derivative filtering was used because experimental measurements of air gaps were noisy. The compensation formula for the

discrete time PD controller with derivative filtering was shown in Eq. 5.18.

$$y(z) = \left(k_p + k_d \frac{N}{Nt_s \frac{1}{z-1}} \right) u(z) \tag{5.18}$$

Where,

k_p = Proportional gain

k_d = Derivative gain

N = Derivative filter coefficient

t_s = Sample time (0.001s)

The initial gains for the discrete time PD controllers were obtained to satisfy following criteria in each mode of operation,

- Vertical direction (z)

    - Less than 50% overshoot

    - Less than 0.04s settling time

    - 0.01s rise time

- Roll around x-axis and pitch around y-axis

    - Less than 50% overshoot

    - Less than 1s settling time

    - 0.2s rise time

Each of the three PD controllers was modeled in Simulink as discrete time models having 1kHz sampling rate and PID tuner tool of Matlab was used to obtain initial gains which satisfy above conditions. The obtained gains include k_p proportional gain, k_d derivative gain, and N derivative filter coefficient. The obtained initial discrete time PD controller gains for LTI system models and achieved performance is shown in table 5.1. The figures 5.2, 5.3, and 5.4 shows step tracking response of each mode of operation. The initial controller gains could achieve levitation in nonlinear system simulator within a very small range around linearized system position. However, it was not possible to achieve levitation with initial gains in the experimental system. Therefore, further controller gain tuning was performed using nonlinear system simulator to increase the robustness of the

system. The tuning was done while observing the performance of the nonlinear system simulation when external forces and torques are applied to the platform. When the simulated system can achieve stable levitation, a small external force was applied to the platform and external force was increased in small steps until the system becomes unstable under influence of external input. Then each of the controller gains was changed in small values until nonlinear system simulator can achieve stable levitation while under influence of external forces and the procedure was repeated until sufficient system performance under external load inputs were obtained. Furthermore, the gains obtained were tested so that the system can reach stable levitation position starting from initial condition having an air gap of 5mm for each HEM.

Table 5.1: Initial controller gains and performance

Mode of operation	Controller gains	Performance
Vertical direction (z)	k_{pz}= 66067	Rise time 3ms
	k_{dz}= 264	Settling time 30ms
	N_z = 1882	Overshoot 39.7%
Roll around x-axis	$k_{p\alpha}$= 419	Rise time 62ms
	$k_{d\alpha}$= 13.1	Settling time 549ms
	N_α= 48.5	Overshoot 35.8%
Pitch around y-axis	$k_{p\theta}$ = 621	Rise time 51ms
	$k_{d\theta}$ = 14.6	Settling time 472ms
	N_θ = 50.1	Overshoot 39.6%
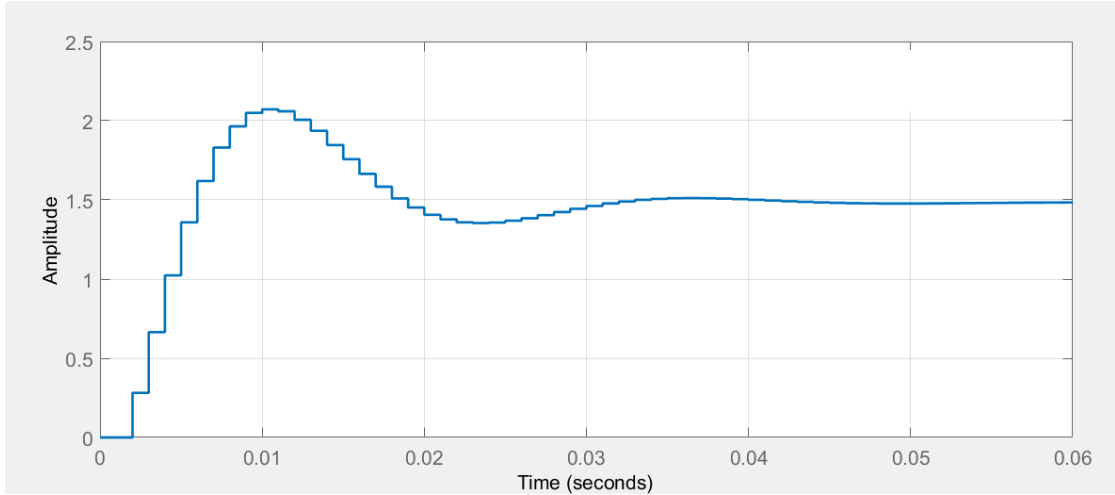
Figure 5.2: Discrete time PD controllers step tracking response for controlling δF_z
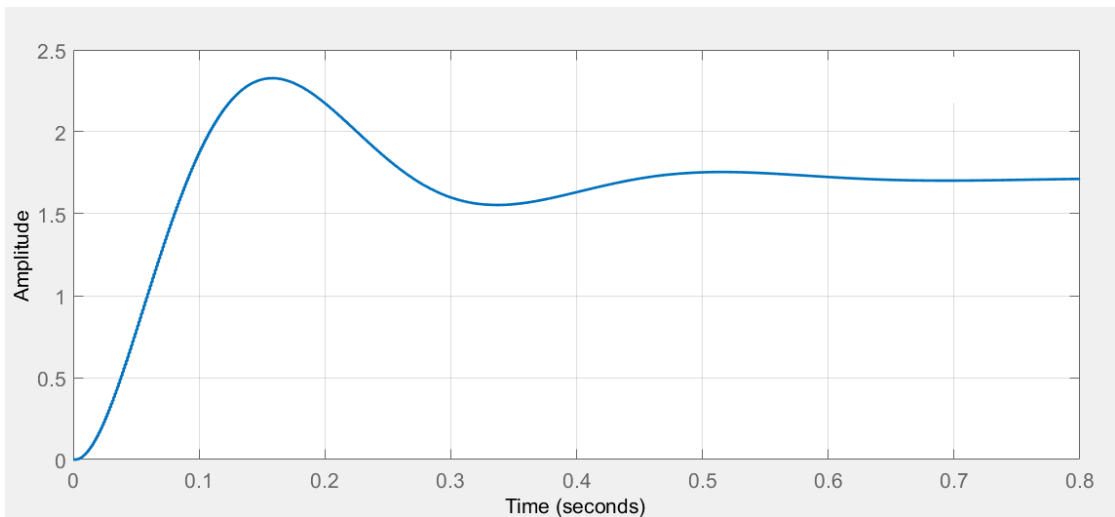
Figure 5.3: Discrete time PD controllers step tracking response for controlling $\delta \Gamma_x$
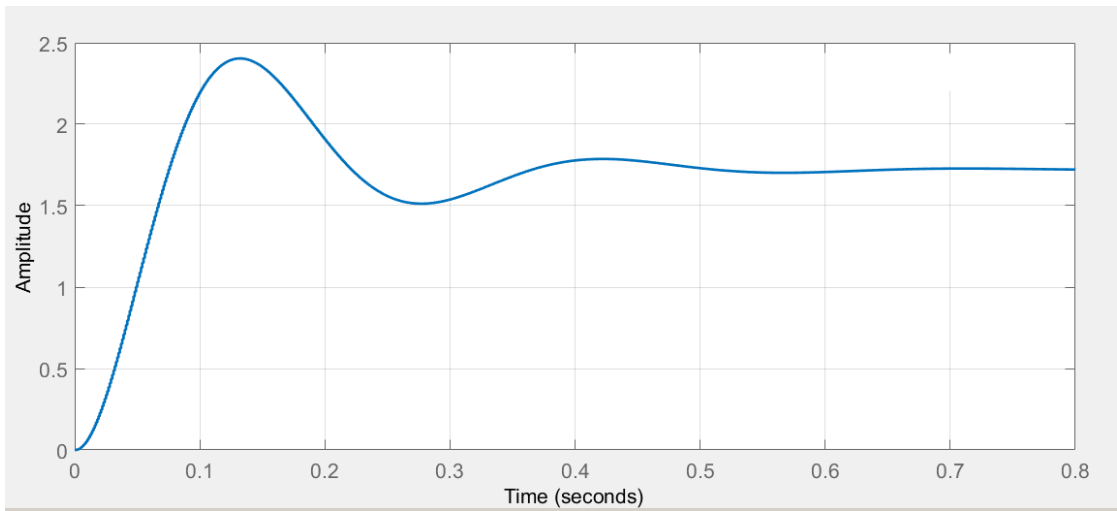
Figure 5.4: Discrete time PD controllers step tracking response for controlling $\delta\Gamma_y$

Chapter 6

Nonlinear system modeling and simulation

Since the system is nonlinear and initial controller gains are not sufficiently accurate to achieve good levitation performance of the experimental system, a nonlinear system was modeled and simulated. The experimental system includes motor drivers for HEMs, laser sensors for air gap measurement and a DSP controller to run control algorithm. The DSP controller has measured input to output delay of 1ms. Furthermore, the current controllers used to drive HEMs has unknown input to output delay and response. Therefore, system identification toolbox was used to estimate input to output relationship of the current driver using measured data. Equation 6.1 shows the discrete time LTI transfer function obtained.

$$i = \frac{0.3973z + 0.1734}{z^2 - 0.4882z + 0.06118} v \tag{6.1}$$

Where,

i = Output current from current driver in Amperes,
v = Input voltage to the current driver in volts.

The experimental system has measurement noise observed from air gap sensors. Therefore, 12th order FIR filter was used to filter air gap measurements. The physics of the MagLevLS platform was modeled using Simscape Multibody. The physical dimensions of the levitated platform were modeled and densities of the materials used for the experimental platform was used. The controller was modeled

in Simulink. Following are the modeled features for the nonlinear simulation. Figure 6.1 shows the model used for nonlinear simulation.

- Three degrees of freedom motion. (Linear z-direction, Roll around x-axis and Pitch around y-axis)

- Four HEMs were models using Eq. 3.2 and used slightly different a, b and c constants to simulate real world system

- Air gap measurement noise was modeled using Gaussian noise generator

- 12th order FIR filters used after air gap measurements

- 1ms DSP controller delay

- Current driver transfer function as shown in Eq. 6.1

- Three discrete time PD controllers with derivative filtering to control each mode of levitation control

- Three integral controllers to achieve zero power operation

- External inputs to model cogging torque of the open-end generator and external force inputs for testing.

- Physical limits of current drivers

True zero power control of the presented levitated platform cannot be achieved without introducing another degree of freedom to the experimental levitated platform because four HEMs are not identical in the experimental system. Therefore, three integrators are used to reach near zero power operating point of the experimental platform under different load conditions. It is assumed that the minimum power for the MagLevLS platform is achieved when $\theta = 0^0$, $\alpha = 0^0$, and z_0 satisfies Eq. 5.2 for the experimental HEMs while platform is not under external forces and torques. Figure 6.2 shows the controller used for the experiment and nonlinear system simulation. The zero power control loop with three integrators are highlighted in red in fig. 6.2. The zero power control loop uses 40th order FIR filter in order to reduce the effect of noise on zero power levitation position adjustment. When there is a coil current in any of HEMs, the zero power control loop generate adjustment signal, which is used to adjust reference position of PD controllers as
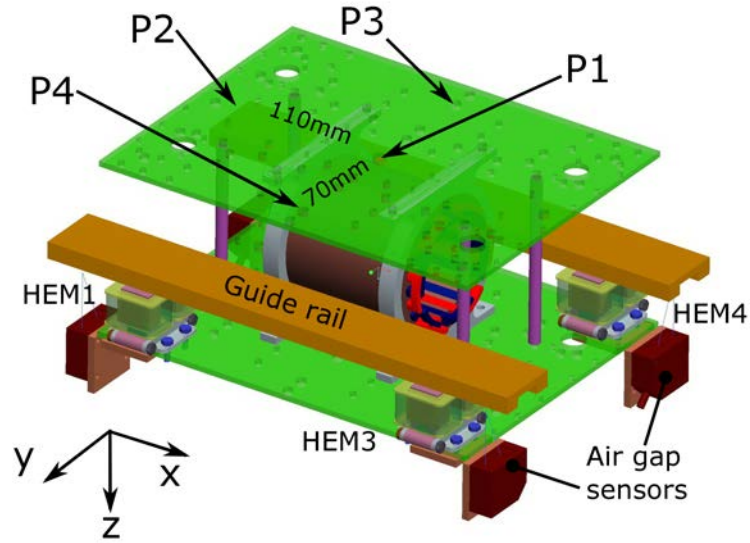
Figure 6.1: Model used for the nonlinear system simulation

shown in fig 6.2. This can be explained as a dynamic reference adjustment of PD controllers based on coil currents to reach zero coil current levitation position. Each of the three integral controllers shown in fig. 6.2 has saturation limits as shown in table 6.1. Initial values of the integral gains were selected as 0.00001 and later adjusted in small increments until the system can reach zero power levitation position within approximately 1s time when an external force or torque applied. Figure 6.3 shows the nonlinear simulator.

Four simulations were performed to observe controller performance as follows, (the point P1 and P2 are shown in fig. 6.1)

1. A external force input was applied to the top plate of the platform at point P1 in z-direction while cogging torque was not applied.

2. A external force input was applied to the top plate of the platform at point P1 in z-direction while cogging torque was applied.

3. A external force input was applied to the point P2 of the platform in z-direction while cogging torque was not applied

4. A external force input was applied to the point P2 of the platform in z-direction while cogging torque was applied
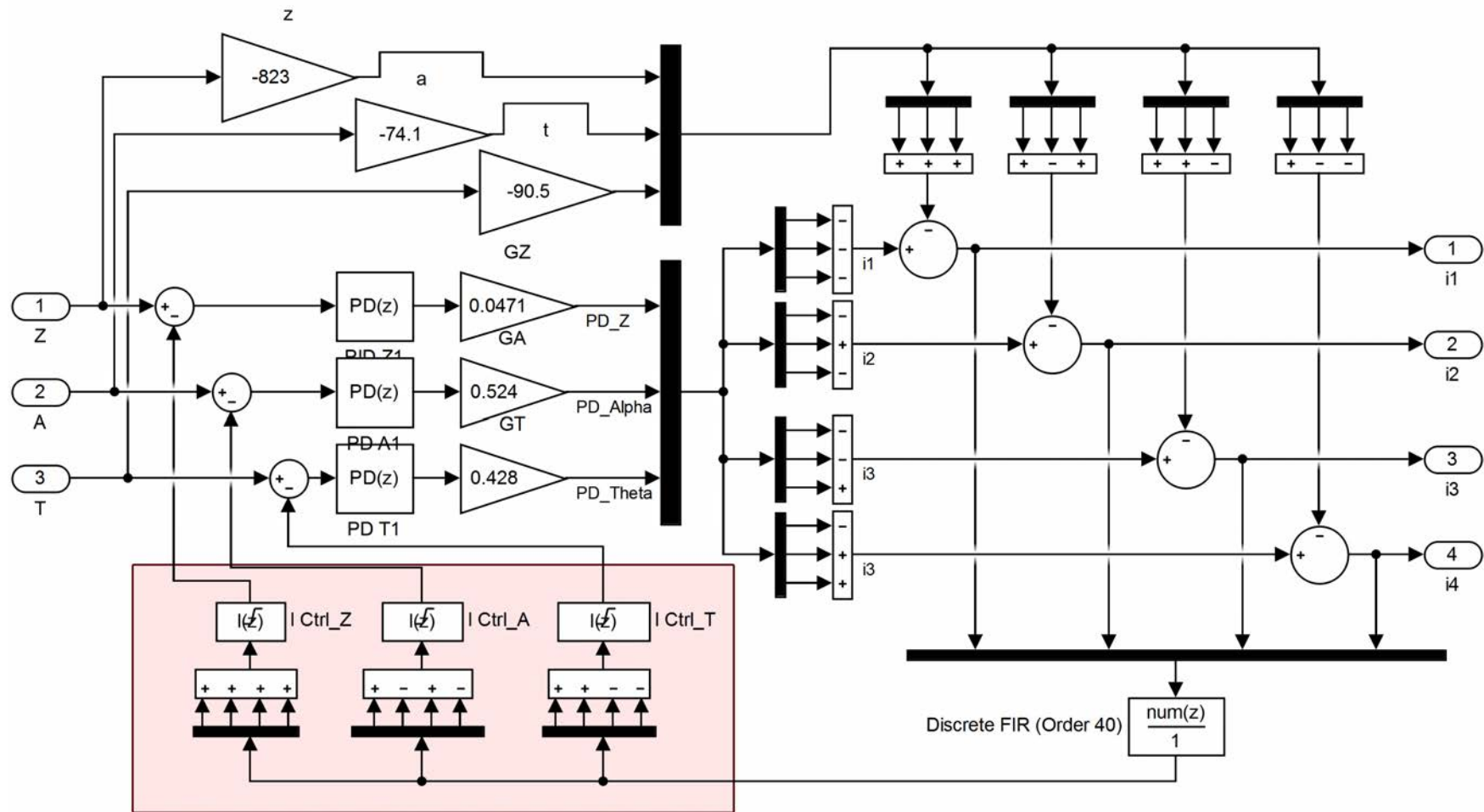
Figure 6.2: Complete controller used for the experiment and nonlinear simulation
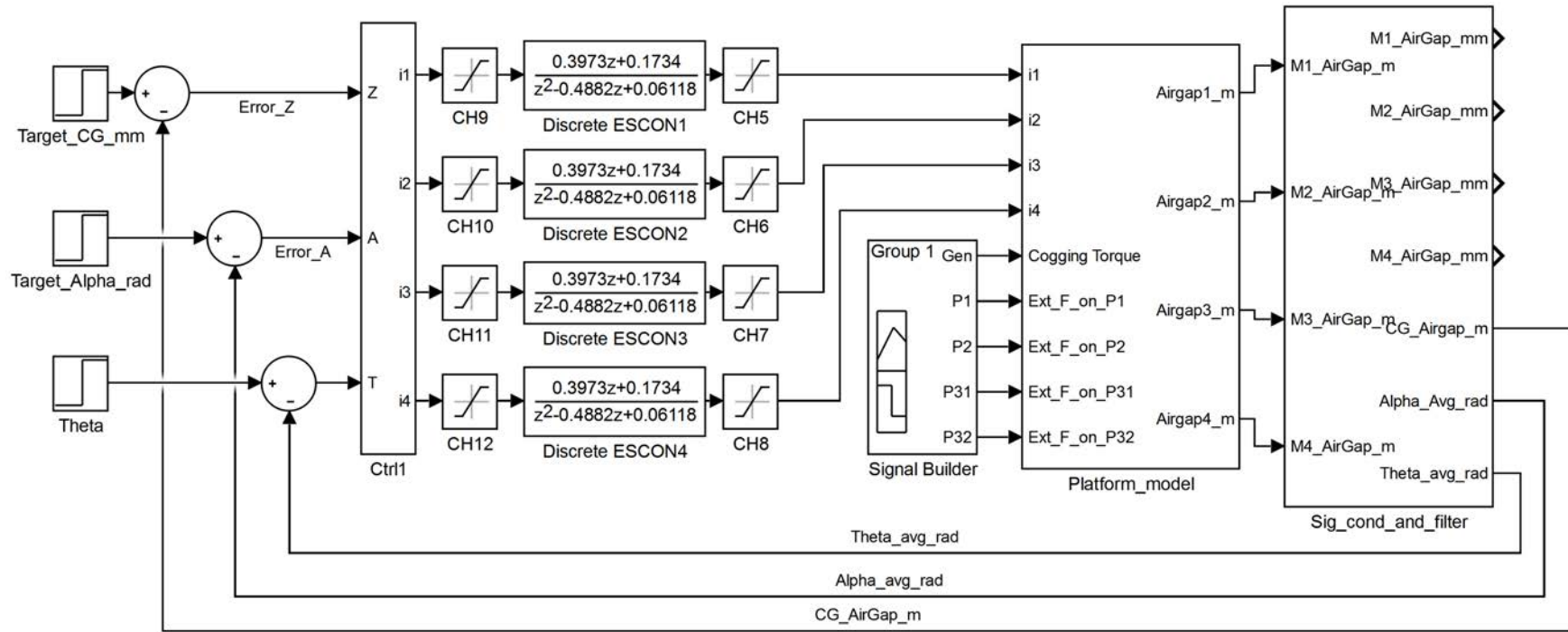
Figure 6.3: Nonlinear 3DOF MagLevLS system simulator

The simulation one and simulation two represents a load applied at the center of the platform at point P1. In real life operation, it is not possible to guarantee that the load will be applied at the center of the platform. Therefore, simulations were performed to observe the behavior of the platform when a load was applied at point P2. Point P2 is defined as the point on the MagLevLS platform where the xz plane and a straight line connecting F_1 and F_2 cross each other on the top platform as shown in fig. 6.1.

The results presented in this chapter was obtained by simulations performed using controller gains shown in table 6.1. The gains given in table 6.1 were obtained by starting from gains shown in table 5.1. The initial gains shown in table 5.1 were modified in small values until expected system performance was achieved.

Table 6.1: Controller gains used for simulations and experiments.

Mode of operation	Controller gains	Saturation limit
Vertical direction (z), PD controller	k_{pz}= 42100 k_{dz}= 510 N_z = 1854	
Roll around x-axis, PD controller	$k_{p\alpha}$= 340 $k_{d\alpha}$= 4.25 N_α = 1754	
Pitch around y-axis, PD controller	$k_{p\theta}$= 484 $k_{d\theta}$= 6.9 N_θ = 1745	
Vertical direction (z), Zero power integrator	k_{Iz}= 0.0011	±2mm
Roll around x-axis, Zero power integrator	$k_{I\alpha}$= 0.011	±0.02rad
Pitch around y-axis, Zero power integrator	$k_{I\theta}$= 0.012	±0.02rad

There are several differences in simulation compared to the experiment. The first major difference is the mathematical equation used to model HEM. The experimental results shown in fig. 7.4 suggest that the mathematical model produces

larger forces compared to the experimental prototype. The difference can be attributed to non-homogeneous nature of materials of the experimental prototype, Non-uniform coil winding, and tolerance in experimental components. In the simulation, external forces were applied without adding any additional mass onto the levitated platform. However, experiments performed by adding a mass onto the platform. Adding a mass changes inertia and total levitated mass of the platform, which is not considered in the simulation. Furthermore, in simulation, a perfectly vertical forces can be applied at perfect locations. But in the experiment, applied load causes impact load and the applied load is not perfectly vertical. This introduces extra forces in the experimental system.

6.1 Simulation 1: Load applied at the center (Point P1) of the platform while open-end generator is stopped.

The first simulation was performed without applying the cogging torque of the open-end generator and with the simulated sensor noise. A external force input of 10.78N was applied to point P1 of the platform in z-direction at time t=3s. The 10.78N force was selected to approximately simulate the weight of the applied mass in the experimental system to obtain the system response. Figure 6.4 shows the currents observed before and after applying external load. The simulation shows that the currents of the all four HEMs reach near zero value within 0.5s from external force input due to the zero power control loop. The rapid fluctuations (at 1000Hz) of the currents are due to the PD controller's response to sensor noise.

Figure 6.5 shows the measured air gaps of the four HEMs when the cogging torque due to the operation of the open-end generator was not applied. Four different steady state levitation air gaps are clearly visible in fig. 6.5 due to the use of four different a, b, and c constants for HEM's force model shown in Eq. 3.2. When the external force input of 10.78N was applied at time t=3s, the MagLevLS platform reaches new zero power levitation air gap within 0.5s as shown in fig. 6.5. Furthermore, since the force is added on to the platform, air gap was reduced as shown.

Figure 6.6 shows the state variables of the MagLevLS platform when a 10.78N external force input applied at the point P1 of the platform in z-direction while

Figure 6.4: Response of the MagLevLS platform when a 10.78N external force applied at the point P1 of the platform in z-direction while cogging torque due to the open-end generator was not applied. Figure shows the measured currents of four HEMs.

Figure 6.5: Response of the MagLevLS platform when a 10.78N external force input applied at the point P1 of the platform in z-direction while cogging torque due to the open-end generator was not applied. Figure shows the measured air gaps of four HEMs (The graph shows air gap measurement after filtering through a 12th order FIR filter)

cogging torque due to the open-end generator was not applied. The simulation result clearly shows that the platform reaches new zero power levitation position after applying extra force on the platform. Furthermore, the simulation results show that state variables α and θ are not affected due to the external force input applied in z-direction at the point P1 of the platform. The state variables α and θ are not zero because of the non-identical HEMs were used for the simulation.

Figure 6.6: Response of the MagLevLS platform when a 10.78N external force input applied at the point P1 of the platform in z-direction while cogging torque due to the open-end generator was not applied. Figure shows the state variables of the MagLevLS platform. (State variables were calculated after filtering air gap measurements through a 12th order FIR filter)

6.2 Simulation 2: Load applied at the center (Point P1) of the platform while open-end generator is running.

The second simulation was performed to observe the performance of the controller under external disturbance of the open-end generator's cogging torque. A constant cogging torque of 0.5Nm was applied around the x-axis of the platform to simulate an open-end generator generating 35W of RMS electrical power. The external force input of 10.78N was applied to the point P1 of the platform in the z-direction and the effect was recorded.

Figure 6.7 shows the measured currents of the four HEMs observed after applying the external force input. According to the simulation results, the currents of all four HEMs reached a near zero value within 0.5s while the platform is under the influence of the cogging torque.

Figure 6.7: Response of the MagLevLS platform when a 10.78N external force input applied at the point P1 of the platform in z-direction while cogging torque due to the open-end generator was applied. Figure shows the measured currents of four HEMs.

Figure 6.8 shows the air gaps measured after applying external force input. The simulation results show that the air gaps of HEM 2 and HEM 4 are higher than the air gaps of HEM 1 and HEM 3 before and after the external force input. In order to overcome cogging torque applied by the open-end generator, the HEMs must generate an opposite torque. Therefore, the HEM 2 and HEM 4 must generate higher forces than HEM 1 and HEM 3 to generate required torque. Furthermore, the zero power control loop must maintain near zero currents in all for HEMs. Therefore, the only possible way to achieve both conditions is to reach levitation air gaps as shown in fig. 6.8.

Figure 6.9 shows the state variables observed after applying external force input at time t=3s. The state variable θ is not affected by the external force input and remained near zero. However, the state variable α was changed due to the external force input as shown in fig. 6.9. The external force reduced the levitation air gap of the platform and can be observed from state variable z. According to the Eq. 3.2 the attractive force generated by a HEM increases with the decreasing air gap. Therefore, the change in air gaps needed to achieve required force difference to
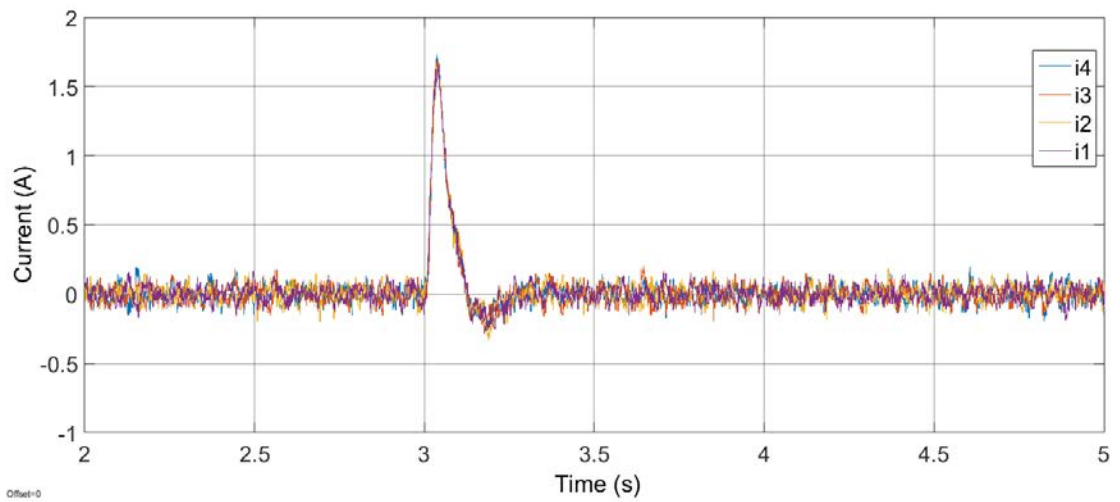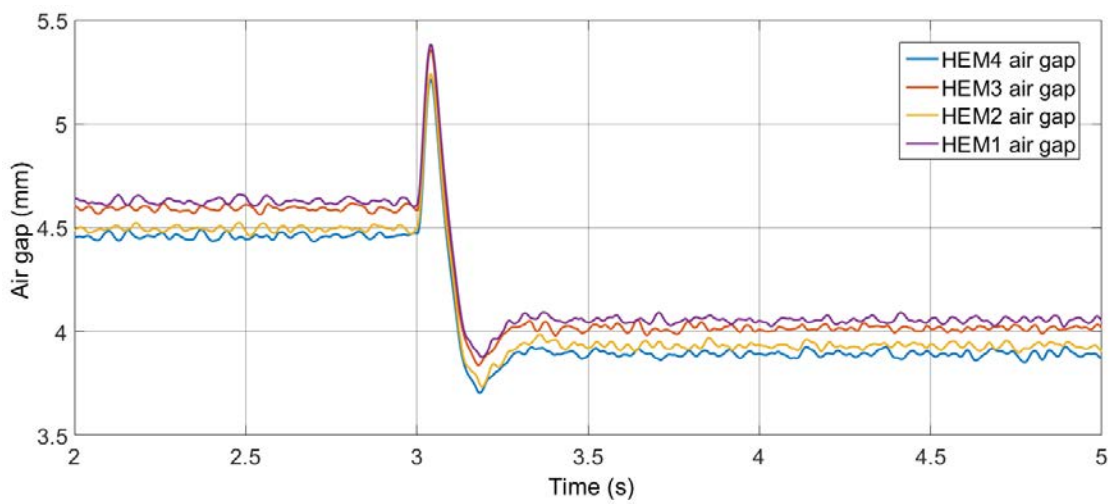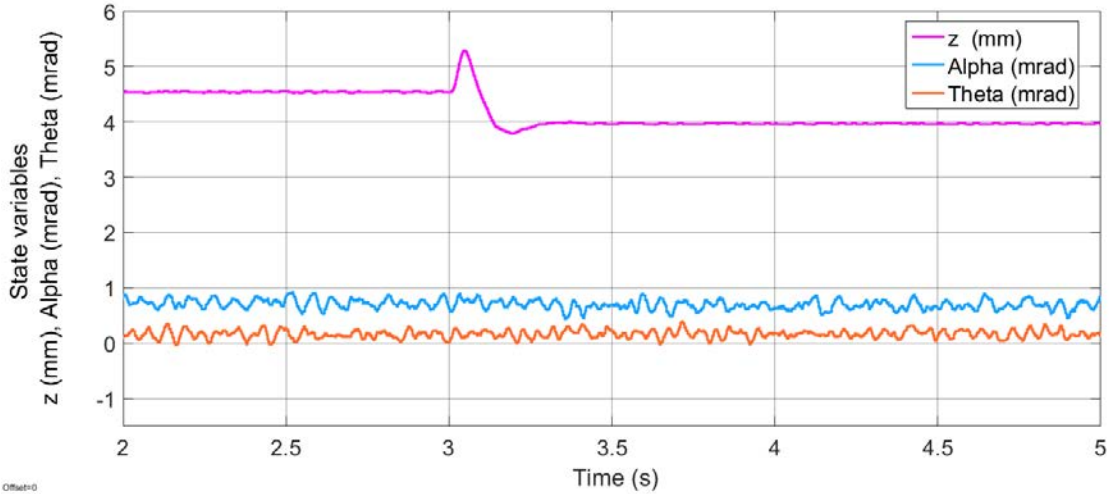
Figure 6.8: Response of the MagLevLS platform when a 10.78N external force input applied at the point P1 of the platform in z-direction while cogging torque due to the open-end generator was applied. Figure shows the measured air gaps of the four HEMs (The graph shows air gap measurement after filtering through a 12th order FIR filter)

overcome the cogging torque reduces at new zero power levitation air gap. (i.e. HEM 2 and HEM 4 must always have higher air gaps than HEM 1 and HEM 3 to overcome cogging torque. However, the difference of the air gaps reduces with decreasing air gap.) Hence, the platform reaches zero power levitation air gap with a reduced value for state variable α as shown in fig. 6.9.

6.3 Simulation 3: Non-Centered external load (at point P2) while open-end generator is stopped.

The third simulation was performed by applying a load of 10.78N at point P2 while the cogging torque of the open-end generator was not applied. Figure 6.10 shows the coil currents observed from four HEMs when the external force input was applied at time t=3s. According to the simulation, the currents of all for HEMs reach near zero values within 0.5s of external force input. Figure 6.11 shows the air gaps observed during the same simulation. Since the load was applied to a non-centered location P2, the HEM 1 and HEM 2 air gaps are higher than that of HEM 3 and HEM 4 after the external force input. Therefore, the platform
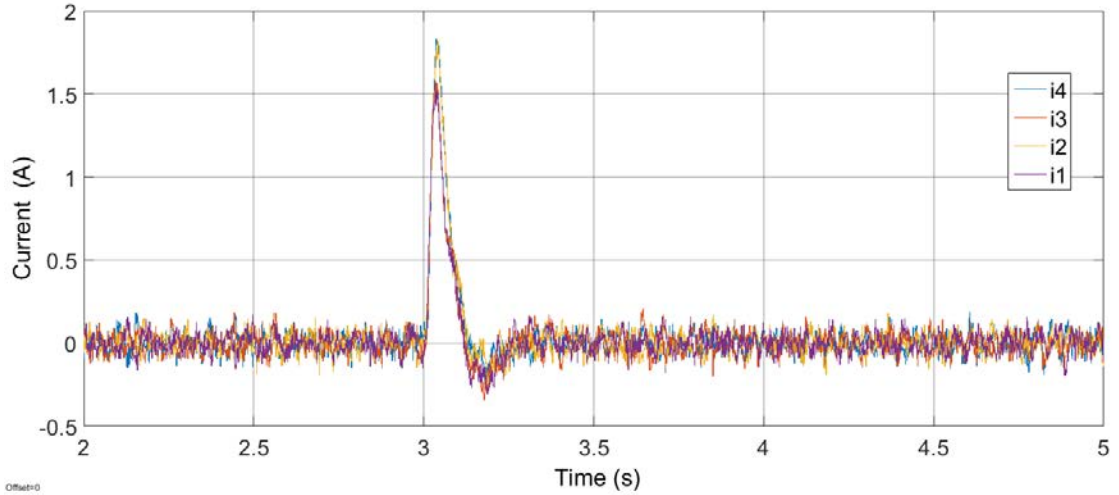
Figure 6.9: Response of the MagLevLS platform when a 10.78N external force input applied at the point P1 of the platform in z-direction while cogging torque due to the open-end generator was applied. Figure shows state variables of the MagLevLS platform. State variables were calculated after filtering measured air gaps using 12th order FIR filter.

is slightly turned around y-axis to reach near zero coil currents for all for HEMs while maintaining stable levitation. Figure 6.12 shows the state variables observed during simulation. The state variable θ clearly shows the effect of applying external force input at non-centered location P2. The state variable θ takes about 0.7s to reach steady state value.

6.4 Simulation 4: Non-Centered load (at point P2) while open-end generator is running.

Nonlinear system simulation 4 was performed by applying 10.78N force at point P2 of the platform in z-direction while the cogging torque of the open-end generator was applied around the x-axis. This simulation considers a situation of applying a non-centered load onto the platform while the open-end generator is generating electric power.

Figure 6.13 shows the currents of the HEMs observed during the simulation. The results show that the current waveform takes more time to reach steady state values compared to previous simulations. However, the simulation shows all four HEMs reaching steady state current near value zero due to the zero power control

64
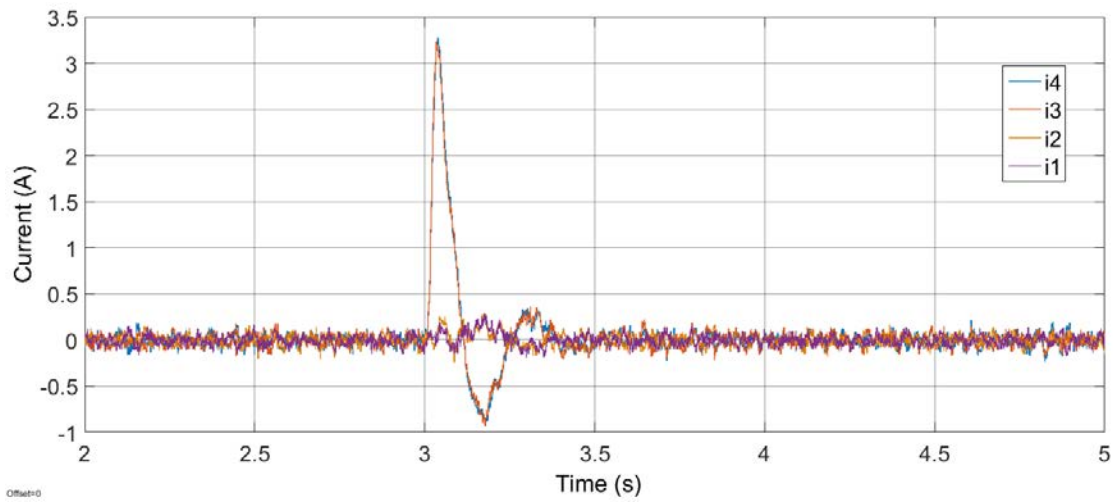
Figure 6.10: Response of the MagLevLS platform when a 10.78N external force input applied at the point P2 of the platform in z-direction while cogging torque due to the open-end generator was not applied. Figure shows the measured currents of four HEMs.
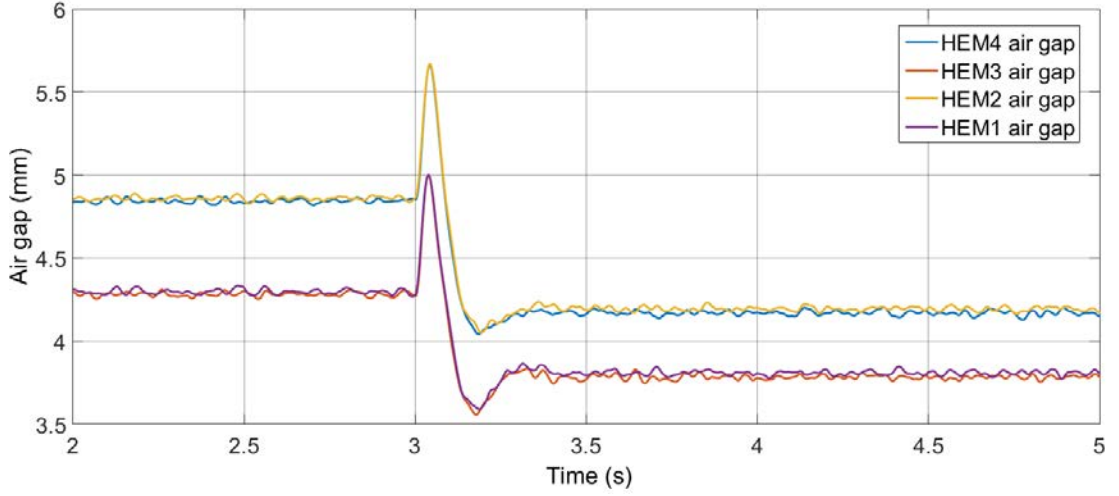

Figure 6.11: Response of the MagLevLS platform when a 10.78N external force input applied at the point P2 of the platform in z-direction while cogging torque due to the open-end generator was not applied. Figure shows the measured air gaps of the four HEMs (The graph shows air gap measurement after filtering through a 12th order FIR filter)

Figure 6.12: Response of the MagLevLS platform when a 10.78N external force input applied at the point P2 of the platform in z-direction while cogging torque due to the open-end generator was not applied. Figure shows state variables of the MagLevLS platform. State variables were calculated after filtering measured air gaps using 12th order FIR filter.

scheme.

Figure 6.14 shows the air gaps observed during the simulation. HEM 1 and HEM 2 air gaps are higher than air gaps of HEM 3 and HEM 4 due to the non-centered load. Furthermore, due to the effect of cogging torque, four HEMs reach four different zero power levitation air gaps as shown in fig. 6.14. This result suggests non-zero values for state variables θ and α.

Figure 6.15 shows the state variables observed during the simulation. Due to the application of external load, platform moved to a new zero power levitation air gap as seen in state variable z of fig. 6.15. The non-zero value of the state variable α before the external force input at time t=3s shows the effect of cogging torque on the platform. After the external force input was applied, the state variable α reaches new reduced value and can be observed in fig. 6.15. This is the expected behavior because the controller reduces air gaps of HEMs to achieve new zero power levitation position due to the application of external load. The state variable θ shows the effect of non-centered load application at point P2. Before application of the load, the state variable θ has value zero. But after the external force input, the state variable θ reaches a new value as shown in fig. 6.15. The new value of state variable θ represents the different efforts done by the HEMs to keep platform levitated while achieving near zero coil currents. Furthermore, the
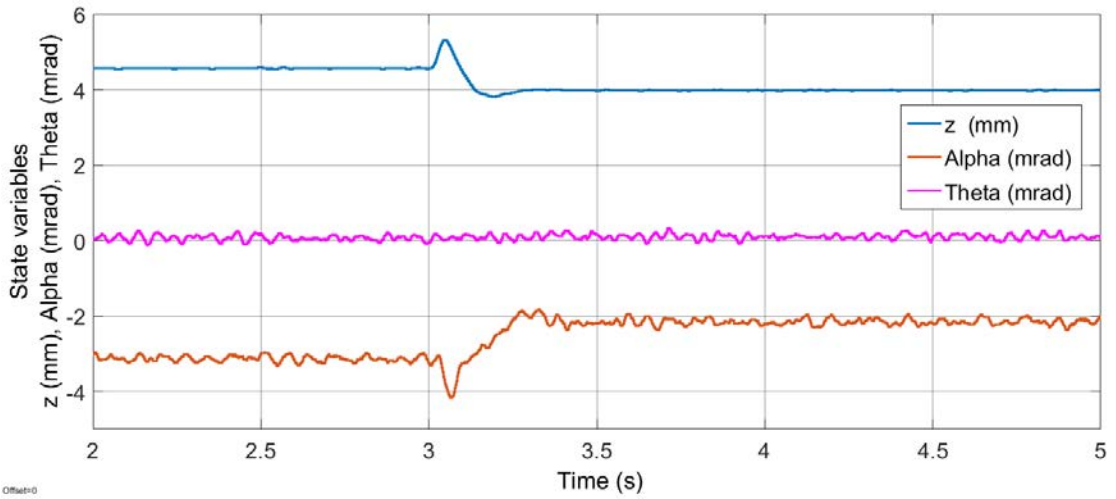
66
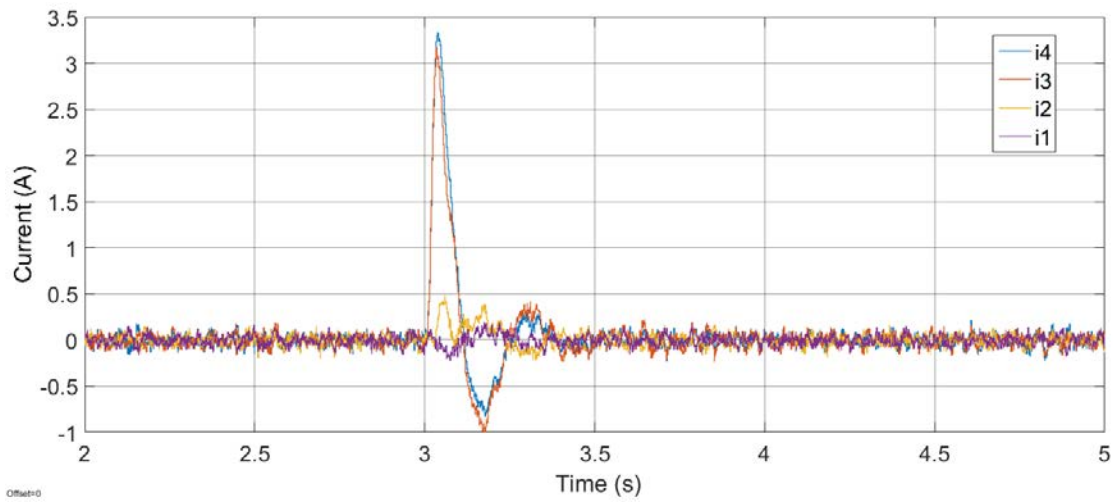
Figure 6.13: Response of the MagLevLS platform when a 10.78N external force input applied at the point P2 of the platform in z-direction while cogging torque due to the open-end generator was applied. Figure shows the measured currents of four HEMs.
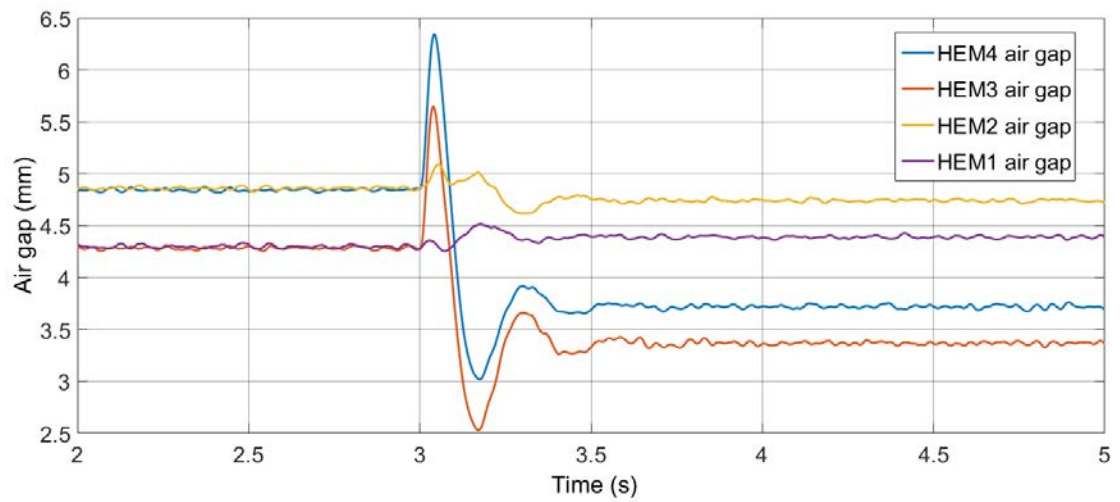
Figure 6.14: Response of the MagLevLS platform when a 10.78N external force input applied at the point P2 of the platform in z-direction while cogging torque due to the open-end generator was applied. Figure shows the measured air gaps of the four HEMs (The graph shows air gap measurement after filtering through a 12th order FIR filter)

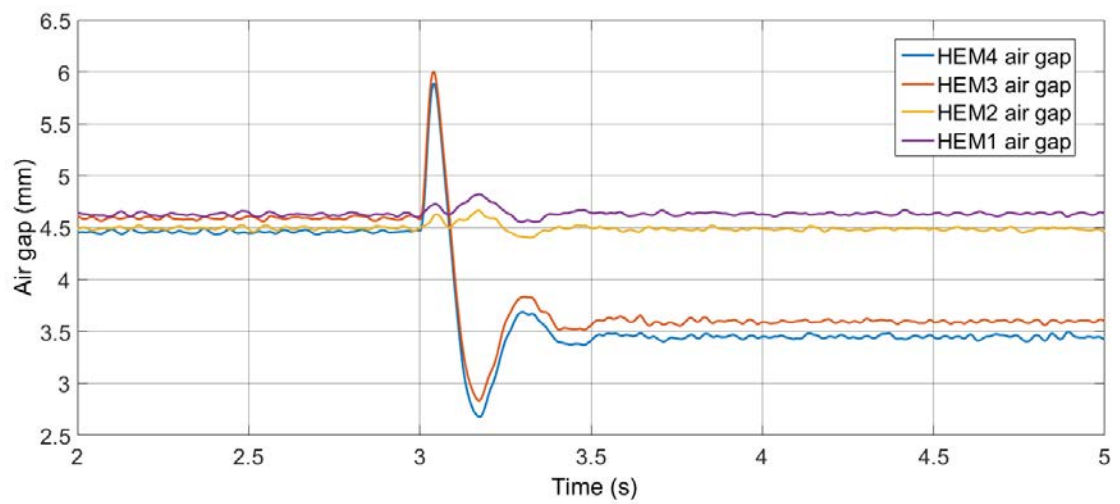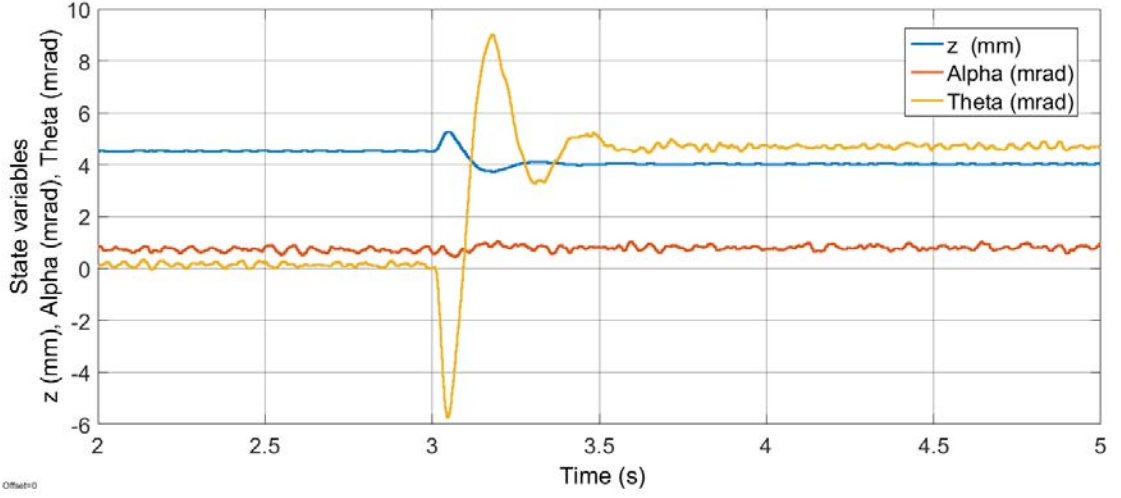time taken to reach steady state value of state variable θ is approximately 0.7s as shown.
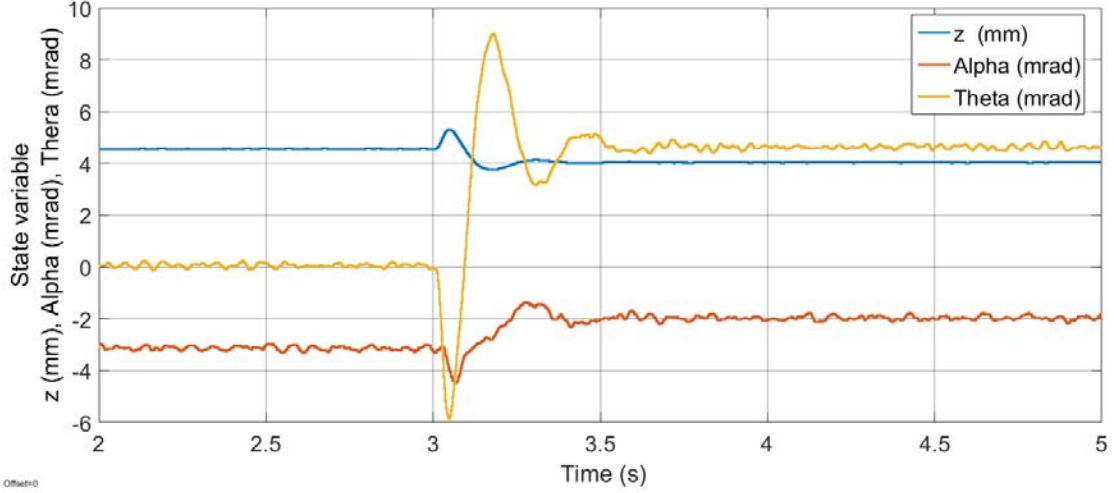
Figure 6.15: Response of the MagLevLS platform when a 10.78N external force input applied at the point P2 of the platform in z-direction while cogging torque due to the open-end generator was applied. Figure shows state variables of the MagLevLS platform. State variables were calculated after filtering measured air gaps using 12th order FIR filter.

6.5 Comparison of observed variables under different simulation conditions

The state variables were compared to identify response differences in each of the four simulations. The simulations were performed without simulating sensor noise to highlight differences in each simulation clearly. The legends of figures 6.16,6.17, and 6.18 use following key,

- OFF: Open-end generator is turned OFF.

- ON: Open-end generator is turned ON

- P1: 10.78N external load applied at point P1 (refer fig. 6.1)

- P2: 10.78N external load applied at point P2 (refer fig. 6.1)

Figure 6.16 shows state variable z observed in four different simulations. According to the comparison results, the value of state variable z is slightly different

before the external force input based on the operational condition of the open-end generator. When the open-end generator is operating, the state variable z has a value 0.03mm higher before the external force input. When the external force input is applied at point P2, the time taken to reach steady state is increased as shown in fig. 6.16. However, there is no significant difference in controller performance due to the cogging torque of the open-end generator in state variable z.

Figure 6.16: State variable z comparison between several simulations. (ON: Open-end generator ON, OFF: Open-end generator OFF, P1 and P2: Location of applied force as shown in fig. 6.1)

Figure 6.17 shows the state variable α observed in four different simulations. Simulations suggest that the state variable α is affected due to the operation of open-end generator. The time taken to reach steady state was largest when the external load was applied at point P2 while open-end generator was operating. However, the MagLevLS platform managed to reach steady state within 1s of external force input in all simulations. Therefore, the controller gains used are suitable to experiment with the experimental system. Furthermore, application of additional force on the levitated platform changed the value of state variable α as shown. When the external load was applied, the levitated platform reached a new zero power levitation air gap, which is smaller than the air gap before application of the external load. When the air gap is reduced, the amount of air gap difference required between HEMs to overcome cogging torque is reduced because lower air gaps of HEMs produce higher forces.

69
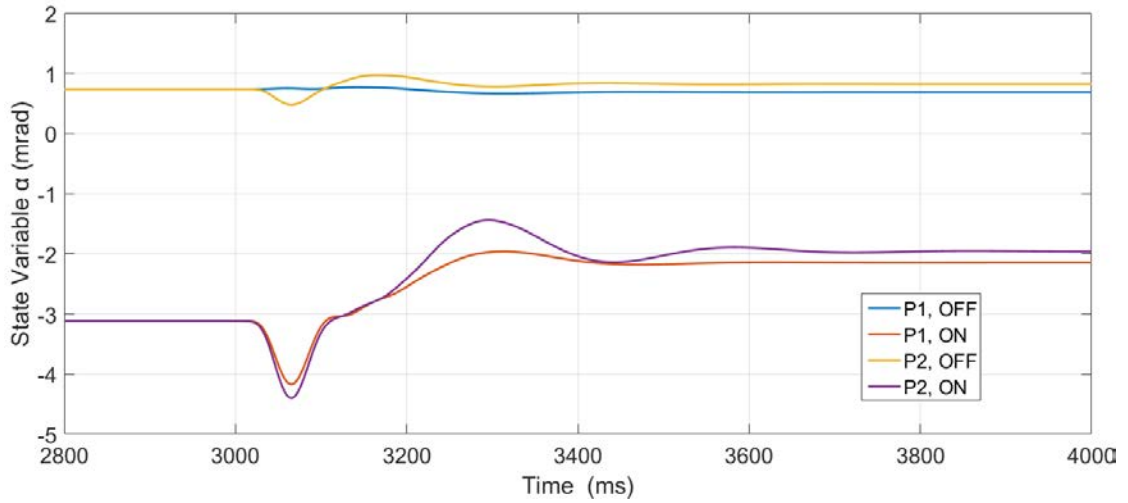
Figure 6.17: State variable α comparison between several simulations. (ON: Open-end generator ON, OFF: Open-end generator OFF, P1 and P2: Location of applied force as shown in fig. 6.1)

Figure 6.18 shows the state variable θ observed in four different simulations. Simulations suggest that the state variable θ is not affected by the open-end generator, but affected by the position of application of external load. When the external load is applied at point P2, the state variable was affected and reaches new steady state value within 1s as shown in fig. 6.18

Figure 6.19 shows the comparison between currents of four HEMs observed during simulations. When the external load was applied at point P2, the HEM 1 and HEM 2 responded with higher currents as shown. All four HEMs reached zero power levitation state within 1s of external force input during all simulations.

Figure 6.20 shows the comparison between air gaps of four HEMs observed during simulations. Simulations show that the air gaps before the external force input depends on the operational condition of the open-end generator. After the external force input, air gaps of four HEMs reach zero power levitation position within 1s of external force input as shown.

Figure 6.21 shows the non linear system simulation when the external forces are applied at point P1, P2, P3 and P4. Locations of applied forces are shown in fig. 6.1.

70
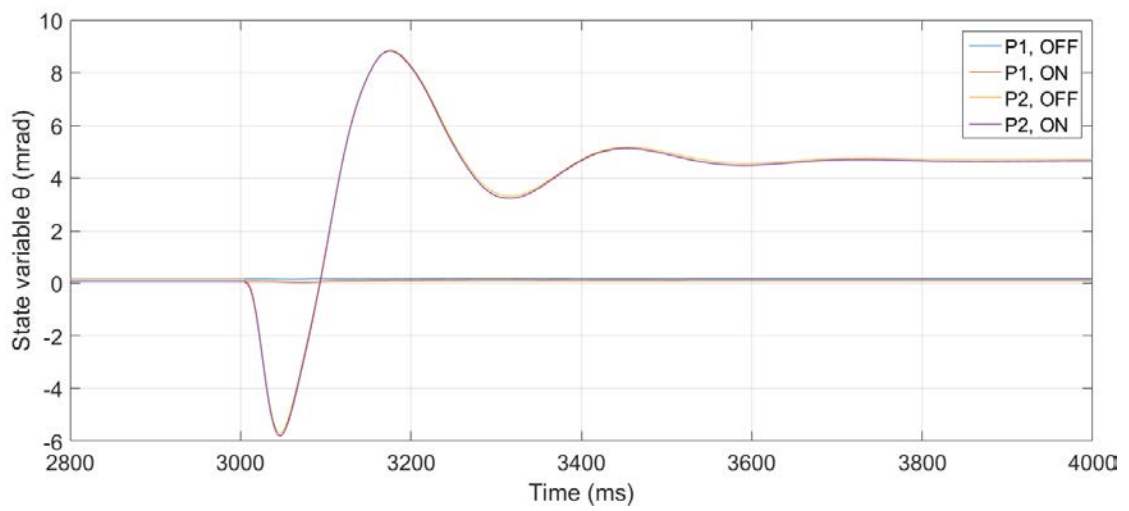
Figure 6.18: State variable θ comparison between several simulations. (ON: Open-end generator ON, OFF: Open-end generator OFF, P1 and P2: Location of applied force as shown in fig. 6.1)
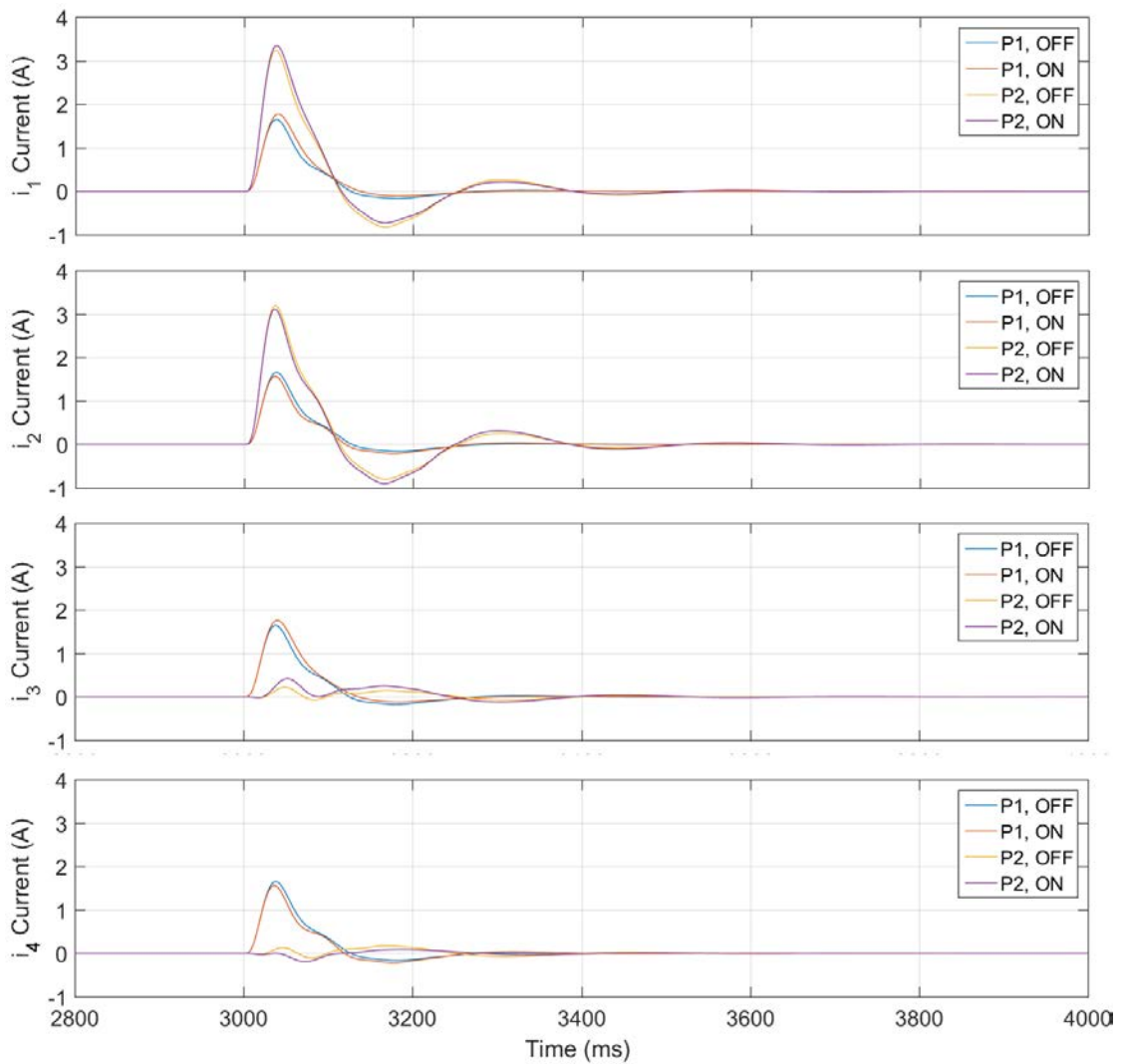
Figure 6.19: Current comparison between several simulations. (ON: Open-end generator ON, OFF: Open-end generator OFF, P1 and P2: Location of applied force as shown in fig. 6.1)
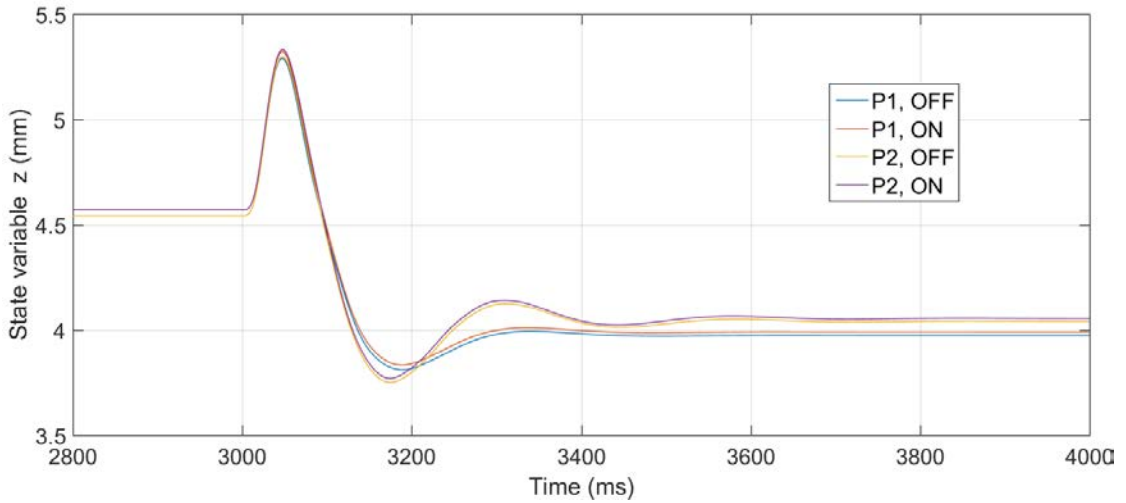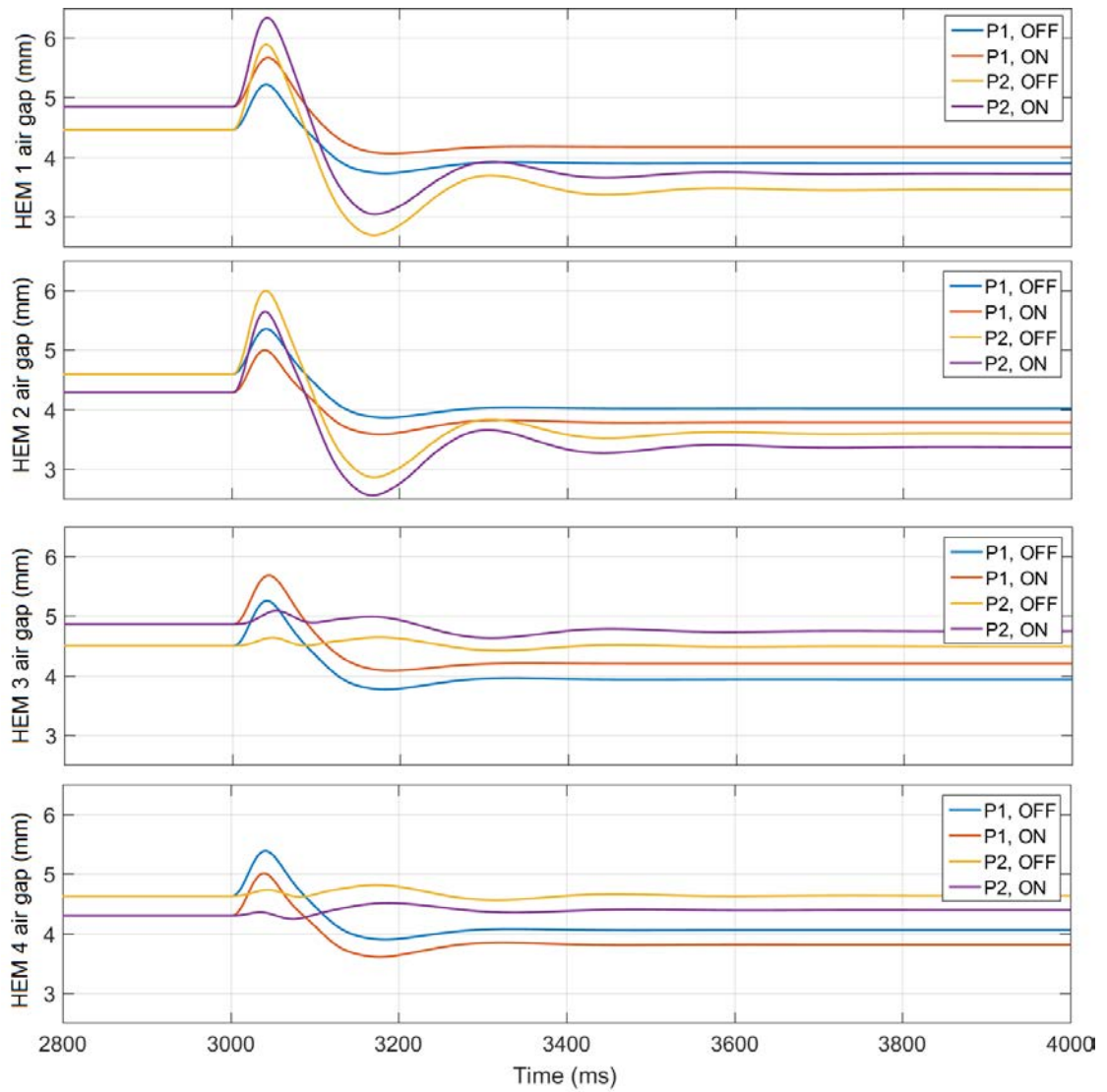
Figure 6.20: Air gaps comparison between several simulations. (ON: Open-end generator ON, OFF: Open-end generator OFF, P1 and P2: Location of applied force as shown in fig. 6.1)
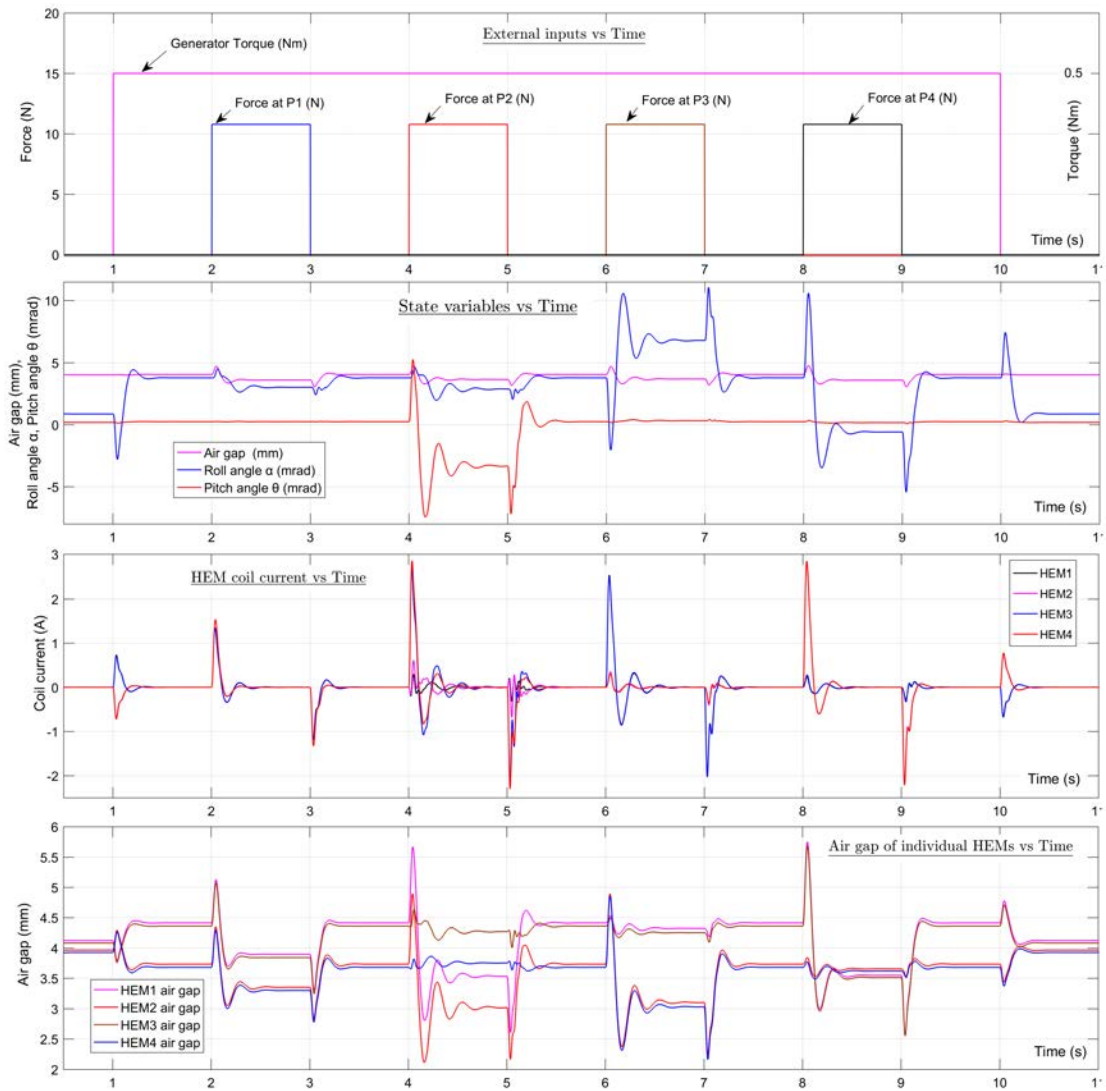
Figure 6.21: System response (simulation) to external inputs. (Locations of applied force as shown in fig. 6.1)

Chapter 7

Prototype system and experimental results

Several experiments were carried out to investigate the function of the major parts of the system using prototype components and experimental prototype of the MagLevLS system. The experiments include,

1. Attractive force, air gap and current measurements to experimentally evaluate a prototype HEM

2. MagLevLS platform 3DOF levitation response by applying a mass at point P1 of fig. 6.1, while the open-end generator is not producing electrical power

3. MagLevLS platform 3DOF levitation response by applying a mass at point P1 of fig. 6.1, while the open-end generator is producing electrical power

4. MagLevLS platform 3DOF levitation response by applying a mass at point P2 of fig. 6.1, while the open-end generator is not producing electrical power

5. MagLevLS platform 3DOF levitation response by applying a mass at point P2 of fig. 6.1, while the open-end generator is producing electrical power

6. open-end generator evaluation to measure electrical power generation

7.1 Experiments with a prototype hybrid electromagnet

A prototype hybrid electromagnet and a guide rail were fabricated and tested to obtain the relationship between the air gap, coil current, and the attractive force. Figure 7.1 shows a prototype HEM manufactured for the experiment. A test bench was designed to measure the attractive force and air gap between the HEM and the guide rail. The test bench is shown in fig. 7.2. The expected forces from the HEM were in the range of 500N when the air gap is in the range of 0.1mm, and when the air gap is in the range of 5mm, the expected force is in the range of 10N according to the FEM analysis. The requirement of measuring large and small forces using same load sensor decreases measurement accuracy. A 500N OIML Class III approved load cell was used for the force experiments. The OIML Class III is accurate up to 3000 force measurement divisions from full capacity. Therefore, the best possible resolution for force measurement is 0.17N when a 500N load cell is used. According to the OIML Class III standard, the minimum force measured from an approved load cell is 30 load measurement divisions. Therefore, the minimum measurable force is 5N satisfying OIML Class III specifications when a 500N load cell is used. Therefore, these specifications satisfy force measurement requirements of HEM using 500N load cell.
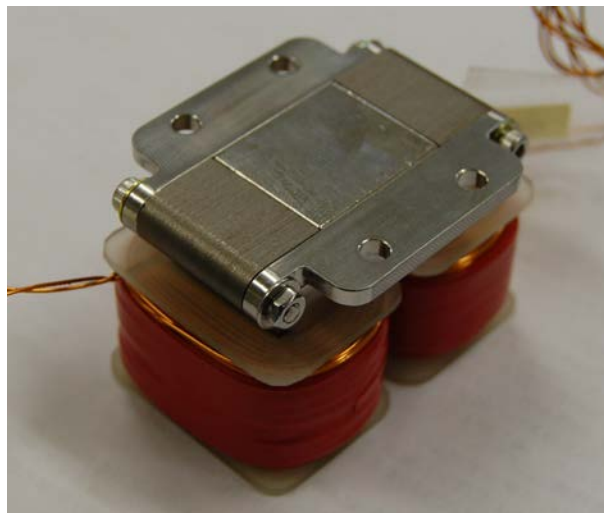
Figure 7.1: A prototype hybrid electromagnet

The air gap was adjusted using a micrometer screw gauge shown in fig. 7.2. Initial air gap measures were taken by directly reading the micrometer gauge.
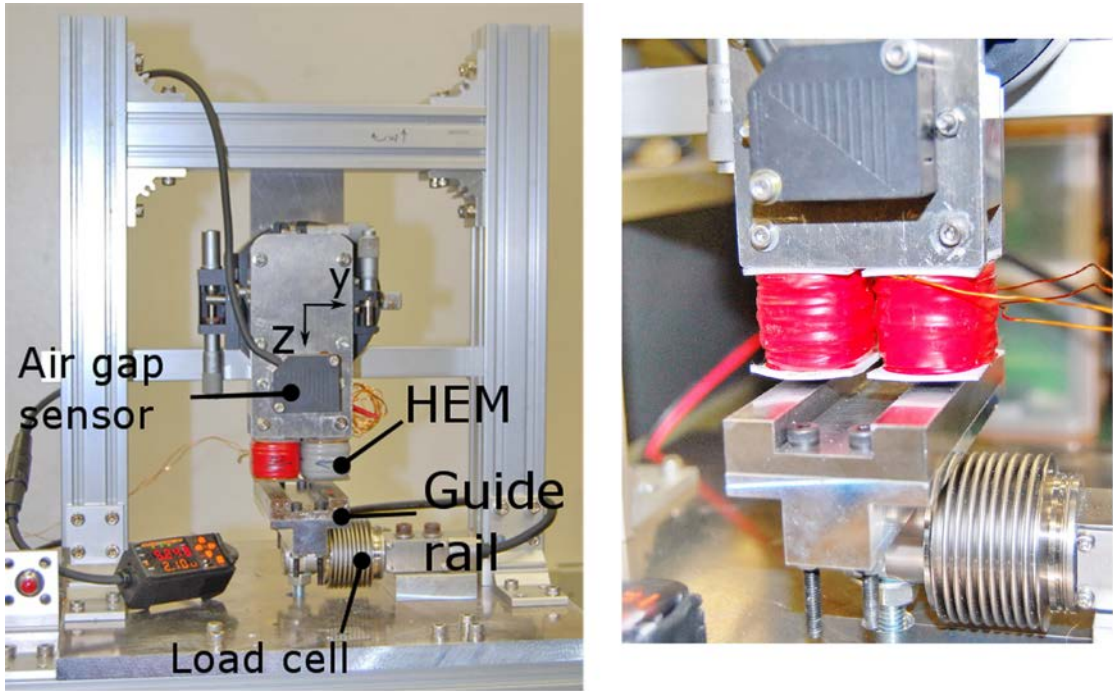
Figure 7.2: Hybrid electromagnet force and air gap measurement system

However, when the air gap becomes small and attractive force increases beyond 150N, the load cell bends upward ($-z$ direction). The bending of the load cell is clearly visible to a necked eye. The micrometer gauge only accounts for the HEM movement and does not measure the deflection of the load cell. Therefore, using a mechanical micrometer gauge to measure the air gap cannot produce accurate measurements.

The air gap measurement was improved by utilizing a laser distance sensor model ZX-LD40 by Omron. The laser sensor has a resolution of 1μm and measurements were averaged using 1024 data samples per each force measurement data point. Since the laser sensor measure distance between the sensor and a target spot, the laser sensor can account for movements of the HEM and the guide rail in the z-direction. Since small misalignments between the HEM and the guide rail can produce large errors in force measurements at small air gaps, achieving good alignment is important before measurements. The alignment was performed using the knowledge obtained from FEM analysis. According to the fig. 3.6, the attractive force becomes maximum at a given air gap when the HEM and the guide rail is properly aligned in y-direction. Furthermore, when the HEM and the guide rail mating surfaces are parallel, the attractive force is maximum at a

77

given air gap. Micrometer gauges was used to adjust the HEM in y-direction and around the x-axis. When the air gap is minimum, the attractive force becomes maximum for a given coil current. Therefore, it is assumed that the air gap is the minimum experimentally achievable value when the force measured is maximum while having zero coil current. When the HEM moved in z-direction starting from a large air gap, the attractive force increases and after the minimum air gap is exceed, the attractive force rapidly reduces.

Figure 7.3 shows the data obtained from the experiment and the fig. 7.4 shows the experimental and FEM analysis data comparison. According to the results, the measured data from the experiment resulted in less force than FEM analysis data. The reasons for the less measured forces include engineering tolerances in HEM manufacturing, non-perfect coil winding, non-homogeneous material properties and measurement errors. However, the resulted surface has the same shape as FEM analysis. The subsequent surface fitting of the experimental data resulted following values for the constants of Eq. 3.2.

$a = 1.915 \times 10^{-5} \text{ Nm}^2\text{A}^{-2}$

$b = 4.242 \text{ A}$

$c = 1.526 \times 10^{-3}\text{m}$

The surface fitting resulted root mean square error (RMSE) 0.52N.

During the experiment, it is observed that the HEM reach an approximate temperature of 90^0C measured at the surface of the permanent magnet for 2A coil current. Since the N50 permanent magnet used is rated up to 115^0C operation, up to 2A continuous current operation is achievable for the manufactured prototype HEM. However, when the zero current operation of the MagLevLS platform is achieved, the steady state current is less than 50mA. The coil currents reach up to 3.6A during the transient states. However, a transient state lasts less than 1s and therefore, the manufactured HEM is well within the operational limits of the MagLevLS system.
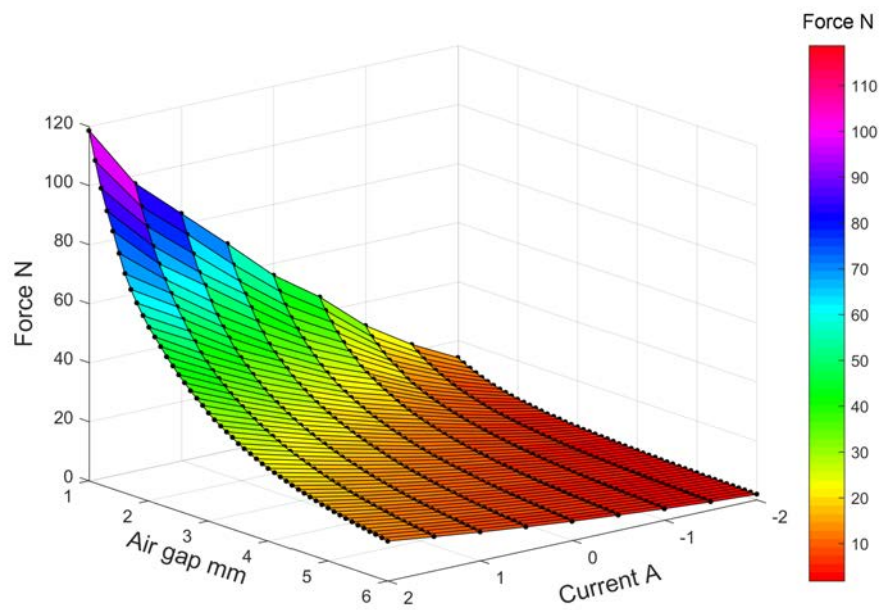
Figure 7.3: Hybrid electromagnet experimental data. The black dots represent measured data points.
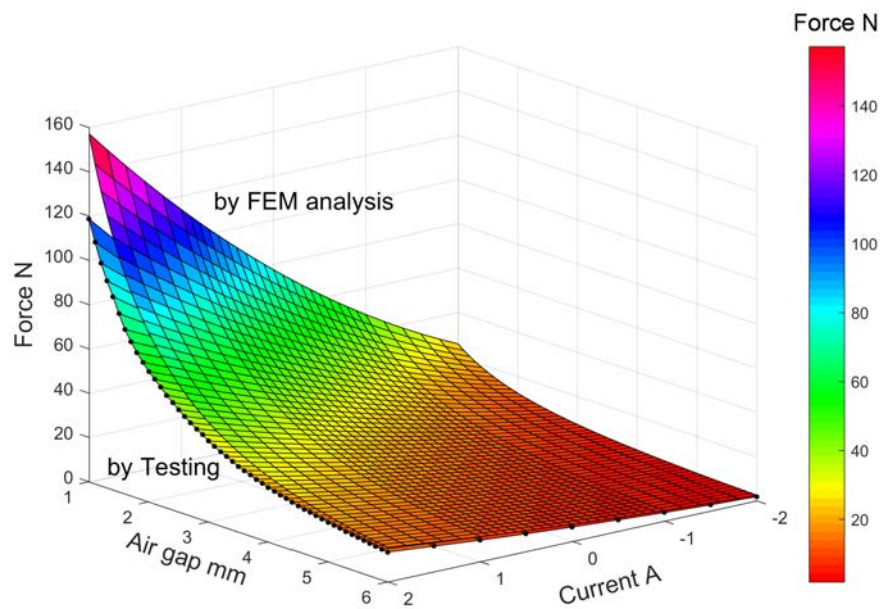
Figure 7.4: Comparison between Hybrid electromagnet experimental data and FEM analysis data.

7.2 Prototype magnetically levitated linear slider system and experiments performed

The experimental MagLevLS system is constructed with the open-end generator and the system performance was observed. The experimental system uses four laser distance sensors of type ZX-LD40 with ZX-LDA11 sensor signal amplifiers manufactured by Omron to measure the air gaps of the HEMs. A DSP board with 1 kHz sampling rate is used for data acquisition from laser distance sensors and to calculate controlled currents for the HEMs to achieve stable levitation. The model of the DSP used is Pass/iBis 7101A manufactured by MTT. The HEMs are driven using four PWM motor controllers with a PWM frequency of 56 kHz. The motor controllers used are ESCON 50/5 manufactured by Maxon motors.

The DSP board has a 1 ms delay between the air-gap measurement using laser sensors to control-current output command to PWM motor controllers. The motor controllers work as current controllers and a voltage signal proportional to the required current was sent to the motor controller from the DSP. The DSP board can measure only up to three variables at a time; therefore, the presented data were obtained from several repeated experiments.

During the experiments, it is observed that the laser sensor output noise has a standard deviation of 6 μm when the open-end generator is not operated. When the open-end generator is started, the standard deviation of the noise increases to 8 μm. Therefore, the 12th order FIR filter was used to filter input air gap signals before they were directed to the PD controllers. Noise measurements are taken when the MagLevLS platform is not levitated. Figure 7.5 shows the measured laser sensor data and the filtered laser sensor data. Data was recorded at 1 kHz sampling rate.

Furthermore, it is observed that the output commands to the PWM motor controllers from DSP fluctuates at 1 kHz frequency within the amplitude range of -0.5 to +0.5 A. This fluctuation leads to vibrations in the MagLevLS platform; therefore, the fifth-order FIR filter is used at output command to reduce the output command fluctuation. The output command noise is due to the large derivative gains required to levitate and stabilize the MagLevLS system. The total weight of the prototype MagLevLS platform including four HEMs, open-end generator, and air gap sensors is approximately 6.4kg.

To measure the response of the MagLevLS system, a 1.1 kg (m_0) steel block
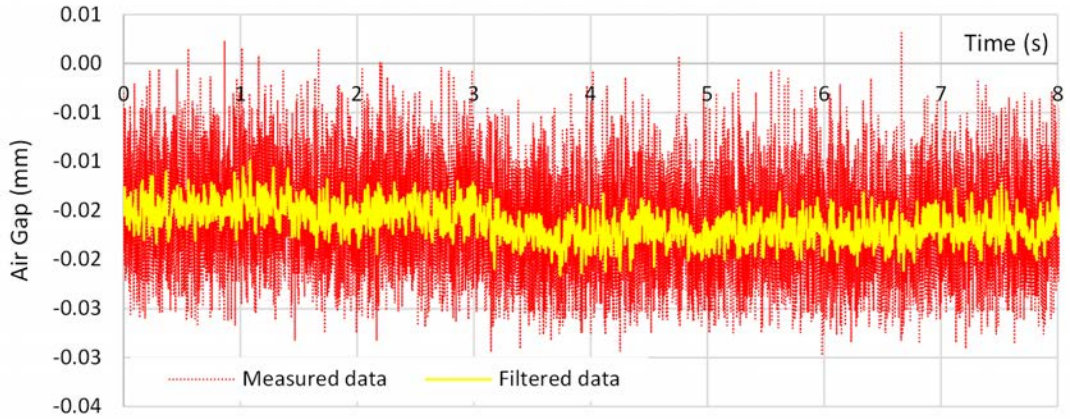
Figure 7.5: Air gap measurement data from laser sensor and filtered data after applying 12th order FIR filter. The data represents measurements while the rotor of the open-end generator is not rotating.

is dropped onto the platform from an approximate height of 10 mm while the MagLevLS platform is levitated. This procedure introduces impact load to the levitated platform and also changes the platform dynamics by introducing additional mass. An electromagnet is used to drop the m_0 mass onto the MagLevLS platform with a minimum disturbance to the system. Each of the results presented is obtained by performing a separate experiment due to the three variable recording limit of the DSP; therefore, the time of applying external input is not same on the time axis of the graphs.

The experiments differ from the simulation because of the application of additional mass to the platform changes platform dynamics. In the simulation, the external input was applied using an external force without changing the platform dynamics. The gains used for the experiment successfully managed to levitate the MagLevLS platform under external load input. The nonlinear system simulations and experiments were performed using identical controller gains.

7.2.1 Response to a load applied at point P1

Figure 7.6 shows the measured state variables z, α, and θ when mass m_0 is dropped onto the MagLevLS platform while the open-end generator is not operated (i.e. rotor rpm is 0). The mass was dropped near point P1 of fig. 6.1. The line of action of the gravitational force acting on the m_0 mass and the line of action of the gravitational force acting on the levitated platform are within 5 mm from each

81

other when the m_0 mass comes to rest on the platform. Figure 7.7 shows the measured state variables z, α, and θ when the same experiment is performed while the open-end generator is producing power. The rotor of the open-end generator is rotating at 1000 rpm. During the experiment, one of the two coils of the open-end generator is connected to a 19 Ω load. The effect of the cogging torque introduced by the open-end generator is clearly visible in state variable α of fig. 7.7 since α is non-zero. The state variable θ was affected at the time of external input according to the results. However, state variable θ returned to a near zero value after about 3s from external input. In nonlinear simulations, the state variable θ was not affected during a similar experiment. This behavior of the state variable θ is expected since it is not possible to place the mass m_0 at exact point P1 and impact forces could introduce forces in y and x directions of the platform.

Figure 7.6: Measured state variables z, α, and θ when 1.1 kg mass is dropped onto the levitated platform. The open-end generator is not operated during experiment.

Figure 7.8 shows the currents measured from three HEMs during a similar experiment while the open-end generator is not operated. Figure 7.9 shows the currents observed while the rotor of the open-end generator is rotating at 1000 rpm and a 19 Ω load is connected to one of the two coils of the open-end generator. The results show that the MagLevLS reaches near zero current operation point within about 1s of external load input. Furthermore, slightly increased vibrations due to the operation of open-end generator can be seen from experimental data. This is clearly visible before the external input. The vibrations occurred due to the external input takes about 60s to disappear completely. The vibrations last for a long time because y-direction motion is not controlled, and the motion is damped only by some wires connecting levitated platform and stationary structure.

Figure 7.7: Measured state variables z, α, and θ when 1.1 kg mass is dropped onto the levitated platform. The rotor of the open-end generator is rotating at 1000 rpm and one coil of the open-end generator is connected to a 19 Ω load.

Figure 7.8: Measured currents of HEMs when 1.1 kg mass is dropped onto the levitated platform. The open-end generator is not operated during the experiment.

Figure 7.9: Measured currents of HEMs when 1.1 kg mass is dropped onto the levitated platform. The rotor of the open-end generator is rotating at 1000 rpm and one coil of the open-end generator is connected to a 19 Ω load.

Figure 7.10 shows the power consumption measured during a similar experiment from HEMs while the rotor of the open-end generator is rotating at 1000 rpm and a 19 Ω load is connected to one of the two coils of the open-end generator. According to the results, the power consumed by each HEM surges up to 35 W when external load applied. However, the power consumption reduces to less than 1 W per HEM within 0.5 s. After about 5 s from the external input, the power consumption reduces to less than 0.25 W per HEM.

Figure 7.10: Measured power from the HEMs when 1.1 kg mass is dropped onto the levitated platform. The rotor of the open-end generator is rotating at 1000 rpm and one coil of the open-end generator is connected to a 19 Ω load.

84

7.2.2 Response to a load applied at point P2

When the MagLevLS is used for material transport, it is not possible to guarantee that the goods placed on the platform will always have their center of gravity near the center of gravity of the MagLevLS platform. To simulate this situation, mass m_0 is dropped onto the platform close to point P2. The placement accuracy of the center of gravity of mass m_0 is within 10 mm from point P2 in x and y-directions.

Figure 7.11 shows the measured state variables z, α, and θ when the open-end generator is not operated. Figure 7.12 shows the same state variables when the rotor of the open-end generator is rotated at a speed of 1000 rpm while one coil of the open-end generator is connected to a 19 Ω load. The increase in vibrations due to the operation of open-end generator can be clearly seen before the external input. Furthermore, the state variable α has non zero value when the open-end generator is producing power. Since the external mass was added to a non-centered location, the state variable θ reaches a non-zero value after the external input as shown in fig. 7.11 and 7.12, regardless of the state of the open-end generator.
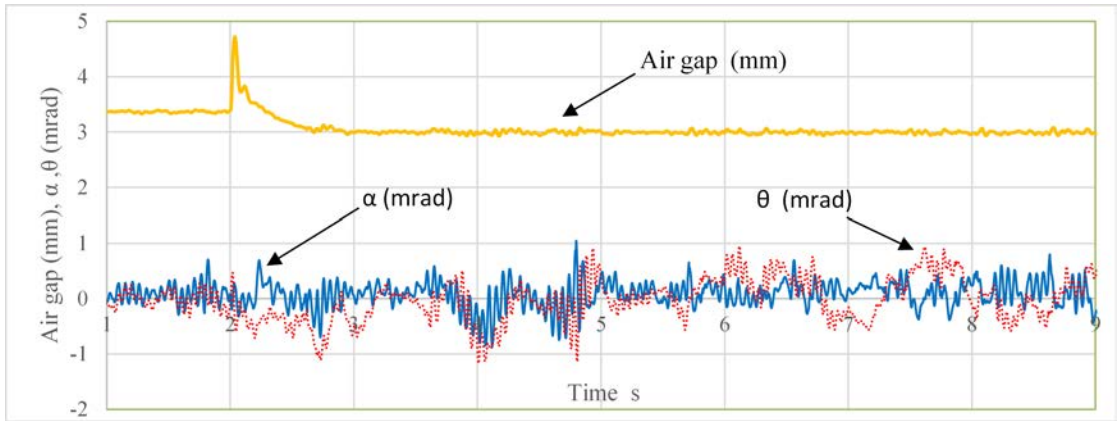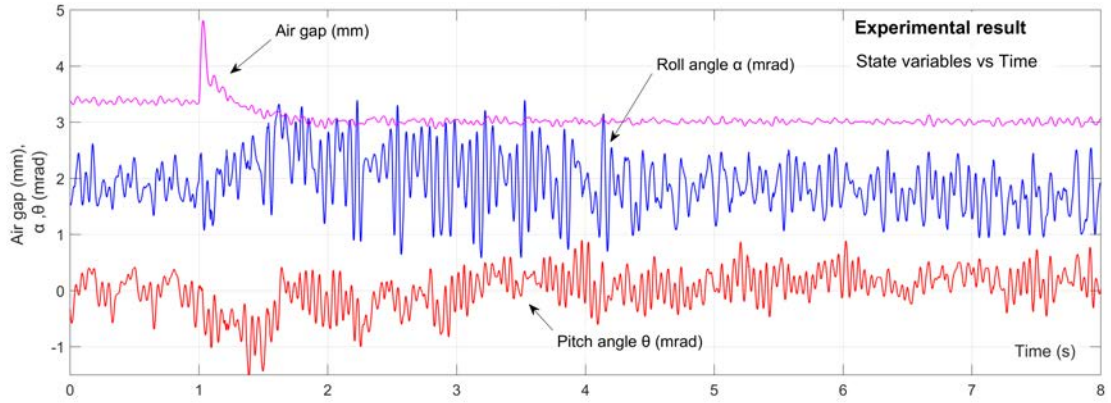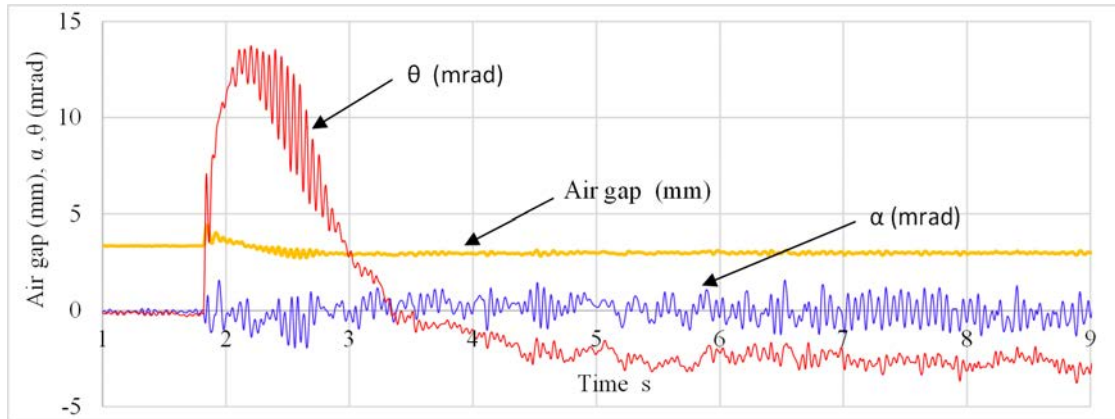

Figure 7.11: Measured state variables z, α, and θ when 1.1 kg mass is dropped onto the levitated platform at point p2. The open-end generator is not operated during the experiment.

Figure 7.13 shows the currents measured from HEMs during a similar experiment while the open-end generator is not operated. Figure 7.14 shows the currents when the experiment is performed while the rotor of the open-end generator is rotating at 1000 rpm and a 19 Ω load connected to one of the two coils of the open-end generator. The results show that the MagLevLS takes about 2.5s to reach near zero current operation point under the experimental conditions.

Once the rotor of the open-end generator is turned on, the driving motor takes
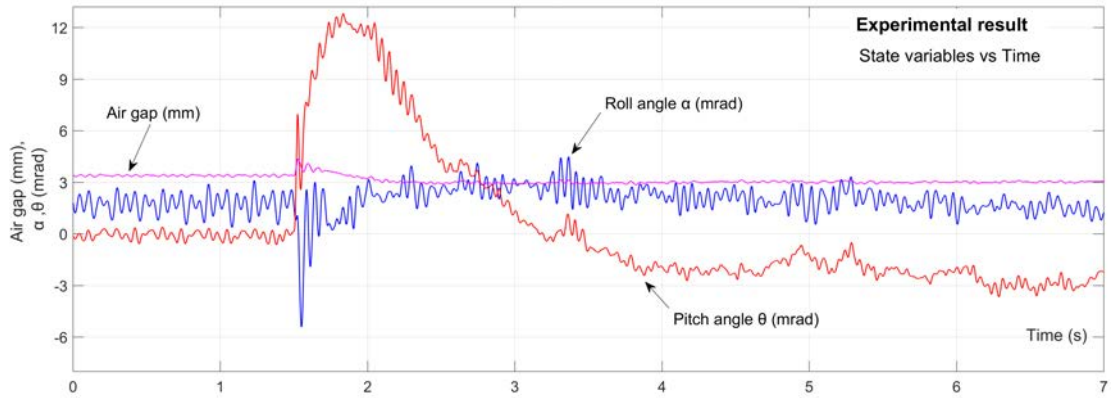
Figure 7.12: Measured state variables z, α, and θ when 1.1 kg mass is dropped onto the levitated platform at point p2. The rotor of the open-end generator is rotating at 1000 rpm and one coil of the open-end generator is connected to a 19 Ω load.
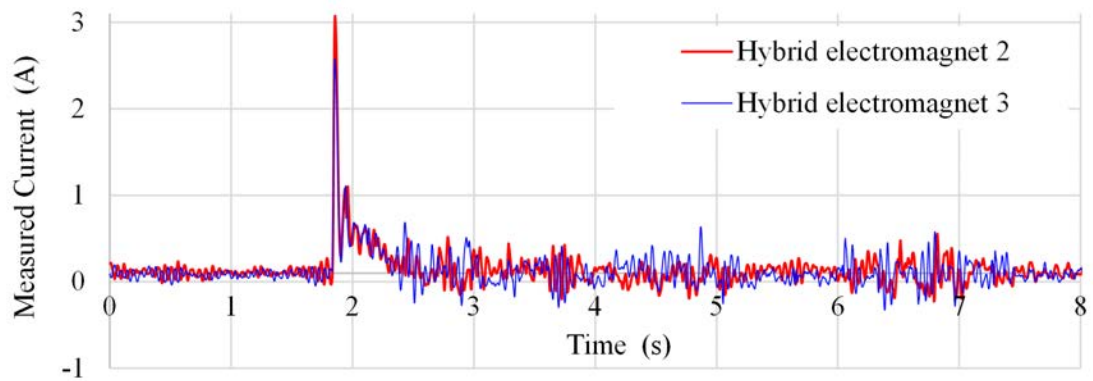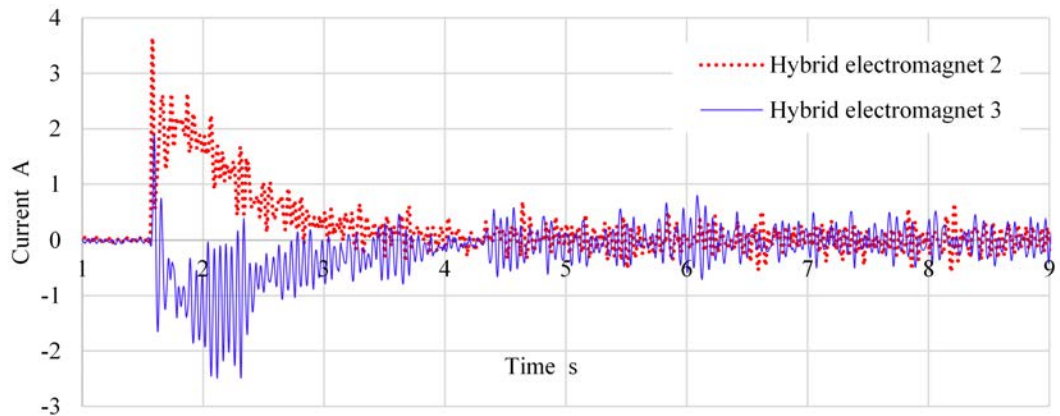

Figure 7.13: Measured currents of HEMs when 1.1 kg mass is dropped onto the levitated platform. The open-end generator is not operated during the experiment
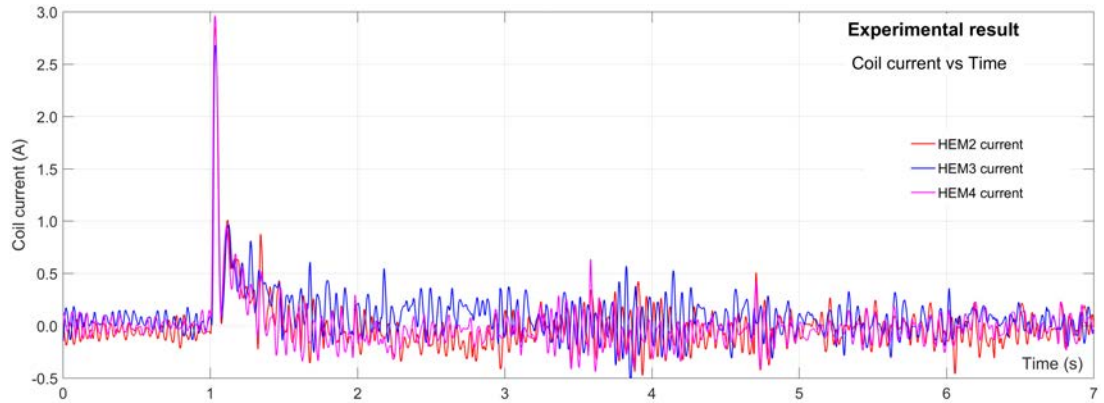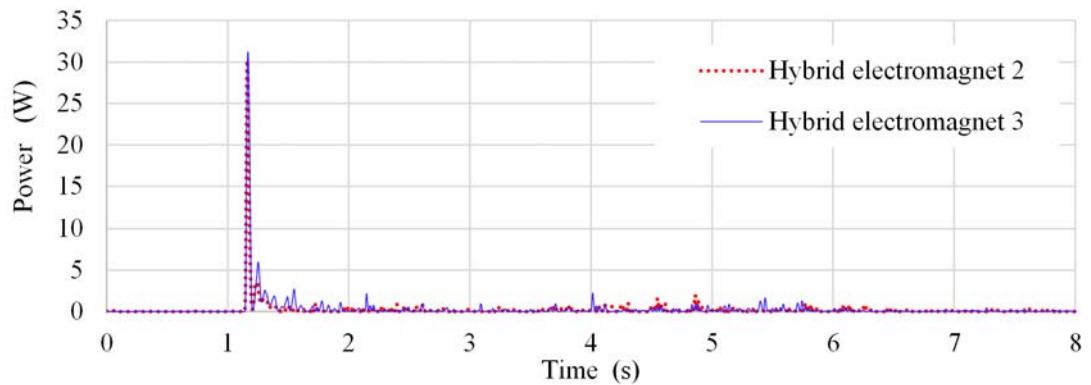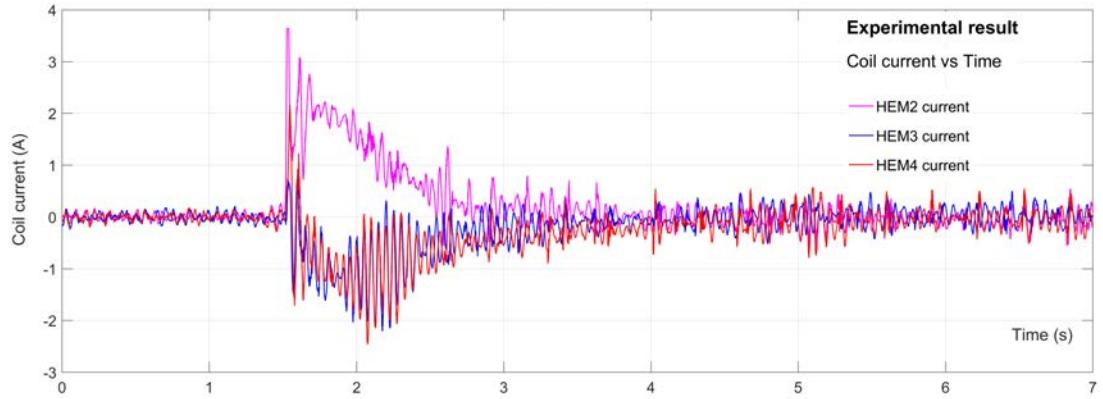
Figure 7.14: Measured currents of HEMs when 1.1 kg mass is dropped onto the levitated platform. The rotor of the open-end generator is rotating at 1000 rpm and one coil of the open-end generator is connected to a 19 Ω load
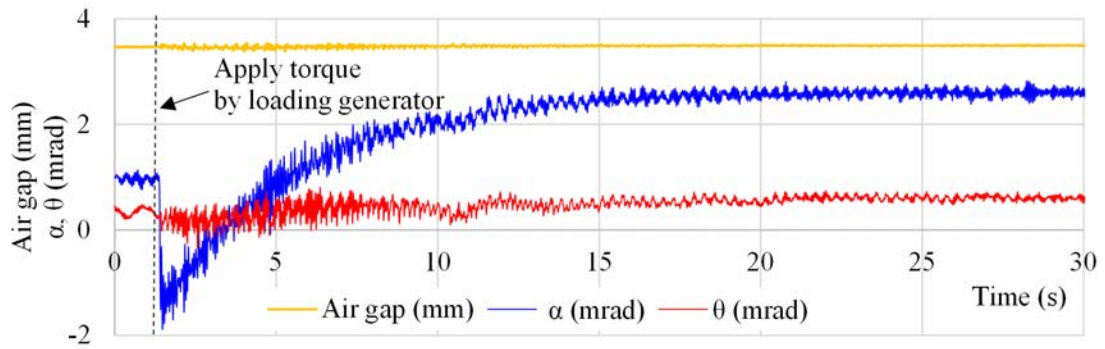
Figure 7.15: System response when the open-end generator is connected to a resistive load using a switch

about 10 seconds to reach final steady rotor speed, when the open-end generator is connected to an electrical load. Therefore application of load is not sudden. However, if the generator is not connected to an electrical load the torque produced by the generator is zero. If an electrical load is connected suddenly, the generator will produce immediate torque. However, the immediate torque will cause the rotor motor to slow down and gain 1000rpm speed again. Figure 7.15 shows the response of the system when the one phase of open-end generator is connected to an external resistive load of 19Ω using a switch. When the switch is off, the resistive load is disconnected and the generator is at open circuit condition. When the switch is turned on, generator immediately applies torque on levitated platform around x-axis. According to the results shown in fig. 7.15, the platform takes about 15s to reach steady state zero power levitation position.

7.3 Experimental results of the open-end generator

The prototype open-end generator was constructed using ABS for the stator core. Figure 7.16 shows the manufactured open-end generator stator core with generator mounts and the fig. 7.17 shows the open-end generator installed on the levitated platform. The manufactured open-end generator has two coil windings at approximately 180-degree phase angle. Each coil has 120 turns wound using $\phi 0.5$mm copper wire.
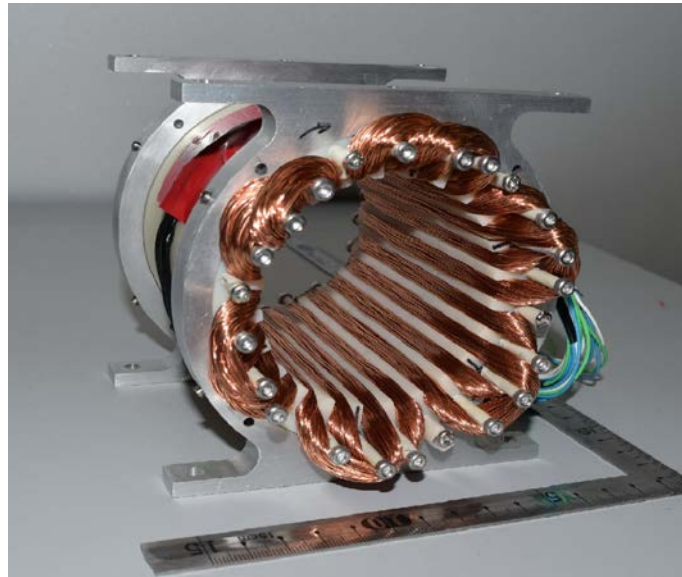
Figure 7.16: Stator core of the open-end generator

The open-end generator is operated at several rotational speeds, rotor eccentricity values, and external loads. Figure 7.18 shows the RMS electric power dissipated through 19Ω, 9.5Ω, and 1Ω load resistors at 800 rpm rotor speed through a single coil of the open-end generator. According to the results, the open-end generator can generate 11.4 W electric power per coil. This result is a close match to the FEM analysis result of 12.2 W RMS electric power per coil. Furthermore, a significant change of power dissipation due to RE is not observed during the experiment as shown in fig. 7.18. The internal resistance of a winding of open end generator was approximately 19Ω. Therefore an external electrical load of 19Ω was selected to obtain maximum power from open end generator.

Figure 7.19 shows the RMS electric power dissipated through 19Ω, 9.5Ω, and
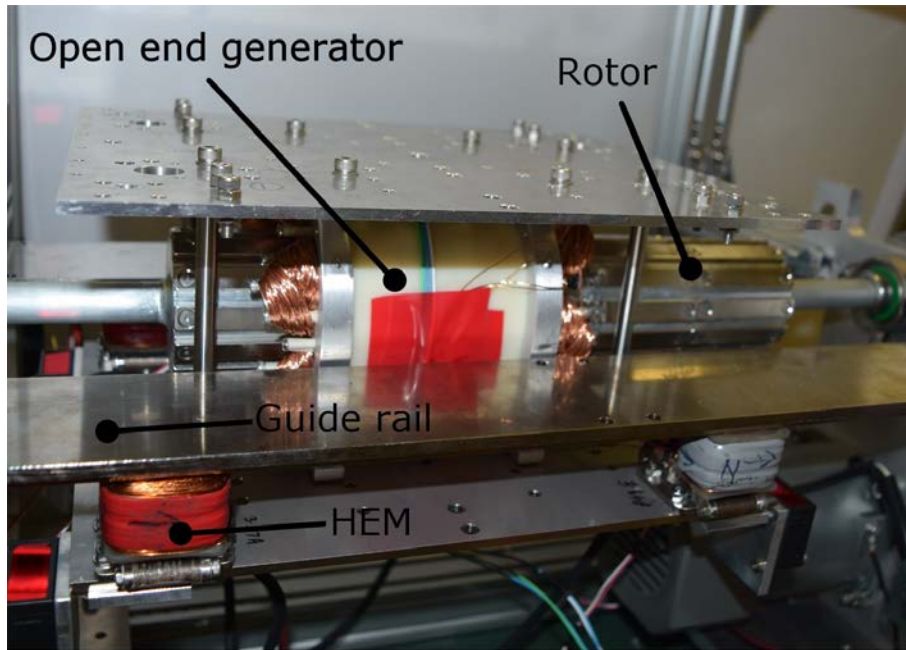
Figure 7.17: open-end generator placement in MagLevLS system

1Ω load resistors at 100 to 1100 rpm rotor speeds through a single coil of the open-end generator. According to the results, the open-end generator can generate 17.7 W electric power per coil at 1000 rpm rotor speed. Therefore, the open-end generator can generate approximately 35 W power using both coils at 1000 rpm rotor speed. The measured steady-state power consumption of the MagLevLS system is approximately 15 W for the electronic components, four HEMs, and air gap sensors. Therefore, it is possible to supply power continuously to the MagLevLS using a battery and the open-end generator. During loading and unloading, a battery can support to supply peak power demand, and during the steady-state operation, the open-end generator can recharge the battery while supplying power for steady state operation.
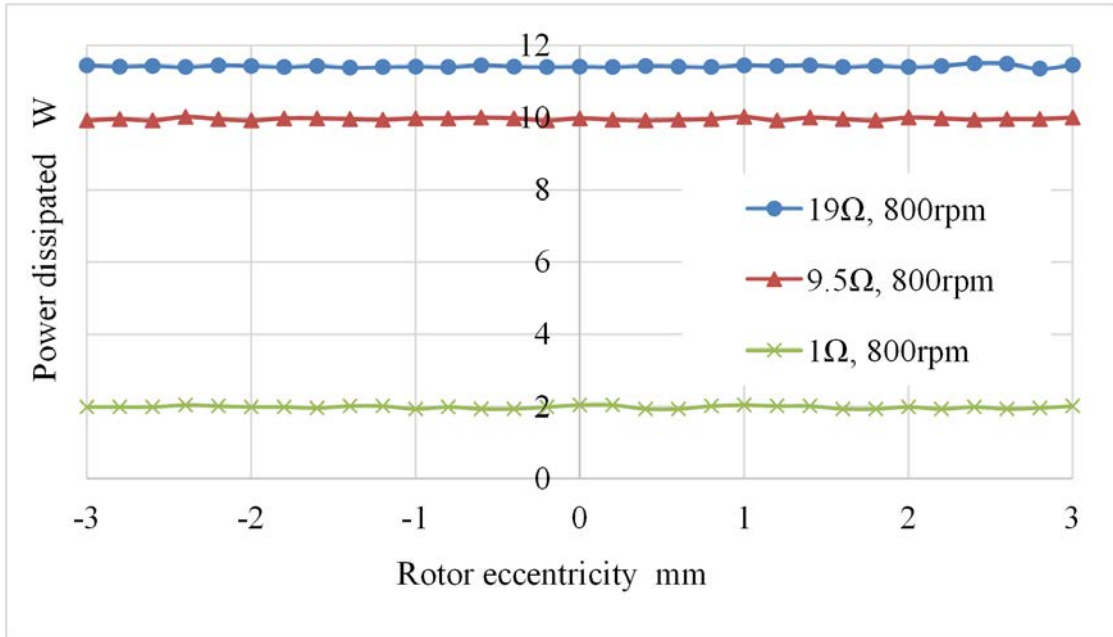
Figure 7.18: RMS electric power dissipated through 19Ω, 9.5Ω, and 1Ω load resistors at 800 rpm rotor speed through a single coil of the open-end generator at -3mm to 3 mm REs.
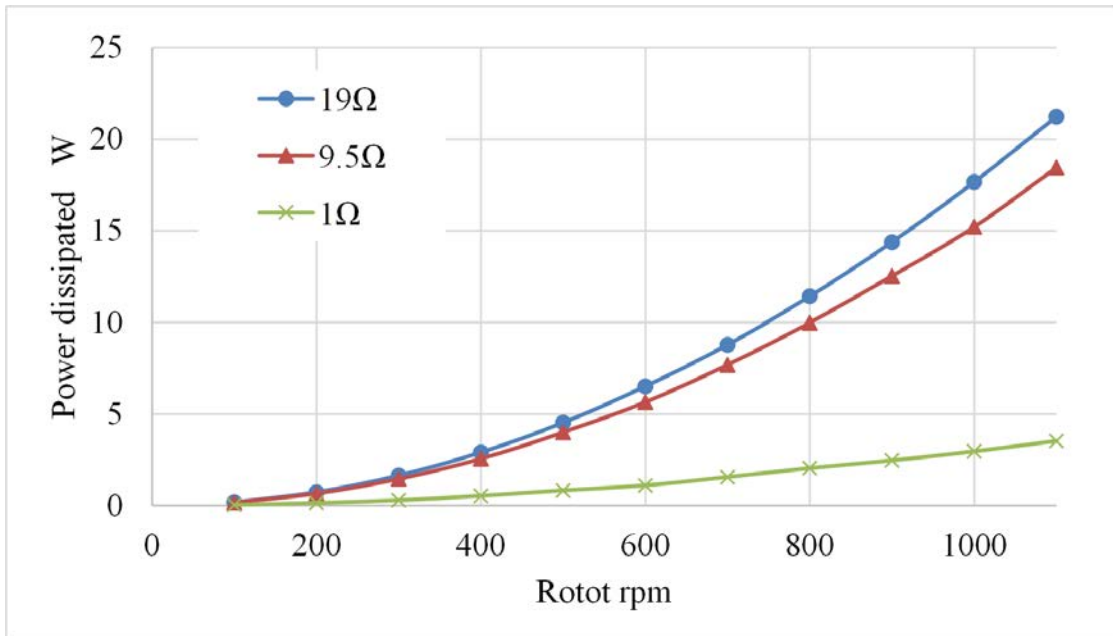
Figure 7.19: RMS electric power dissipated through 19 Ω, 9.5 Ω, and 1 Ω load resistors at 100 to 1100 rpm rotor speeds through a single coil of the open-end generator.

Chapter 8

Conclusions

A magnetically levitated linear slider (MagLevLS) platform was designed, fabricated and experimental data was obtained. A novel non-contact power transfer system using an open-end generator was purposed and custom designed to meet the requirements of the levitated platform. The proposed system is suitable to transport materials between short distances in a clean room environment. The main components of the system were designed separately and integrated into a single system. Main components of the system are the hybrid electromagnets (HEMs) used as levitation actuator and the open-end generator used for non-contact power transfer.

8.1 Summary and conclusions

A hybrid electromagnet was designed to use with a magnetically levitated linear slider platform and capable of generating approximately 65N force using 0A current. The existing designs of a hybrid electromagnet were improved to achieve better lateral aliment. The design of the HEM was analyzed using finite element method (FEM). The improvements made to the HEM was analyzed using FEM data and presented. The FEM analysis data was used to find the relationship between the attractive force, coil current and air gap using surface fitting techniques. A prototype electromagnet was fabricated and experimental data obtained by measuring attractive force, coil current and air gap. The analysis of experimental data and FEM data revealed that the experimental data has lower values than FEM analysis data. However, the experimental data showed a close match to FEM analysis data. The obtained data was used to derive a mathematical model

describing the attractive force in terms of coil current and air gap. The linearized mathematical model was used in designing levitation controller.

A novel method of using an open-end generator was suggested to transfer power to the levitated platform without using contacts. The open-end generator was designed to meet three specific goals so that the open-end generator can be used with the magnetically levitated platform. The first goal was to reduce the cogging forces generated by the open-end generator to a limit that can be handled by the HEMs. The second goal was to transfer sufficient amount electrical power to the levitated platform. It is calculated that 35W of root mean square (RMS) electrical power is sufficient to achieve continuous operation of the system. The third goal was to achieve sufficient air gap between the stator and the rotor of the open-end generator to achieve different zero power levitation air gaps under different load conditions. The design goal of air gap was to achieve air gap of at least 3.5mm when the rotor of the open-end generator is at the center of the stator core of the generator. All three design goals are interconnected in such a way that changing one parameter affects all other parameters. Even though a fairly large cogging force can be compensated using HEMs in the z-direction, it is not possible to compensate large forces in y-direction because HEMs are not designed to generate large forces in the y-direction. A several generator designs were analyzed using FEM to calculate cogging forces. The analysis revealed that the cogging forces generated by an open-end generator with a soft magnetic steel core cannot be compensated by y-direction forces of HEMs. The FEM analysis of open-end generators with soft magnetic steel cores resulted in RMS electrical power larger than 100W while achieving 3.5mm air gap goal. Furthermore, analysis reviled that the cogging forces are generated regardless of the amount of power generated by the open-end generator.

Due to the large cogging forces generated by soft magnetic steel stator cored generators, an open-end generator was designed using ABS as the stator core material. After several refinements, the open-end generator with ABS stator core resulted approximately 35W of RMS electrical power while having 4.25mm air gap. The cogging forces generated by the open-end generator with ABS stator core depends on the current generated in the coils of the generator according to the FEM analysis results. When the current in coils of the open-end generator is zero, the cogging force becomes zero. Since the cogging force is generated due to the induction of current in coils, the cogging force is a Lorentz force. The maxi-

mum amount of cogging force of the final design was approximately 1.1N at 3mm rotor eccentricity while having 19Ω external load per winding. Furthermore, FEM analysis revealed that the cogging force is a restitutive force supporting alignment of levitated platform in the y-direction. The FEM analysis showed that the cogging torque generated by the open-end generator was approximately 0.5Nm and fluctuations due to the rotor angular position are negligible. The change of electrical power generated due to the rotor eccentricity is negligible according to the FEM analysis results. Therefore, the open-end generator can supply the same amount of power to the levitated platform regardless of the rotor eccentricity. This is an advantage for the levitated platform. Based on FEM analysis and experimental results, it is concluded that the open-end generator with an ABS stator core can meet all design goals and suitable to supply power to the levitated platform. Since the open-end generator was designed to use readily available cuboid shaped permanent magnets and due to the physical size constraints, a slight overlap between electrical coil windings was observed in the final open-end generator design.

A mathematical model for the MagLevLS platform describing three degrees of freedom motion was developed. The forces of the HEMs was described using the model obtained by FEM analysis and experimental testing. The linearized mathematical model was used to develop three PD controllers to control vertical levitation position, roll, and pitch. The gains of three PD controllers was obtained to meet selected system performance. The experiments revealed that the initial gains of the PD controllers were not accurate enough to maintain stable levitation of the experimental system. Subsequently, a nonlinear system was modeled, and the initial controller was tuned. The nonlinear system was modeled to closely match components of the experimental system. The controller was improved to achieve zero power operation by adding three integral controllers to the initial levitation controller. The levitation system was simulated to observe different real world operation scenarios and results were presented. The simulations revealed that the levitation controller with zero power control loop can achieve and maintain stable levitation under step inputs while the cogging torque of the open-end generator is active. Furthermore, the effect of cogging torque on levitated platform was clearly visible in the simulation results.

A prototype platform with an open-end generator was fabricated to experimentally validate simulation results. The levitated system was constructed as a four-point suspended single rigid rectangular platform. Therefore achieving zero

power operation of all four HEMs was not possible in the experimental system. The controller was designed to achieve near zero power operation of the experimental platform. The experimental system has a DSP board with 1 kHz sampling rate, four laser air gap sensors, and four hybrid electromagnets. The con-contact power transfer was achieved by operating the open-end generator. Experiments were performed to evaluate the levitation system under a step load input applied at the center of the levitated platform and applied at one side of the platform. Experiments revealed that the MagLevLS system can achieve and maintain stable levitation under cogging forces and torque introduced by the open-end generator. Furthermore, slightly increased vibrations were observed due to the operation of the open-end generator. The experiments revealed that the prototype open-end generator can generate approximately 35W RMS electrical power at 1000rpm rotor speed. Furthermore, experiments confirmed that the change of generated electrical power due to the rotor eccentricity was negligible. The experimental observations of the open-end generator was a close match to the FEM analysis results. The effect of the cogging torque was clearly visible in the experimental results. However, the zero power levitation controller managed to reach near zero power operation point under step input within approximately 2.5s time. The power consumption per HEM was increased to 35W during the transient state of step input. However, the power consumption reduced to less than 1W per HEM within 0.5s of step input and reduced to 0.25W per HEM within 5s of step input. The power measurements were recorded under the influence of cogging forces and torque of the open-end generator. Therefore, it is concluded that the MagLevLS can be powered through open-end generator and stable near zero power operation can be achieved while disturbances introduced by the cogging forces are acting on the levitated platform.

During the experiments, lateral vibrations were observed due to the application of step load. The major reason for the lateral vibrations is because of application of step load, which is not perfectly vertical at the time of application. Furthermore, if the platform is not perfectly orthogonal to the direction of gravity at the time of application of the step load, the application of vertical step load leads to force components in vertical, lateral and horizontal directions. Lateral vibrations are not controlled and not actively damped. Therefore, it is observed that the lateral vibrations due to the application of step load take about 60s to disappear. However, MagLevLS platform managed to return to lateral position due to the improvements made to HEM and guide rail design.

During the manufacturing of prototype, it is observed that the manufacturing process of the rotor is complicated and fairly expensive compared to other mechanical elements of the system. Furthermore, all major components manufactured using SS400 was galvanized to avoid corrosion. The HEMs were made using laminated soft magnetic steel to reduce eddy currents.

As a result of the research work carried out, a magnetically levitated linear slider system was designed, analyzed and stable near zero power levitation was achieved. The suggested novel non-contact power transfer system was designed, analyzed and a prototype was fabricated. The complete system was controlled using a DSP controller and observed experimental results were a close match to the simulation and FEM analysis results.

8.2   Possible improvements and future work

The completion of prototype and subsequent experiments on the magnetically levitated linear slider platform revealed several problems of the constructed prototype and control system.

One of the major problems observed during the levitation was the lateral vibrations. The current system does not control or actively damp lateral vibrations. The lateral alignment of the current system was achieved by lateral restitutive forces generated by the HEMs and open-end generator. Since the lateral force generated by the open-end generator can be controlled by the current in the coils of the open-end generator, it is suggested to design a controller to reduce lateral vibrations by controlling current in generator coils. If the platform was rotated around the x-axis, the attractive forces of the HEMs could generate a lateral force component. Therefore, by controlling the roll of the platform, the lateral vibration could be controlled. However, this approach needs further study to evaluate the applicability to the levitated system.

The HEMs were manufactured by manually wound coils. Therefore, four HEMs are not a close match. By using machine winding to fabricate coils of the HEMs, the HEMs could be improved to be a close match to each other. This could reduce the amount of steady state power consumption of the HEMs.

The laser air gap sensors were observed to be noisy. Therefore, better sensors could be utilized to improve levitation performance. It is suggested to use inductive sensors to measure air gap to achieve better performance. The experiments

were performed on the first prototype fabricated. Since the prototype design was made to accommodate design changes at later stages, the tolerances of mechanical components are high. All adjustments were made manually, and aluminum extrusions were used to fabricate the stationary structure. It is suggested to improve the stationary structure of the system to accommodate tighter tolerances and to a better rigidity to reduce vibration due to the operation of the open-end generator.

The non-contact power transfer system needs a battery to supply peak power demand. Therefore, a battery charging and power supply system must be designed to use the power of the open-end generator for the control of the levitated system.

The linear motor of the system should be integrated to the levitation control system to achieve position and thrust control.

Other non-contact power transfer methods should be investigated and experimented with the levitated platform to evaluate best non-contact power transfer method the levitated platform.

The designed nonlinear system simulator gains were directly compatible with the experimental system. Therefore, initial system testing was fast and convenient. It is suggested to improve nonlinear system simulator to accommodate lateral motion of the system. This could be advantages to rapidly evaluate different lateral alignment and vibration damping controllers.

Bibliography

[1] M. Morishita and T. Azukizawa, "Zero power control of electromagnetic levitation system," *Electrical Engineering in Japan*, vol. 108, no. 3, pp. 111–120, 1988. [Online]. Available: http://dx.doi.org/10.1002/eej.4391080313

[2] M. Morishita, T. Azukizawa, S. Kanda, N. Tamura, and T. Yokoyama, "A new maglev system for magnetically levitated carrier system," *IEEE Transactions on Vehicular Technology*, vol. 38, no. 4, pp. 230–236, Nov 1989.

[3] C. H. Kim, J. M. Lee, H. S. Han, and B. S. Kim, "Levitation and thrust control of a maglev lcd glass conveyor," in *IECON 2011 - 37th Annual Conference on IEEE Industrial Electronics Society*, Nov 2011, pp. 610–615.

[4] K. Kim, J. Han, C. Kim, J. Lee, and H. Han, "Dynamic analysis of maglev conveyor using an em-pm hybrid suspension," in *2011 IEEE International Conference on Mechatronics and Automation*, Aug 2011, pp. 2027–2032.

[5] C. H. Kim, K. J. Kim, J. S. Yu, and H. W. Cho, "Dynamic performance evaluation of 5-dof magnetic levitation and guidance device by using equivalent magnetic circuit model," *IEEE Transactions on Magnetics*, vol. 49, no. 7, pp. 4156–4159, July 2013.

[6] Y. ISHINO, M. TAKASAKI, and T. MIZUNO, "Fabrication of non-contact carrier system using solar magnetic suspension," *Mechanical Engineering Journal Japan society of Mechanical Engineers*, vol. 2, no. 4, 2015.

[7] X. Wei, Z. Wang, and H. Dai, "A critical review of wireless power transfer via strongly coupled magnetic resonances," *Energies*, vol. 7, no. 7, p. 4316, 2014. [Online]. Available: http://www.mdpi.com/1996-1073/7/7/4316

[8] J. Dai and D. C. Ludois, "A survey of wireless power transfer and a critical comparison of inductive and capacitive coupling for small gap applications,"

IEEE Transactions on Power Electronics, vol. 30, no. 11, pp. 6017–6029, Nov 2015.

[9] R. J. Mukti, N. P. Begum, and A. Islam, "Analysis of medium range wireless power transfer system using magnetic resonant coupling," in *Informatics, Electronics Vision (ICIEV), 2014 International Conference on*, May 2014, pp. 1–6.

[10] Z. N. Low, R. A. Chinga, R. Tseng, and J. Lin, "Design and test of a high-power high-efficiency loosely coupled planar wireless power transfer system," *IEEE Transactions on Industrial Electronics*, vol. 56, no. 5, pp. 1801–1812, May 2009.

[11] Y. D. Chung, C. Y. Lee, H. Kang, and Y. G. Park, "Design considerations of superconducting wireless power transfer for electric vehicle at different inserted resonators," *IEEE Transactions on Applied Superconductivity*, vol. 26, no. 4, pp. 1–5, June 2016.

[12] A. Kurs, A. Karalis, R. Moffatt, J. D. Joannopoulos, P. Fisher, and M. Soljačić, "Wireless power transfer via strongly coupled magnetic resonances," *Science*, vol. 317, no. 5834, pp. 83–86, 2007. [Online]. Available: http://science.sciencemag.org/content/317/5834/83

[13] J. Wang, Z. P. Xia, and D. Howe, "Three-phase modular permanent magnet brushless machine for torque boosting on a downsized ice vehicle," *IEEE Transactions on Vehicular Technology*, vol. 54, no. 3, pp. 809–816, May 2005.

[14] T. Azukizawa, M. Morishita, S. Kanda, N. Tamura, and T. Yokoyama, "A linear induction motor control system for magnetically levitated carrier system," *IEEE Transactions on Vehicular Technology*, vol. 38, no. 2, pp. 102–108, May 1989.

[15] M. Morishita, "Robust controller design for maglev transport vehicles with a guide-effective electromagnetic suspension system," in *Decision and Control, 1996., Proceedings of the 35th IEEE Conference on*, vol. 2, Dec 1996, pp. 1242–1244 vol.2.

[16] M. Morishita and H. Itoh, "The self-gap-detecting electromagnetic suspension system with robust stability against variation of levitation mass," in *Interna-*

tional Symposium on Power Electronics, Electrical Drives, Automation and Motion, 2006. SPEEDAM 2006., May 2006, pp. 1178–1183.

[17] C. H. Kim, H. W. Cho, J. M. Lee, H. S. Han, B. S. Kim, and D. S. Kim, "Levitation control of a hybrid-excited magnetic levitation vehicle," in *Control, Automation and Systems (ICCAS), 2011 11th International Conference on*, Oct 2011, pp. 1020–1024.

[18] F. J. Lin, L. T. Teng, and P. H. Shieh, "Intelligent adaptive backstepping control system for magnetic levitation apparatus," *IEEE Transactions on Magnetics*, vol. 43, no. 5, pp. 2009–2018, May 2007.

[19] Y.-K. Tzeng and T. C. Wang, "Dynamic analysis of the maglev system using controlled-pm electromagnets and robust zero-power-control strategy," *IEEE Transactions on Magnetics*, vol. 31, no. 6, pp. 4211–4213, Nov 1995.

[20] F. SUN and K. OKA, "Zero power non-contact suspension system with permanent magnet motion feedback," *Journal of System Design and Dynamics*, vol. 3, no. 4, pp. 627–638, 2009.

[21] Z. Sun, N. C. Cheung, J. Pan, S. Zhao, and W.-C. Gan, "Design and simulation of a magnetic levitated switched reluctance linear actuator system for high precision application," in *2008 IEEE International Symposium on Industrial Electronics*, June 2008, pp. 624–629.

[22] U. Hasirci, A. Balikci, Z. Zabar, and L. Birenbaum, "3-d fem analysis of a novel magnetic levitation system," *IEEE Transactions on Plasma Science*, vol. 43, no. 5, pp. 1261–1265, May 2015.

[23] U. Hasirci, A. Balikci, Z. Zabar, and L. Birenbaum, "A novel magnetic-levitation system: Design, implementation, and nonlinear control," *IEEE Transactions on Plasma Science*, vol. 39, no. 1, pp. 492–497, Jan 2011.

[24] J.-H. Yang, T.-S. Kim, S.-Y. Shim, Y.-S. Lee, and O.-K. Kwon, "Actuator and sensor modeling for magnetic levitation system," in *Control, Automation and Systems, 2007. ICCAS '07. International Conference on*, Oct 2007, pp. 917–922.

[25] A. A. Kuijpers, C. Nemlioglu, F. Sahin, A. Verdel, J. C. Compter, and E. A. Lomonova, "Force analysis of linear induction motor for magnetic levitation

system," in *Power Electronics and Motion Control Conference (EPE/PEMC), 2010 14th International*, Sept 2010, pp. S3–17–S3–20.

[26] A. E. Hajjaji and M. Ouladsine, "Modeling and nonlinear control of magnetic levitation systems," *IEEE Transactions on Industrial Electronics*, vol. 48, no. 4, pp. 831–838, Aug 2001.

[27] S. Verma, W. jong Kim, and J. Gu, "Six-axis nanopositioning device with precision magnetic levitation technology," *IEEE/ASME Transactions on Mechatronics*, vol. 9, no. 2, pp. 384–391, June 2004.

[28] Y. H. Kim, K. M. Kim, and J. Lee, "Zero power control with load observer in controlled-pm levitation," *IEEE Transactions on Magnetics*, vol. 37, no. 4, pp. 2851–2854, Jul 2001.

[29] L. Dosiek and P. Pillay, "Cogging torque reduction in permanent magnet machines," *IEEE Transactions on Industry Applications*, vol. 43, no. 6, pp. 1565–1571, Nov 2007.

[30] F. R. Ismagilov, I. K. Khairullin, V. E. Vavilov, and V. S. Durakova, "Influence of the rotor eccentricity on the magnetic field of high-speed magnetoelectrical generators," *Russian Engineering Research*, vol. 34, no. 10, pp. 617–619, 2014. [Online]. Available: http://dx.doi.org/10.3103/S1068798X14100074

[31] F. Marignetti, A. Vahedi, and S. M. Mirimani, "An analytical approach to eccentricity in axial flux permanent magnet synchronous generators for wind turbines," *Electric Power Components and Systems*, vol. 43, no. 8-10, pp. 1039–1050, 2015. [Online]. Available: http://dx.doi.org/10.1080/15325008.2015.1024356

[32] L. Wang, G. H. Chen, Z. X. Liao, Z. Jun, and J. S. Lian, "A research of suspension system with hybrid electromagnets made of hts coils and normal conductor coils," in *Industrial Electronics and Applications, 2006 1ST IEEE Conference on*, May 2006, pp. 1–4.

[33] G. C. Lee and T. U. Jung, "Cogging torque reduction design of dual stator radial flux permanent magnet generator for small wind turbine," in *TENCON Spring Conference, 2013 IEEE*, April 2013, pp. 85–89.

[34] B. I. Annasiwaththa and K. Oka, "Design concept and analysis of a magnetically levitated linear slider with non-contact power transfer," *International Journal of Applied Electromagnetics and Mechanics*, vol. Preprint, 2016.

[35] B. I. Annasiwaththa, K. Oka, and A. Harada, "Magnetically levitated linear slider with a non-contact power transfer method," *International Journal of Applied Electromagnetics and Mechanics*, vol. Under review, -.